Post-landing major element quantification using SuperCam laser induced breakdown spectroscopy

Ryan B. Anderson, Olivier Forni, Agnes Cousin, Roger C. Wiens, Samuel M. Clegg, Jens Frydenvang, Travis S. J. Gabriel, Ann Ollila, Susanne Schröder, Olivier Beyssac, et al.

Post-Landing Major Element Quantification Using SuperCam Laser Induced Breakdown Spectroscopy

Ryan B. Anderson[1], Olivier Forni[2], Agnes Cousin[2], Roger C. Wiens[3], Samuel M. Clegg[3], Jens Frydenvang[4], Travis S.J. Gabriel[1], Ann Ollila[3], Susanne Schröder[5], Olivier Beyssac[6], Erin Gibbons[7], David S. Vogt[5], Elise Clavé[8], Jose-Antonio Manrique[9], Carey Legett IV[3], Paolo Pilleri[2], Raymond T. Newell[3], Joseph Sarrao[3], Sylvestre Maurice[2], Gorka Arana[10], Karim Benzerara[11], Pernelle Bernardi[12], Sylvain Bernard[11], Bruno Bousquet[8], Adrian J. Brown[13], César Alvarez-Llamas[14], Baptiste Chide[2], Edward Cloutis[15], Jade Comellas[3], Stephanie Connell[15], Erwin Dehouck[16], Dorothea M. Delapp[3], Ari Essunfeld[3], Cecile Fabre[17], Thierry Fouchet[12], Cristina Garcia-Florentino[10], Laura García-Gómez[14], Patrick Gasda[3], Olivier Gasnault[2], Elisabeth Hausrath[18], Nina L. Lanza[3], Javier Laserna[14], Jeremie Lasue[2], Guillermo Lopez[9], Juan Manuel Madariaga[10], Lucia Mandon[12], Nicolas Mangold[19], Pierre-Yves Meslin[2], Marion Nachon[20], Anthony E. Nelson[3], Horton Newsom[21], Adriana L. Reyes-Newell[3], Scott Robinson[3], Fernando Rull[9], Shiv Sharma[22], Justin I. Simon[23], Pablo Sobron[24], Imanol Torre Fernandez[10], Arya Udry[18], Dawn Venhaus[3], Scott M. McLennan[25], Richard V. Morris[23], Bethany Ehlmann[26]

[1]U. S. Geological Survey Astrogeology Science Center, Flagstaff, Arizona, USA
[2]Institut de Recherche en Astrophysique et Planetologie (IRAP), Université de Toulouse, UPS, CNRS, Toulouse, France
[3]Los Alamos National Laboratory (LANL), Los Alamos, New Mexico, USA
[4]Globe Institute, University of Copenhagen, Copenhagen, Denmark
[5]Institute of Optical Sensor Systems, DLR, Berlin, Germany
[6]Institut de Minéralogie, de Physique des Matériaux et de Cosmochimie (IMPMC), Université Pierre-et-Marie-Curie (UPMC), Paris, France
[7] McGill University, Montreal, Quebec, Canada
[8]Centre Lasers Intenses et Applications, CNRS, CEA, Univ. Bordeaux, Bordeaux, France
[9]University of Valladolid, Valladolid, Spain
[10]University of Basque Country (UPV/EHU), Leioa, Bilbao, Spain
[11]Institut de Minéralogie, de Physique des Matériaux et de Cosmochimie, Muséum National d'Histoire Naturelle, CNRS, Sorbonne Université, Paris, France
[12]Laboratoire d'Etudes Spatiales et d'Instrumentation en Astrophysique, Observatoire de Paris, CNRS, Sorbonne Univ., Univ. Paris-Diderot, Meudon, France
[13]Planicus Research, Severna Park, Maryland, USA
[14] UMALASERLAB, Department of Analytical Chemistry, University of Málaga, Málaga, Spain
[15]University of Winnipeg, Manitoba, Canada
[16]Univ. Lyon, Univ. Lyon 1, ENSL, CNRS, LGL-TPE, Villeurbanne, 69007 Lyon, France
[17]GéoRessources, CNRS, Univ. Lorraine, Nancy, France
[18]University of Nevada, Las Vegas, Nevada, USA
[19]Laboratoire de Planétologie et Géodynamique, Université de Nantes, Université d'Angers, CNRS UMR 6112, Nantes, France
[20]Texas A&M University, College Station, Texas, USA

[21]University of New Mexico, Albuquerque, New Mexico, USA
[22]University of Hawaii, Manoa, Hawaii, USA
[23]Astromaterials Research and Exploration Science (ARES) Division, NASA Johnson Space Center, Houston, Texas, USA
[24]SETI Institute, Mountain View, California, USA
[25]State University of New York (SUNY) Stony Brook, New York, USA
[26]Division of Geological and Planetary Sciences, California Institute of Technology, Pasadena, California, USA

Abstract

The SuperCam instrument on the *Perseverance* Mars 2020 rover uses a pulsed 1064 nm laser to ablate targets at a distance and conduct laser induced breakdown spectroscopy (LIBS) by analyzing the light from the resulting plasma. SuperCam LIBS spectra are preprocessed to remove ambient light, noise, and the continuum signal present in LIBS observations. Prior to quantification, spectra are masked to remove noisier spectrometer regions and spectra are normalized to minimize signal fluctuations and effects of target distance. In some cases, the spectra are also standardized or binned prior to quantification. To determine quantitative elemental compositions of diverse geologic materials at Jezero crater, Mars, we use a suite of 1198 laboratory spectra of 334 well-characterized reference samples. The samples were selected to span a wide range of compositions and include typical silicate rocks, pure minerals (e.g., silicates, sulfates, carbonates, oxides), more unusual compositions (e.g., Mn ore and sodalite), and replicates of the sintered SuperCam calibration targets (SCCTs) onboard the rover. For each major element (SiO_2, TiO_2, Al_2O_3, FeO_T, MgO, CaO, Na_2O, K_2O), the database was subdivided into five "folds" with similar distributions of the element of interest. One fold was held out as an independent test set, and the remaining four folds were used to optimize multivariate regression models relating the spectrum to the composition. We considered a variety of models, and selected several for further investigation for each element, based primarily on the root mean squared error of prediction (RMSEP) on the test set, when analyzed at 3 m. In cases with several models of comparable performance at 3 m, we incorporated the SCCT performance at different distances to choose the preferred model. Shortly after landing on Mars and collecting initial spectra of geologic targets, we selected one model per element. Subsequently, with additional data from geologic targets, some models were revised to ensure results that are more consistent with geochemical constraints. The calibration discussed here is a snapshot of an ongoing effort to deliver the most accurate chemical compositions with SuperCam LIBS.

Contents

1. Introduction

The SuperCam instrument suite on the Mars 2020 rover Perserverance [1] includes the second remote laser-induced breakdown spectroscopy (LIBS) instrument to operate on another planet. In addition to LIBS, SuperCam capabilities include visible and infrared reflectance spectroscopy, time-resolved Raman and luminescence spectroscopy, remote imaging, and acoustic recording [2,3]. SuperCam's first use was followed closely by the MarSCoDe instrument suite on the Zhurong rover, which consists of a LIBS instrument, an infrared spectrometer, and an imager [4]. Both instrument suites have LIBS instruments patterned after ChemCam [5,6], which has been used on Mars since 2012 as part of the payload of the Mars Science Laboratory rover *Curiosity*.

SuperCam contributes to three Mars 2020 mission science goals: to study the geology and geochemistry of Jezero crater; to investigate habitability, materials with biosignature preservation potential, and evidence of past life; and to assemble a cache of returnable samples, including searching for the best samples and documenting their geological context and general character [1]. The SuperCam investigation's specific goals include rock identification; characterization of sedimentary stratigraphy and alteration, morphology, and texture; the search for organic molecules and biosignatures; characterization of volatile elements; and investigation of surface varnishes and coatings, regolith, igneous history, and atmospheric properties. LIBS contributes to all of these goals as described in [2].

SuperCam's instrument architecture is similar to ChemCam's but with notable changes to facilitate SuperCam's additional functionality. Both instruments consist of an internal body unit containing the spectrometers and an external mast unit with the laser and 110 mm aperture telescope to acquire observations of targets around the rover. SuperCam's telescope is improved compared to ChemCam, enabling a slightly smaller laser footprint on targets with its ~12 mJ, 1064 nm, 3-4 ns long laser pulse [2]. Plasma light is transmitted from the telescope to the spectrometers in the body of the rover via a ~6 m optical fiber and an optical demultiplexer [3]. Both ChemCam and SuperCam use a trio of spectrometers to cover wavelengths between ~240 and 850 nm at similar wavelength resolution. The ultraviolet (UV) and violet (VIO) spectral ranges on both SuperCam and ChemCam are covered by nearly identical Czerny-Turner [7]

spectrometers and ungated detectors. Unlike ChemCam, which uses a third Czerny-Turner spectrometer, SuperCam uses a transmission spectrometer with a gated intensifier to cover the ~535-850 nm range. This spectrometer enables remote time-resolved Raman spectroscopy. This spectrometer has similar resolution to ChemCam over much of that range but has a factor of 2 better resolution in the Raman range from 535 to ~610 nm. In addition to superior resolution, the transmission spectrometer affords other advantages, including reduced collection of ambient light (sunlight) due to a shorter exposure (10 μs is used for LIBS). The disadvantage of the intensifier is increased noise relative to ChemCam's bare CCD (charge-coupled device). The transmission spectrometer transmits light into three spectral ranges (Green, Orange, and Red), thus using nearly three times the number of spectral channels relative to ChemCam (Table 1), which uses ~2000 channels over a larger spectral range. SuperCam cannot acquire simultaneous LIBS and Raman spectra even though both use the same spectrometer, because the laser is frequency doubled and its beam path is changed for the Raman observations. Table 1 summarizes the SuperCam spectrometer spectral ranges and number of spectral channels in a typical LIBS Calibrated Data Record (CDR) product. These values are valid for both Mars spectra and the laboratory spectra used here.

Table 1: Overview of SuperCam LIBS calibrated data record (CDR)

Spectrometer	Abbreviation	Wavelength range (nm)	# of spectral channels after stitching	Range of channel indices used in stitching
Ultraviolet	UV	243.79 - 341.36	2040	n/a
Violet	VIO	379.26 - 464.54	2037	n/a
Green	VNIR	537.57 - 619.82	1237	600-1837
Orange		620.08 - 712.14	1114	471-1587
Red		712.17 - 852.77	1505	345-1850

A key advantage of SuperCam's LIBS system is the inclusion of a much larger number of onboard calibration targets that cover a greater compositional range than ChemCam's. The 23 LIBS targets include pure igneous mineral compositions, basaltic targets doped with trace elements, and a number of targets simulating typical rock compositions [8,9]. A titanium plate is included for wavelength calibration as was done on ChemCam. These onboard targets are not adequate to train a regression model, but they provide ground-truth comparisons that can be used to evaluate calibration models under martian conditions.

The *Perseverance* landing site, Jezero crater, appears to differ substantially in rock type and composition from Curiosity's landing site in Gale crater. Like Gale crater (e.g., [10–12]), Jezero crater was once a large lake, as indicated by a notable deltaic formation and outflow channel

which demonstrates that the crater was filled with water (e.g., [13–15]). However, the local chemistries appear to be different. The Curiosity rover has encountered three main stratigraphic groups in Gale crater: the Bradbury group, the Mount Sharp group, and the Siccar Point group [10]. The Bradbury group consists of sorted detrital plagioclase-phyric basaltic sedimentary rocks transported from the crater rim [16,17]. The composition of the Stimson formation in the Siccar Point group is similar to the Mars global dust composition, and it consists of lithified aeolian dunes [16]. The Murray formation, which constitutes much of the Mount Sharp group is a dominantly lacustrine formation that has a relatively consistent silica-rich subalkaline basalt composition that is distinct from the Bradbury group: with a more silica-rich basaltic source rich in plagioclase and Fe, low in Ca and Mg (e.g., [18]). By contrast, from orbit, Jezero crater's upstream regions contain olivine and pyroxene, areas of Jezero crater just inside the rim have a distinctive Mg carbonate signature, and the crater floor farther from the rim appears to have an olivine-rich mafic unit (e.g., [19]). The team thus expects minerals rich in Mg such as olivine and its alteration-pathway minerals, e.g., serpentine and talc [20] as well as Mg-rich clays, and C (carbonates; e.g. [21–23]). To address these expectations, we tuned both the onboard targets and the overall spectral library with more carbonates and Mg-rich compositions.

1.1. Overview

This paper provides an overview of the current state of the SuperCam team's ongoing efforts at developing quantitative calibration models for the major element oxides (SiO_2, TiO_2, Al_2O_3, FeO_T, MgO, CaO, Na_2O, K_2O), and possible next steps. We first discuss the challenges of quantitative LIBS and the different approaches to calibration. This is followed by a description of the laboratory setup and details regarding the collection of a diverse database of LIBS spectra used to train and test the calibration models. We then discuss the preprocessing steps applied to the spectra, followed by the organization of spectra into training and test sets and the assessment of data quality and removal of outliers. We discuss the multiple regression algorithms tested and how models were tuned and selected for optimal performance. Finally, we discuss the results of applying the selected models to data on Mars and potential next steps in our effort to improve the accuracy of SuperCam LIBS quantification.

1.2. The Challenges of Quantitative LIBS

Deriving quantitative elemental abundances of geologic targets from LIBS spectra is challenging, both because of the nature of the stand-off LIBS technique itself and the nature of the targets being analyzed. The distance to the target and target properties influence the recorded LIBS spectra. The laser spot size, and therefore the laser irradiance on the target, varies with distance: the spot size is ~170 μm at 2.4 m and increases to ~370 μm at 5.5 m [15]. The amount of energy absorbed by a target per laser pulse is also strongly dependent on the target opacity and albedo at the laser wavelength. Some materials absorb the laser well, but others, particularly those with large crystals that are transparent or translucent to the laser, may be absorbed poorly or not at all (e.g. [23,24]) resulting in low signal to noise or a lack of any discernible LIBS signal. Moreover, the laser spot size is often bigger than the individual crystals or grains in the geologic sample which can lead to heterogeneous mixtures in the targets probed.

An additional challenge is that LIBS spectra record a process that is inherently transient: the laser-induced plasma evolves rapidly during and after the laser pulse, changing in temperature, density, and opacity [26]. Furthermore, the ions, atoms, and molecules in the plasma interact with each other, causing the intensity of emission lines from any given element to depend on the presence and concentration of other elements. Unconsolidated materials such as regolith/soil or dust present an additional challenge; although they may absorb the laser well, the shock wave from the laser ablation alter the material surface for subsequent laser shots and create a pit that confines the plasma and changes its properties compared to an unconfined plasma generated on a hard surface (the conditions under which our spectral database was acquired). Collectively the chemical and physical effects that can complicate the simple relationship between emission line strength and elemental abundance are called “matrix effects” [27].

For terrestrial LIBS applications, it is possible to mitigate these analytical challenges by, e.g., sample preprocessing, control of observation repeatability, and possibly by selection of calibration samples that are matrix matched to specific targets of interest. For SuperCam and other planetary LIBS instruments, these strategies are not available, but key features of LIBS (e.g., speed, remote compositional analysis, and no sample-preparation requirements) led to SuperCam’s selection as part of the rover payload.

Even when the laser is absorbed well and a quality LIBS spectrum is collected, quantifying the compositions of rocks and minerals is challenging compared to LIBS applications in industrial settings, where the range of compositions is relatively well constrained and the materials themselves are homogeneous in terms of their physical properties and composition. Although most Mars rocks are composed primarily of silicates and have a roughly basaltic composition (e.g., [27–29]), experience from Gale crater with ChemCam shows that “extreme” compositions (often pure minerals) are observed and are scientifically interesting targets (e.g. [31–33]). An ideal quantification for Mars targets should be accurate for “typical” basaltic rocks, for pure silicate minerals such as olivine and plagioclase, and also for “unusual” non-silicate compositions such as manganese-, iron-, and titanium-oxides, sulfates, and carbonates.

Considering the range of variations in observational parameters and the expected heterogeneity of samples expected at Jezero crater, a physics-based approach like “calibration-free LIBS” (CF-LIBS; e.g., [34]) might seem attractive. However, the SuperCam instrument is not suitable for CF-LIBS because the whole plasma evolution from initiation to extinction is recorded in each spectrum, rather than only acquiring the spectrum during a narrow time-gate of the plasma evolution. Furthermore, not all contributing components in martian targets are easily quantified by LIBS (e.g., sulfur, or carbonates in a CO_2-dominated atmosphere), making the self-normalization implied in CF-LIBS problematic [35]. For these reasons, we have not investigated the use of CF-LIBS for the quantitative calibration model for SuperCam.

1.3. Multivariate vs Univariate Calibration

Our calibration approach was to seek an empirical calibration trained on data collected in the laboratory. Empirical calibrations can be “univariate” or “multivariate.” Univariate calibration relates a single variable such as intensity at a given wavelength, or the integrated intensity of a

fitted emission line, to the abundance of the element of interest. Multivariate models instead incorporate information from many emission lines, and potentially from the entire spectrum, to predict elemental abundances.

Univariate models have the advantage of being simple and easy to interpret, and the user has complete control over which emission line is used. However, although univariate models can be effective for minor and trace elements with few weak emission lines (e.g., [31,36]), they tend not to perform as well as multivariate models for major elements [37]. Multivariate models can incorporate information from the entire spectrum, including emission from elements other than the element being predicted, to mitigate matrix effects outlined above.

Both univariate and multivariate models run the risk of giving spurious predictions for new data, either due to the prediction model being overfitted (i.e. tuning the parameters such that the model performs well on the training set but does not handle novel data well) or because the new observation represents an unusual composition relative to the samples on which the model was trained. If trained on a large and representative data set, the multivariate models have superior performance [37,38]; we therefore chose to focus our efforts on the multivariate approach for the major element calibrations discussed in this paper.

2. Experimental

2.1. Setup

The multivariate models used to extract quantitative chemical compositions are developed from a spectral library of pressed rock powder and synthetic standards with known chemical compositions. This spectral library was acquired prior to delivery of the SuperCam instrument to the rover for assembly and integration. Data acquisition was performed in Los Alamos National Laboratory using the flight Body Unit (i.e. the unit now in the *Perseverance* rover on Mars) containing the spectrometers, and an Engineering Qualification Model (EQM) of the Mast Unit (MU) containing the laser and telescope [2,3]. Differences between the EQM and flight versions of the MU are minor. The most significant is that the flight MU uses an aluminum primary mirror surface, while the EQM uses a nickel-coated aluminum mirror similar to ChemCam's [5]. The flight mirror is an all-aluminum mirror because it was determined after the EQM build that the nickel coating resulted in a slight degradation of the shape of the mirror at its normal temperature on Mars (where it is maintained at ~-35ºC) relative to the optimum shapeat room temperature on Earth. The change in mirror surfaces resulted in a noticeable improvement in the resolution of the Remote Micro-Imager (RMI) images at Mars temperatures, but the change in laser beam size was not noticeable; however, it may have had a small but unquantified effect on the LIBS. The other effect of the all-Al mirror surface was a slight loss (~10%) in reflectivity in the UV range. Both flight and test setups were corrected for their respective optical responses, compensating for this and any other differences in optical response.

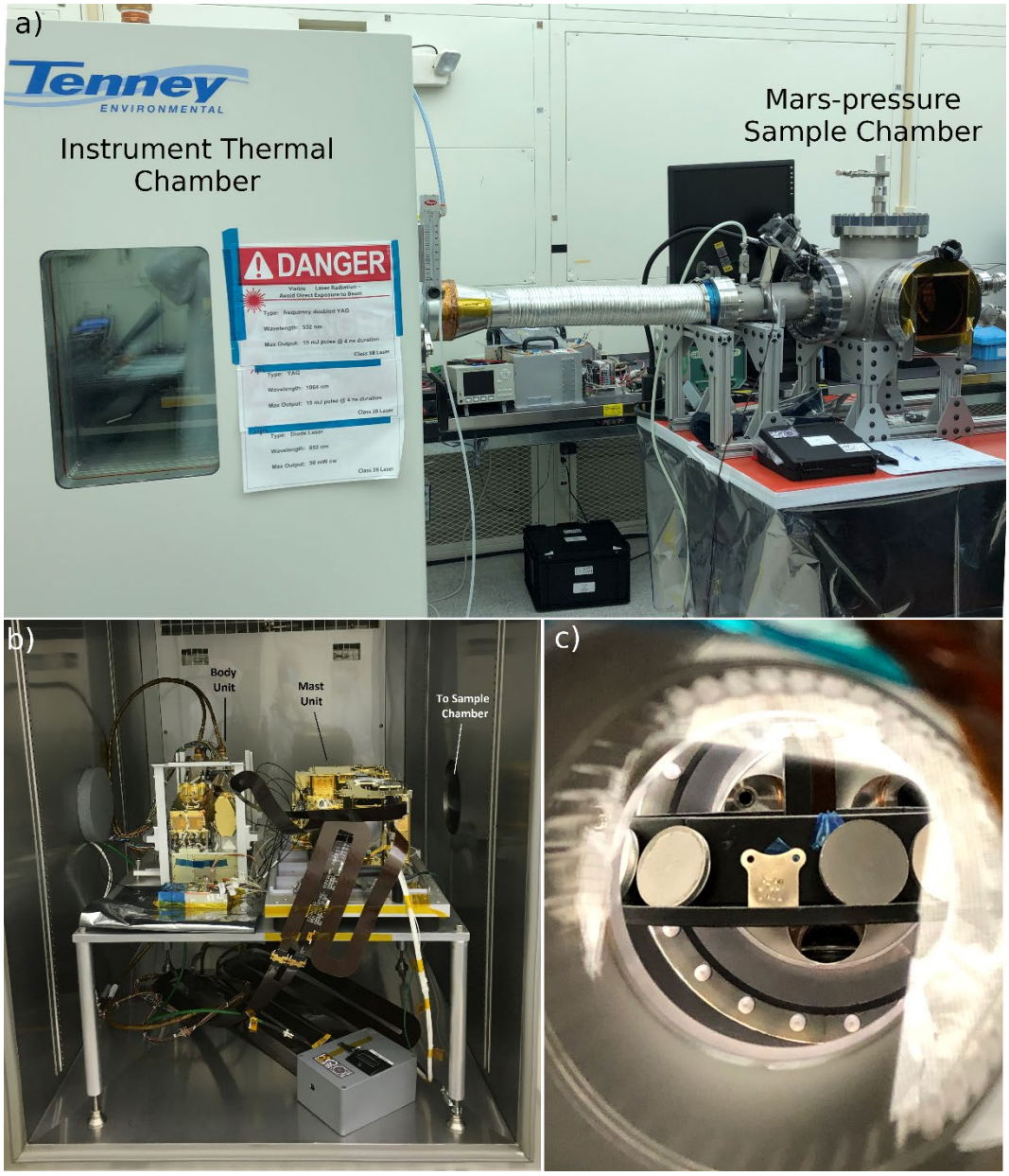

Figure 1: Photographs of the laboratory setup: (a) environmental chamber, with a tube connecting to the chamber containing standards to be analyzed; (b) SuperCam inside the environmental chamber and (c) view down the connecting tube of several pressed powder samples and a Ti plate ready for analysis. Photo credit: R. Wiens.

The experimental arrangement is shown in Figure 1. Because the SuperCam laser is designed to give optimum performance at “Mars-like” temperatures in the -30 to +10ºC range, the instrument was maintained in a thermal chamber for laboratory measurements. The Body Unit was in the chamber too, since the detectors should be operated at temperatures below 0°C. It was observed during early testing that the compressor of the thermal chamber vibrated the instrument slightly, causing the laser beam position on the target to vary by up to ~500 μm at

nominal target distances. To provide consistent pointing such that successive pulses hit the same location, the thermal chamber was cooled to -15ºC and turned off while observations were made of two targets, at which point the chamber was re-cooled to -15ºC before repeating with the next two targets. The chamber temperature never exceeded -7ºC

Samples were placed in the Mars chamber (Figure 1), which accommodated ~16 pressed pellets (30 mm diameter) plus a Ti plate control sample. The chamber was sealed and evacuated to <100 mTorr (~10 Pa) pressure. Gas was introduced to bring the pressure to 5.5 Torr (733 Pa, the mean surface pressure at Jezero crater) using CO_2, maintaining that pressure with dynamic pumping so that the gas in the chamber was constantly refreshed. This minimizes moisture and removes volatiles produced during ablation to minimize contamination of the chamber window. Pressure was read by a vacuum gauge, which is calibrated for terrestrial air composition (80% N_2). Pressure curves for CO_2 indicate that a reading of 3.5 Torr corresponds to an actual pressure of 5.5 Torr. The pressure was maintained within ±3%. Relative humidity in the room was low (~20%); however, the pressed powder standards were stored without desiccants, and notable hydrogen peaks in otherwise anhydrous standards suggest that the pressed powders contained some adsorbed and/or absorbed water.

To be consistent with SuperCam optical geometry and to avoid unnecessary optical aberrations, we used only a single window between the instrument and the samples, similar to the remote warm electronics box (RWEB) window on the rover. To achieve this configuration while keeping the targets at Mars pressure and keeping the instrument at Mars-like temperatures, a tube was installed to enclose the beam path between the thermal chamber and the sample chamber. The tube kept warm, humid air from entering the thermal chamber near the aperture of the instrument, which would have resulted in condensation there. The tube extended to the window of the sample chamber at Mars pressure (Figure 1). Different lengths of tubing were available, so that targets could be observed at different distances.

Focusing was performed manually by setting the focus stage to the approximate distance to the target, firing the laser, and checking the signal strength. Small adjustments to the focus were made in the forward and backward directions to find the strongest signal. The focus was kept at this position over a period of several days during the measurement campaigns, checking the strength of the signal from a control sample (titanium plate) to ensure that focus was maintained from one day to the next. The LIBS campaign was interrupted before the last standards were observed, and upon resumption, a distance of 3.0 m was used instead of the original 2.85 m, and a relatively small number of standards were observed at this slightly longer distance. In the analyses discussed here, the data at 2.85 and 3.0 m are grouped together and referred to as the “3 meter” data set.

2.2. Data for the spectral library were collected between 9 and 21 April 2019. Three separate locations were analyzed on each standard, collecting 30 active and 30 non-laser (“dark”) spectra from each location. The average spectrum for each location was calculated, excluding the first five points to minimize surface contamination (e.g. adsorbed water). In a few cases, four locations were probed if there was any question of the validity of the first three observations. The laser was energized with a current of 140 A, which yields 12 mJ of energy measured on target at Mars-like temperatures after passing through the telescopic system and the window between the thermal chamber and the sample chamber. For the UV and VIO spectral ranges, signal was collected over 200 rows of the detectors with an integration time set to 34 µs, although without a shutter, the effective integration time was much longer due to the CCD readout time of several milliseconds. For the transmission spectrometer, the intensifier gain was set to 2500 (See [3] for details regarding instrument gain). The gate was set to open at the same time as laser firing by setting the delay to 650 ns relative to an arbitrary start time. The intensifier gate (exposure duration) was 10 µs, and the CCD exposure duration was 4.9834 ms to allow time for the intensifier phosphor glow to decay before transferring data. Additional details of the instrument operation are provided by Maurice et al. and Wiens et al. [2,3].Description of Standards

The SuperCam calibration database comprises 334 samples. Most of the standards used in this library come from the database built for the ChemCam calibration [38]. These standards include powdered geologic materials provided by several laboratories, in addition to those purchased from Brammers and U.S. Geological Survey. A variety of igneous, sedimentary, and metamorphic rock types are represented, as well as multiple mineral types: primary igneous minerals (olivines, pyroxenes, and feldspars of various compositions), carbonates (limestone, dolomite, and aragonite), phyllosilicates (nontronite/smectite, kaolinite), sulfates (gypsum and mixtures of sulfate and basalt), phosphates (apatite, heterosite/purpurite), oxides. These samples are described in detail in [38], and are grouped by different mineralogies in (Table 9 in [3]). Samples were prioritized to cover the expected mineral types in Jezero crater identified from orbital spectroscopy, rock types common on Mars, and compositions found at previous landing sites. An attempt was made to cover the geochemically relevant range for each element (Figure 2) but, for several elements, certain compositional ranges (in particular, high concentrations) are underrepresented, making accurate quantification in these ranges challenging. Additional standards may need to be analyzed to improve the calibration in these ranges.

Replicates of the onboard SuperCam Calibration Targets (SCCTs) [8,9] as well as several additional calibration targets that are not onboard the rover are also included in the spectral

library. These samples are not pressed powders, but sintered powders that make them more durable. These calibration targets include primary igneous minerals, some standards, some natural rocks (serpentine, chert, carbonates), an apatite, some basaltic mixtures doped in minor elements, and a mixture between a basaltic standard with a sulfate [8,9].

A table containing the compositions and other metadata for all targets in the calibration database is included in the supplementary material. The individual .fits files for each of the laboratory observations, as well as a single .csv file containing compositions, metadata, and spectra, are available at the SuperCam PDS archive: https://pds-geosciences.wustl.edu/missions/mars2020/supercam.htm

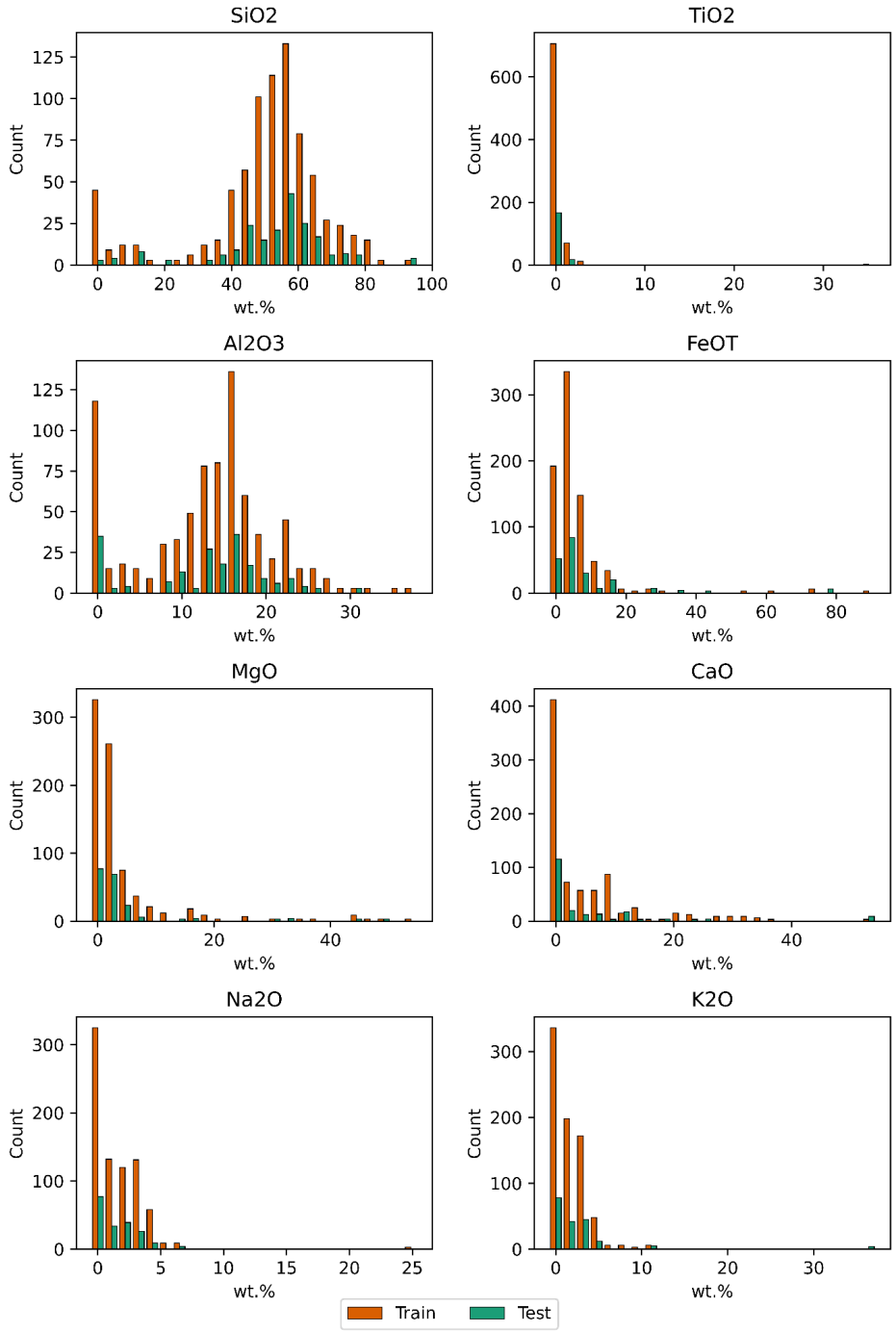

Figure 2: Histograms showing the distribution of compositions in the laboratory data training and test sets for each major element oxide.

2.2.1. Spectral Variability

The performance of our calibration models depends on the diversity of the library of spectra on which they are trained and their similarity to spectra collected on Mars. Given that the spectra have thousands of wavelength channels but the underlying chemical variability is of far lower dimensionality (most natural samples have a small number of major elements, and the emission lines from a given element tend to be highly correlated), we can use dimensionality reduction techniques to simplify exploration of library data and comparison with data from Mars. Principal Component Analysis (PCA; [39–41]) allows us to capture the spectral response to chemical variability by finding a set of only a few principal components that encapsulate most of the variability of the data set. The first step in the PCA process is to compute an MxM variance-covariance matrix based on the library spectra, where M is the dimensionality of the spectra (the number of spectral channels). This symmetric matrix relates the variability in one wavelength bin to that of all other bins, illustrating their covariance with one another. For example, if Fe content tends to be lower when Si content is higher, it is likely that the covariance of the wavelength bins in those spectral lines/features will have a large negative and positive covariance respectively. If Fe content is independent of Si content, the covariance will be near zero. Once the variance-covariance matrix is computed, an eigenvector decomposition of the matrix is performed, where a set of M linearly independent unit vectors with length M (eigenvectors) are computed and their scalar multiples (M eigenvalues) are computed. In PCA, each eigenvector is sorted according to their eigenvalues and the first few eigenvectors (PCs) reflect the greatest variability in the underlying data set.

Before the PCA process, each spectral range was normalized to its respective sum. In Figure 3 we show the amount of variance in the normalized library spectra that is represented by the first several components and we show the first two eigenvectors (referred to as ‘loadings’ in PCA) for the UV region of the LIBS spectra. The first two components together explain 60% of the variance in the library spectra and the first ten components explain 95% of the variance. In Figure 4 we show the projection of all library spectra into the principal component space of PC1 and PC2. The maximum extent of the hull or “outline” of the library is defined by a few SCCTs due to their “extreme” pure mineral end-member compositions. Some general compositional groupings and trends can also be identified (Figure 4), for example, with metal oxides and olivines having high PC2 values and carbonates and sulfates, having large PC1 values. These groupings are not strict, and the loadings should be studied for a more detailed understanding of the location of a given spectrum on the scores plot. The clinopyroxene calibration target, for example, is near the (predominantly Ca-bearing) carbonates and sulfates due to their calcium contents. As shown in Figure 3, the first component is strongly correlated with Ca content.

To understand whether the library data set encompasses observations on Mars, we plot the PC1 versus PC2 scores of all LIBS points acquired in Jezero crater up to Sol (solar day of the mission) 147 in Figure 5 with the hull of the library overlain. Nearly all Mars spectra plot well within the library hull, demonstrating that the extent of the library is likely sufficient in terms of its spectral variability in the dominant components. None of the points that fall outside the hull are dramatically distinct from the library: they do not appear to represent a separate class

of materials that would require special analysis. It is worth noting that most of the observations on Mars are centered near the igneous rock compositions, with some notable excursion into end-member compositions at high values in the first two components.

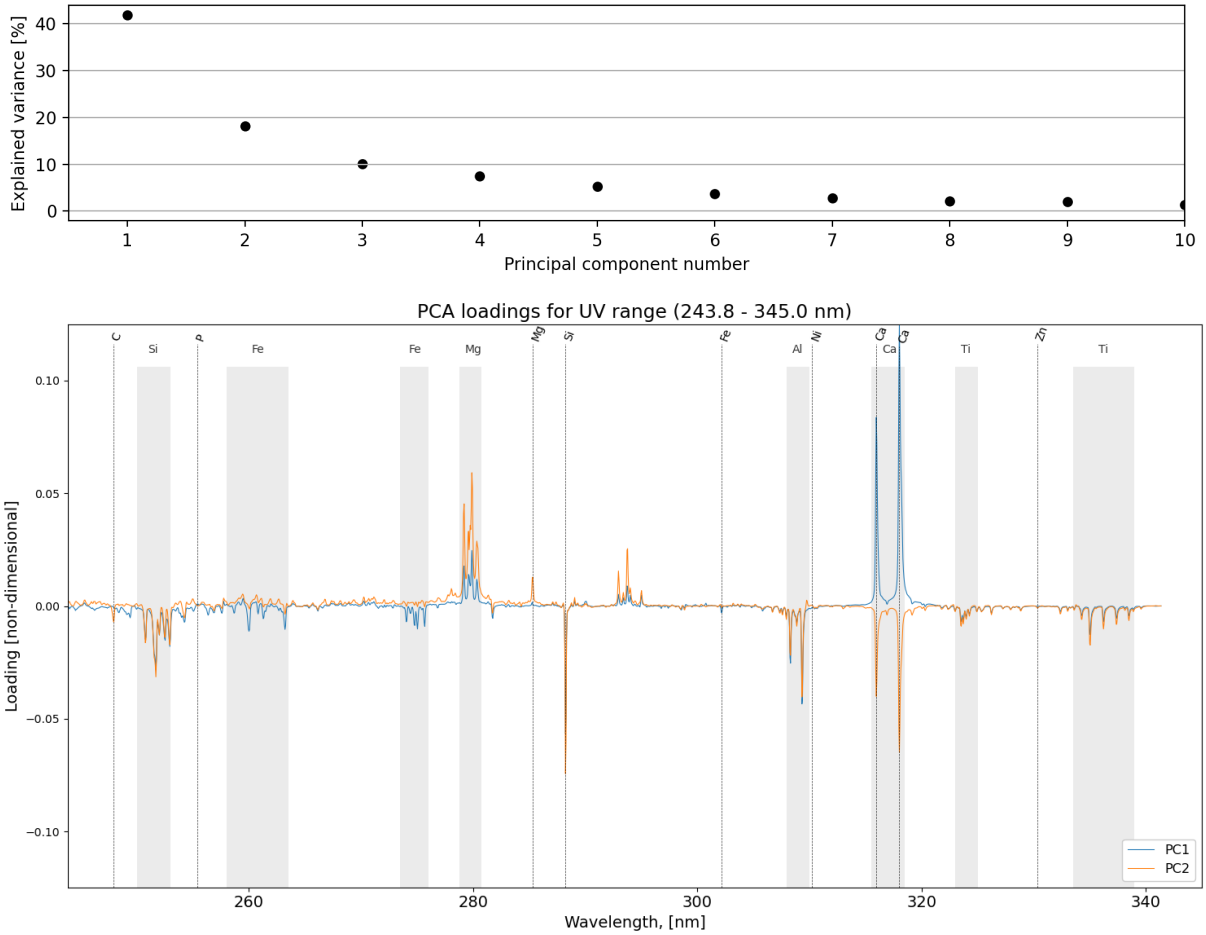

Figure 3: (Top) The amount of variance in the library spectra explained by each principal component. (Bottom) Loadings of the first two principal components across the UV range. The first principal component is strongly correlated with Ca signal and the second is anticorrelated with Ca signal. Both PCs show correlations and anticorrelations in other elements.

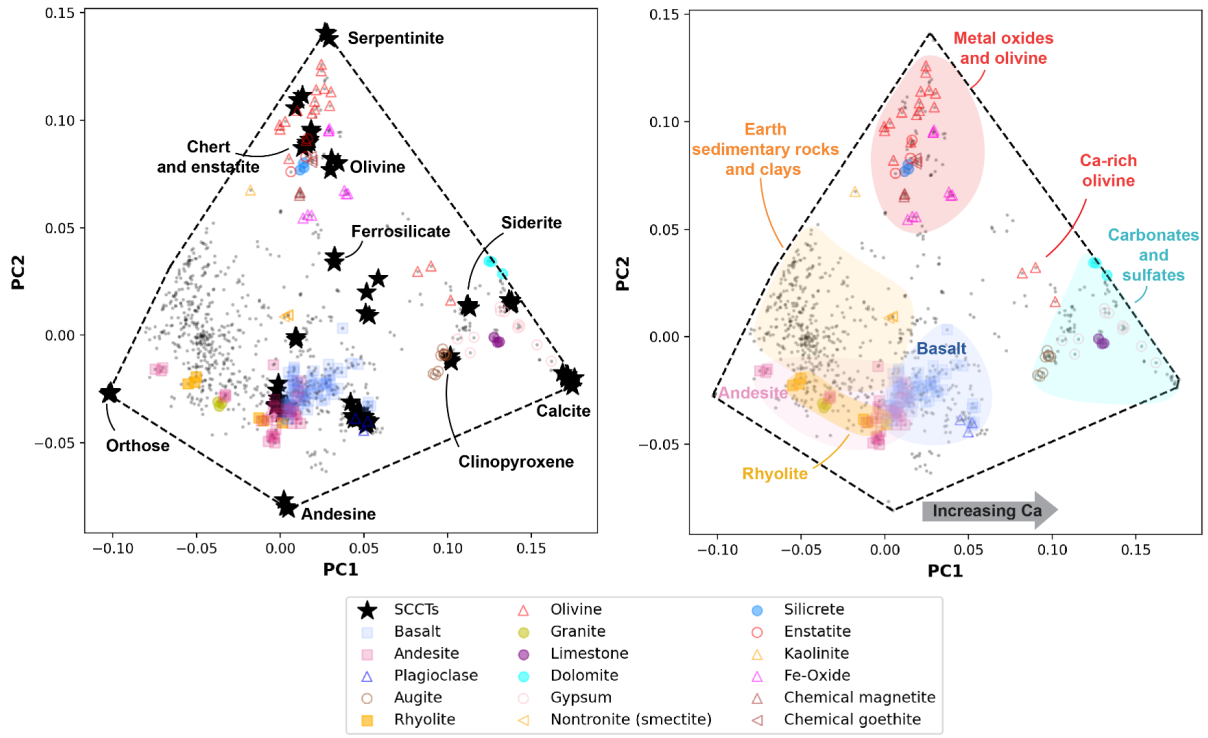

Figure 4: (Left) All library points (grey dots) projected onto the first two PCs with selected sample types denoted by a range of colors and symbols (see legend). Black stars represent SuperCam Calibration Target (SCCT) samples in the laboratory with selected samples labeled. The dashed line represents the convex hull of all the library points. (Right) Same data without the SCCTs highlighted. Groupings of samples are shown by shaded regions, based on the colored symbols, however these regions are not strict. The first principal component is strongly indicative of the calcium line strength in the LIBS spectra.

441

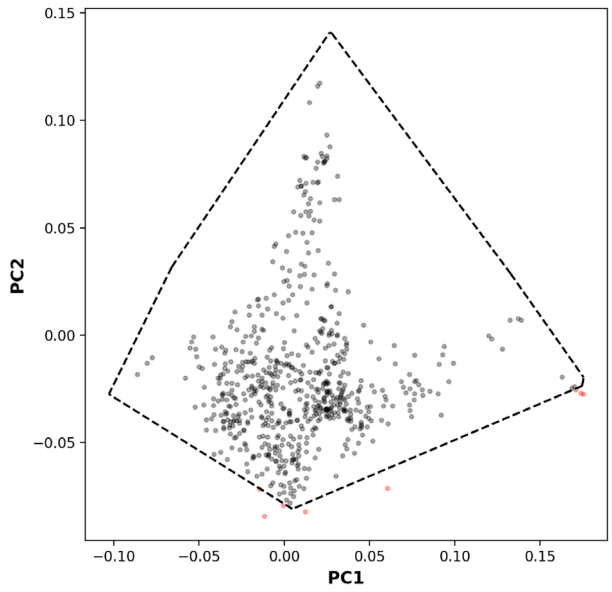

Figure 5: All of the SuperCam LIBS data (circles) from Mars, up to sol 147, projected into the principal component space of the LIBS library (see Figure 4). The convex hull of the library is shown by the dashed line. Only very few observations on Mars fall out of the convex hull of the LIBS library database in this projection (red circles), indicating that the library is generally comprehensive with respect to the LIBS spectral variability observed in targets on Mars.

3. Data Processing

3.1. Preprocessing

3.1.1. Non-laser dark subtraction

SuperCam is commanded to take a non-laser “dark” spectrum immediately after the LIBS spectra using the same spectrometer settings as the active spectrum, but without the laser firing. This is not a true dark spectrum because light is still falling on the detector, but it serves a similar purpose, allowing the fixed background signal of the instrument and ambient light to be removed. Signal and darks for a given observation are stored in the same data file. Dark spectra are averaged and then the mean spectrum is subtracted from each of the active collects. The dark subtraction also removes an offset of 300-500 digital numbers (DNs; counts produced by the analog-to-digital converter in the SuperCam instrument) which is added in the analog-to-digital conversion to ensure that the converter does not encounter negative values.

3.1.2. Stitching

In the intensified transmission spectrometer, the light is split into three bands: the band closest to the CCD serial register is referred to as the “Red” region and covers 707-853 nm; in the

center is the “Green” region covering 530-618 nm, and at the other side of the CCD is the “Orange” region covering 598-720 nm[3]. The three bands overlap and are stitched together to obtain a spectrum that has monotonically increasing wavelengths. The transition between spectrometers is selected with two main criteria: 1. Given the choice between two spectrometers, we want to use the higher signal to noise data as indicated by the Instrument Response Function (IRF; see below); 2. To ensure a smooth spectrum, we want to transition between spectrometers in a zone where no emission lines are present. The final spectral channel indices used for the three ranges are listed in Table 1.

3.1.3. Denoising

To remove low level random signal variation across the spectrum (white noise), we use a “stationary” wavelet transform analysis to decompose the spectrum, remove noise, and then reconstruct the spectrum. The stationary wavelet transform is particularly useful for identifying noise [42,43] and the method we use for SuperCam is almost identical to that performed for ChemCam data reduction [44].

Wavelet analysis involves a convolution of the signal with orthogonal basis functions (wavelets) that have both scale and frequency properties. The process results in an invertible transform that can be considered as a series of band pass filters with a response function that is uniform in shape (a constant-shaped wavelet) but variable in scale and frequency. Using the orthogonality properties of the basis function, a spectrum can be completely characterized by the wavelet basis function and associated coefficients determined through the decomposition process.

A scaling function $\phi(x)$ and a wavelet function $\psi(x)$ are used for the wavelet transform. The continuous scaling function satisfies the following equation:

$$\phi(x) = \sqrt{2}\sum_n h(n)\,\phi(2x - n)$$

where *h(n)* is the low-pass filter, x are the spectral channels, and n is the level of the wavelet decomposition.

The continuous wavelet is defined in terms of the scaling function and the high-pass *g(n)* QMF through:

$$\psi(x) = \sqrt{2}\sum_n g(n)\,\psi(2x - n)$$

In the standard “discrete” wavelet transform (DWT), the input signal is broken down into a series of decomposition levels. At each level *L*, the wavelet has a resolution reduced by a factor of 2^L with respect to the original signal. That is, if the signal is defined across 100 nanometers, at level L=2, the wavelets will have a length of $100/2^L$ or 25 nanometers. At each level, the wavelet decreases in size, providing greater resolution of high frequency or sharper spectral features (Figure 6).

One downside to the discrete wavelet transform that is relevant to spectral noise characterization is that all levels are required in the reconstruction of the signal (i.e. the levels are “non-redundant”) and the loss of the translation-invariance property in the DWT leads to a large number of artifacts when a signal is reconstructed after modification of its wavelet coefficients. This is undesirable for denoising because the goal is to isolate the noise, remove it, and reconstruct the signal without noise. We instead use a stationary or undecimated form of the wavelet transform [45] in which each level is redundant, with higher levels containing information necessary to deconstruct the signal in the previous level. Thus, in the context of spectral analysis, the levels can be inspected to distinguish between salient features, e.g., emission lines and white noise. We direct the reader to [46] for a mathematical description and a comparative discussion of discrete and stationary wavelet analysis for an analogous noise characterization analysis.

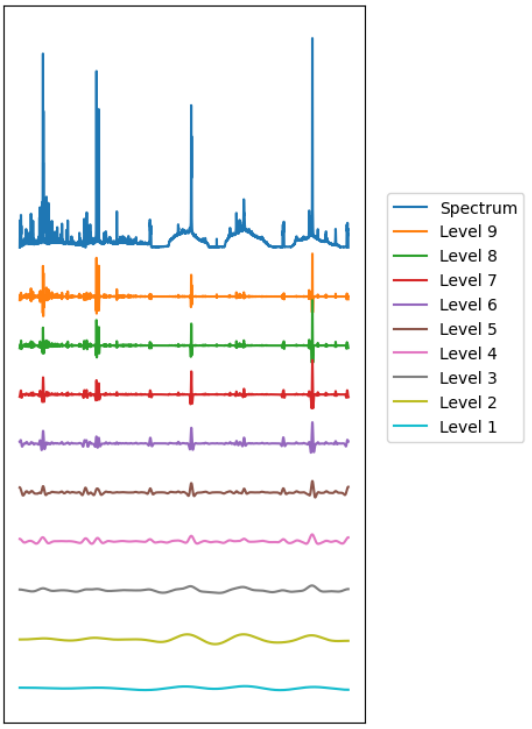

Figure 6: Illustration of the wavelet decomposition of a LIBS spectrum, with vertical offset applied to each level. Horizontal axis is wavelength, vertical axis is intensity. Numerical values are omitted because the decomposition is applied prior to wavelength calibration or conversion to physical units.

In our application of the stationary transform, the wavelet coefficients are found by calculating the difference between two successive scaling passes. The scaling function used is a B_3-spline, and the associated low-pass filter h is defined in terms of its z-transform as:

$$h(z) = 1/16(z^{-2} + 4z^{-1} + 6z^0 + 4z^1 + z^2)$$

We use the second generation of the transform described by [45] which is more robust to artefacts than other wavelet-based denoising methods. The z-transform of the high-pass filter g is:

$$g(z) = 1/256(-z^4 - 8z^3 - 28z^2 - 56z^1 + 186z^0 - 56z^{-1} - 28z^{-2} - 8z^{-3} - z^{-4})$$

This differs from the high-pass filter used in [44]:

$$g(z) = 1/16(-z^{-1} - 6z^0 + 16z^1 + 6z^2 + z^3)$$

For more details on the stationary wavelet transform and its implementation, refer to [45].

At each scale, noise is identified and removed using “sigma clipping” as described in [47,48]. We calculate the standard deviation of the absolute value of the wavelet spectrum at a given decomposition scale and identify those spectral channels with values less than three times the standard deviation. This process is repeated iteratively on the channels that fall below the threshold several times to arrive at an estimate of the standard deviation of the noise in the wavelet spectrum at each scale. Then, values in the wavelet spectrum below three times the standard deviation are set to zero. Once this has been applied to each scale of the wavelet decomposition, the de-noised spectrum is reconstructed by summing the wavelet scales.

Figure 7 illustrates the result of denoising applied to a spectrum acquired on Mars. The figure shows a small subset of the spectrum so that the noise and the difference between the original and denoised spectrum can be seen. The average absolute change in signal for this spectrum after denoising is ~8 DNs.

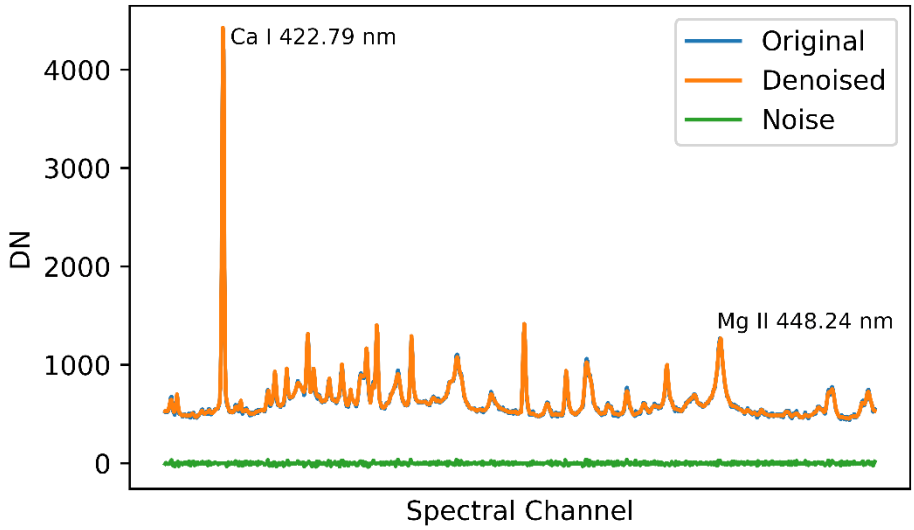

Figure 7: Example illustrating the effect of denoising. This figure shows a subset of the EDR spectrum of the target Máaz, in the 420 - 450 nm range. Vertical axis is intensity, horizontal axis is wavelength. Denoising is applied prior to wavelength calibration so we omit the numerical values on the x axis. The two strongest emission lines in this range are labeled.

3.1.4. Instrument Response Function and Conversion to Radiance

SuperCam spectra are converted to physical units of radiance (W/cm^2/sr/nm) prior to quantitative analysis. The conversion from photons to radiance is similar to that described in section 2.3.4 of [44]. First, the recorded CCD signal in DN (digital number) is converted to photons using the Instrument Response Function (IRF).. Figure 8 shows the IRF for the three spectrometers. After the IRF has been applied, the spectrum is divided by the integration time, area on target, solid angle subtended by the telescope, and spectral channel width for each CCD column. Finally, photons/s is converted to watts using $E = hc/\lambda$ for each spectral channel. The calculation of both the area of the target visible from the telescope and the solid angle subtended by the telescope as seen from the target include the distance to the target, so applying the conversion to radiance includes an implicit correction for distance for the light emitted by the plasma spark.

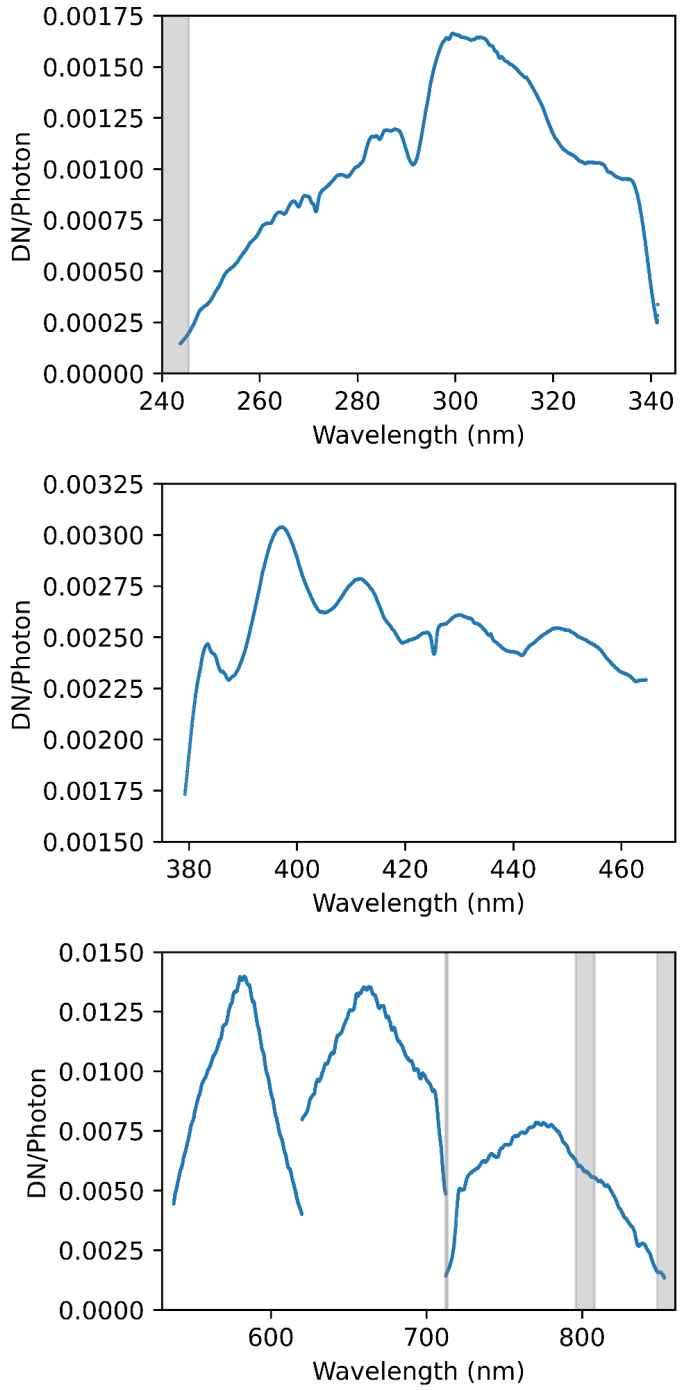

Figure 8: SuperCam instrument response function (IRF) for the three spectrometers. Gray rectangles indicate portions of the spectrum that are masked before quantification (see the “Additional Preprocessing for Quantification” section).

541

3.1.5. Continuum Removal

Laser-induced plasma emission contains a background continuum due to primarily to ion-electron recombination processes. In SuperCam spectra, this is most notable in the three transmission spectrometers. This continuum shows some correlation with chemical composition [49,50], but is more strongly influenced by the amount of laser energy absorbed by the target (e.g. due to distance or focus). We have found that removing the continuum prior to normalization helps to mitigate these variations. We use the same continuum removal procedure described by [44].

The continuum removal algorithm is based on the same wavelet decomposition as the de-noising algorithm described above. It works by decomposing the spectrum to a specified scale and then finding the local minima of the decomposed spectrum at that scale. Then, minima are found in the original input spectrum within windows of $\pm 2^L$ around each local minimum from the decomposed signal, where L is the wavelet scale. A cubic spline is fit to these minima and subtracted from the input spectrum. For each wavelet scale, beginning with the largest scale and continuing to lower scales until reaching a specified minimum scale, the process is repeated iteratively until the standard deviation of the corrected spectrum stops changing significantly or a maximum number of iterations is reached. The advantage of this algorithm is that it is fast and relies on very few parameters. Figure 9 illustrates how the removed continuum evolves with each additional scale.

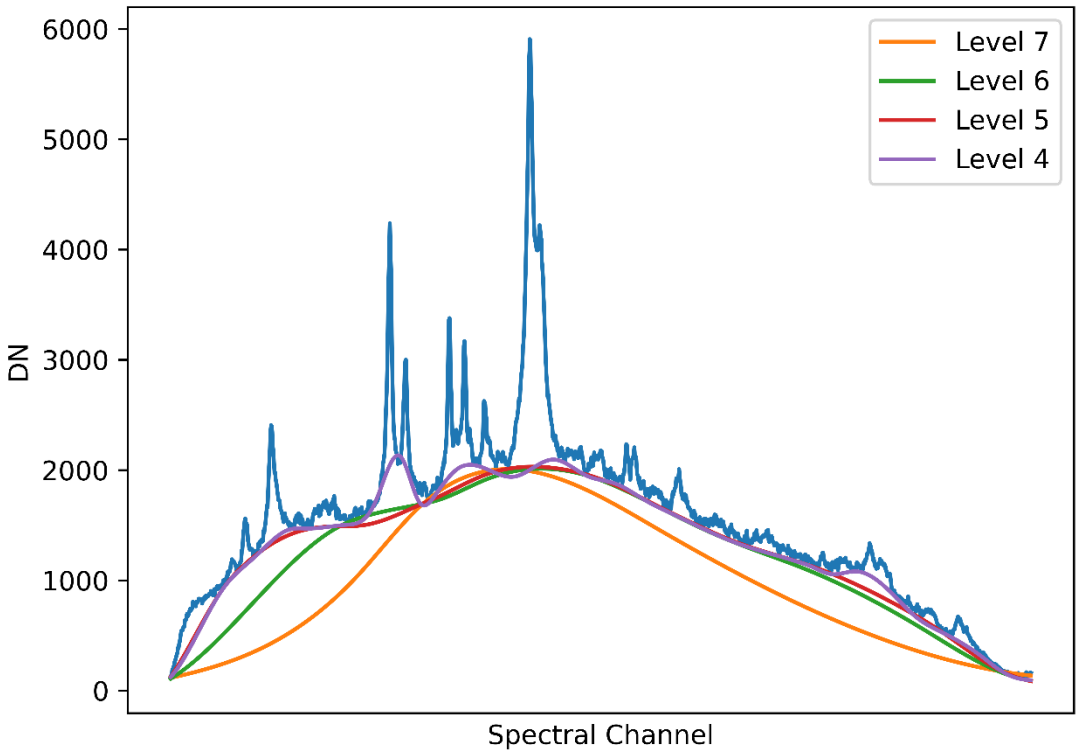

Figure 9: Illustration of how reducing the minimum wavelet scale results in a continuum which more closely follows small-scale variations in the spectrum. The level 4 continuum fits the spectrum too closely, while the continuum at levels 6 and 7 does not fit closely enough. This figure shows a subset of the Orange spectrometer. Wavelength values are omitted from the x axis because continuum removal is applied prior to wavelength calibration.

The default parameters for the minimum wavelength scale for continuum removal are 6 for the UV and VIO spectral ranges, and 5 for the three transmission spectrometer ranges (Green, Orange, Red). Increasing this parameter produces a smoother continuum, but a lower number gives a continuum that follows the spectrum more closely (Figure 9).

3.1.6. Wavelength Calibration

Wavelength calibration is performed by comparing the spectrum to be calibrated with a reference spectrum. The reference spectrum can be either a real spectrum acquired by the instrument or a synthetic spectrum built from lines of interest. In either case, the known positions of the emission lines are mapped to spectral channel indices using a pattern recognition algorithm, and a continuous wavelength distribution is fit to these index-wavelength pairs. The procedure is an updated version of the method described in section 2.3.3 of [44]. We

use the vacuum wavelengths of the emission lines from the NIST spectral database [51] rather than the wavelengths in air at 1 bar because all data were acquired at martian atmospheric pressure (6 mbars).

The UV and VIO ranges of the calibration database are calibrated against a spectrum acquired on a titanium plate. Titanium is well suited for the UV and VIO ranges because it contains a large number of emission lines in these ranges. For the Green, Orange and Red spectrometers, we used synthetic spectra built with emissions lines of identified elements in the respective ranges. The wavelength calibration of the laboratory database serves as a reference for all the spectra acquired on Mars.

Wavelength calibration for the flight instrument was calculated using LIBS spectra from a titanium plate and two additional targets: IlmHem which is a mixture of ilmenite and hematite, and ClinQzOrth which is a mixture of clinozoisite quartz and orthoclase. These spectra were collected during the rover System Thermal Test in October 2019. Because wavelength calibration alters the distance in wavelength space covered by each channel, we re-sample the calibrated spectrum onto the baseline channel-to-wavelength map. Finally, the spectra are re-interpolated over the reference wavelength defined for the calibration database so that the wavelengths of the Mars and laboratory data have precisely the same wavelength values.

On Mars, we observe slight changes in wavelength calibration as a function of temperature. Figure 10 shows the average absolute pixel (spectral channel) shift calculated for the UV and VIO ranges for all active LIBS sequences taken up to sol 147 of the mission. The median of the average shift is 0.16 pixel for the UV range, and 0.2 pixel for the VIO range. All values remain well within $\pm$ 0.5 pixel shift in the UV range, and within $\pm$ 1 pixel shift for the VIO range. The transmission spectrometer calibrations have been checked to be robust to temperature variations and typically present an average shift of about 0.02 pixels per degree, much lower than for the UV and VIO ranges. Given the small observed shifts, the wavelength calibration for SuperCam spectra is not currently adjusted for temperature.

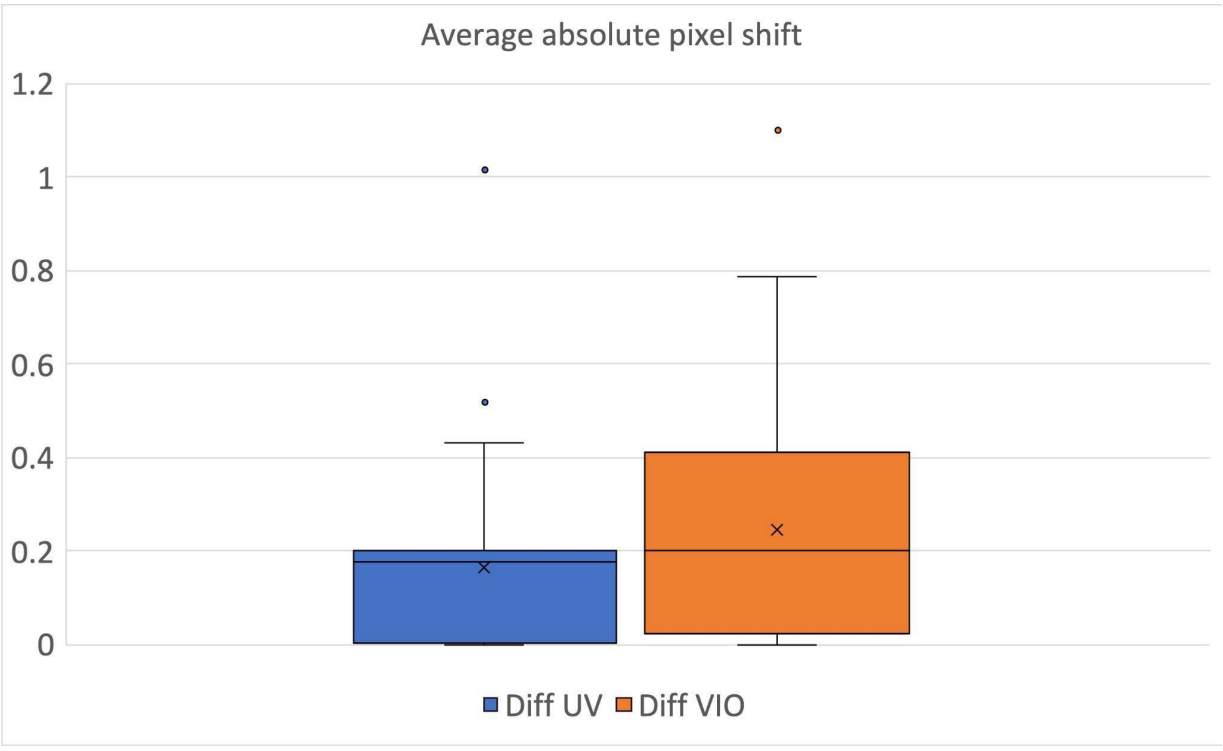

Figure 10: Boxplot of the average absolute pixel shift detected for all SuperCam active LIBS sequences up to sol 147 on Mars. The average shift calculated for these spectrometers remain well within +/- 1 pixel. The transmission spectrometer exhibits a much smaller shift than the UV and VIO spectrometers.

3.1.7. Additional Preprocessing for Quantification

In addition to the preprocessing applied to all spectra, we also applied several additional steps prior to training regression models. The first is masking: to ensure that quantification is based on the highest-quality data, we defined a mask to remove portions of the spectra with lower signal to noise, based on investigation of the instrument response function (Figure 8), while also retaining key emission lines, such as the Ti lines at the long-wavelength end of the UV range. We masked out the UV spectrometer for wavelengths less than 245.5 nm and the Red spectrometer for regions where the instrument response is <1/5 the best instrument response value for the Red spectrometer. This results in the removal of Red spectrometer data between 712.17 nm and 714 nm, and for wavelengths >848.3 nm. No masking was required for the VIO, Green, or Orange spectrometers. There was also an anomalous feature in some of the laboratory data in the wavelength range 796 nm ≤ λ ≤ 808 nm that was masked.

We also normalized each spectrum. This involves dividing the portion of the spectrum from each spectrometer by the total signal from that spectrometer. We treat the three spectral ranges of the transmission spectrometer separately, so we have five spectral ranges for normalization. Thus, after normalization is applied, the full spectrum across all five spectral ranges sums to 5.

Normalization helps to mitigate fluctuations in signal between observations and partly reduces the effect of distance on the spectrum.

We also experimented with applying standardization and peak binning to the spectra. Peak binning is an algorithm originally developed for ChemCam analysis as a fast and simple alternative to fitting and summing all of the individual peaks in a spectrum [52]. It works by calculating an average training set spectrum and using that average spectrum to identify the wavelength values of local minima and local maxima. Each individual spectrum is then binned: the signal between pairs of local minima is summed, and the resulting value is assigned to the wavelength of the local maximum. In this way, the full spectrum (>7900 spectral channels after masking) can be replaced with a “spectrum” of summed values (~560 channels). This has the benefit of significantly reducing the size of the spectrum and collecting the signal from each line into a single value, increasing robustness to small shifts in wavelength calibration. Peak binning may also increase model sensitivity to broad or weak lines [52]. We applied peak binning prior to normalization. Regression models with and without peak binning were evaluated for all elements, but it did not always improve the accuracy of the quantification.

Standardization involves subtracting the average value and dividing by the standard deviation for each spectral channel, resulting in a spectrum where each channel has a mean value of 0 and a standard deviation of 1. The mean and standard deviation are calculated based on the training set spectra, and the same values are used to standardize unknown spectra to be predicted. Standardization can help with regression in some cases by equalizing the influence of all spectral channels on the model. It reduces the magnitude of very bright emission lines and amplifies portions of the spectrum with few or weak emission lines. The resulting spectra and regression coefficients are less intuitive for human interpretation but can lead to improved regression models. Standardization was applied after normalization. As with peak binning, we evaluated models with and without standardization for each of the major elements, but it did not always improve the results.

We also shifted the wavelength calibration of the training spectra by $\pm$ 1 to 3 pixels and used both the shifted and unshifted data to train models. The observed variation in wavelength calibration on Mars is small (Figure 10), but we found that models trained on shifted spectra did not suffer in performance when predicting unshifted data but were more robust to shifts in wavelength if they were to occur, so most of the models considered were trained on spectra with shifts of up to 1 or 2 pixels.

3.2. Data Organization

One challenge for developing an empirical multivariate calibration is determining the optimal parameters to use for the regression algorithms considered. Many algorithms are susceptible to “overfitting” - tuning the parameters such that the model performs well on the training set but does not handle novel data well. To tune model parameters while avoiding overfitting, we use k-fold cross validation [53] in which the data are split into k roughly equal-sized parts or “folds.” We used five folds, defined separately for each major element. The exact number of folds used has been shown to have little effect on the performance of the final model as long as both the

training set and test set provide a good representation of the sample variability [54]. We "stratified" the data by sorting on the abundance of the element of interest, so that when the samples are sequentially assigned to the folds, the result is that the distribution of compositions is as similar as possible (Figure 11). This helps to reduce the likelihood that all of the samples with the highest concentration of the element being predicted do not end up in one fold, causing it to behave dramatically differently than the other folds. To some extent this situation is unavoidable, given the "long tail" of higher compositions for many elements, but stratification minimizes the effect. All spectra of the same target are grouped together when defining the folds to ensure that the folds are independent

We held out one of the folds as a "test set" which is used for model selection and estimation of accuracy only after cross validation and model tuning have been completed. All rover calibration targets were kept in the test set so spectra from Mars can be used to assess model performance.

The cross-validation process involves stepping through the remaining four folds, holding out one at a time, training a model based on the other three folds, and predicting the held-out data. This gives an estimate of how the final model, trained on all four folds in the training set, will perform on unknown data. The optimum parameters for a given algorithm can be determined by examining how the root mean squared error of cross validation (RMSECV) varies with different settings. When the RMSECV is similar for multiple different settings of a model, the least-complex model was adopted.

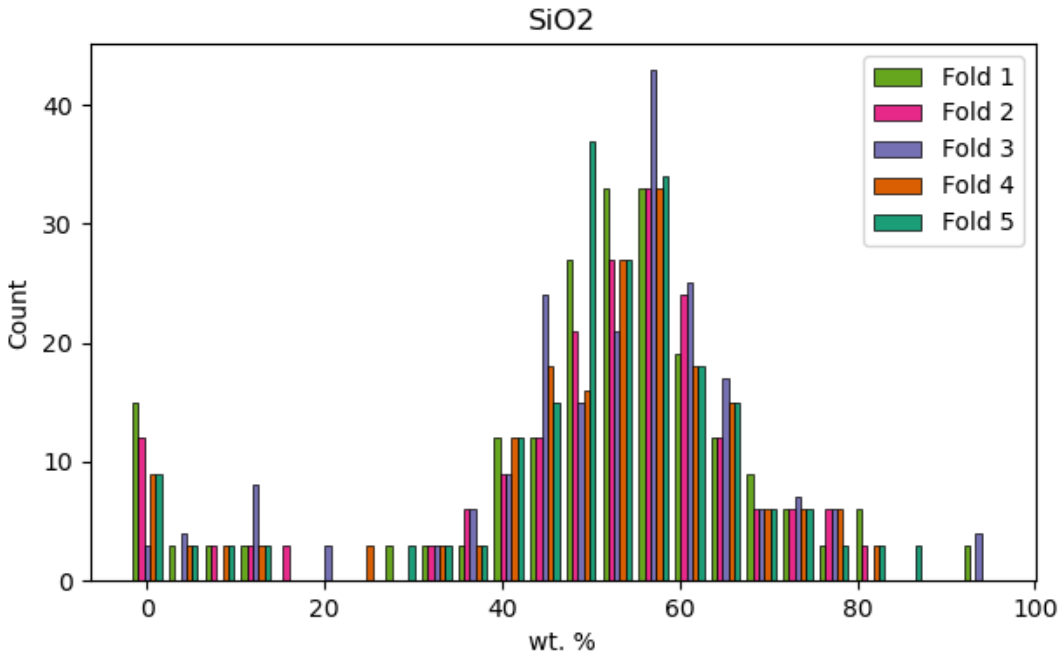

Figure 11: Histogram showing the similar distribution of SiO_2 concentrations in the five folds.

3.2.1. Outlier Removal

We use several approaches to determine whether certain samples should be considered "outliers" in the development of our models for each element. First, we evaluate the data quality to determine if each spectrum is valid to use at all. Some spectra exhibit low total signal, low signal to noise, and anomalous curvature in the continuum of the UV spectrometer and are marked for potential removal, although they were not removed until after the outlier identification steps described here were applied.

We next evaluate target homogeneity by running a PCA analysis on the full data set and qualitatively inspecting the PC1 vs PC2 score plots to visualize how tightly grouped the points for a given target were. This analysis allowed us to remove several anomalous spectra. In other cases, the points for a given target exhibited considerable variation on the scores plot. If one point was significantly different from the others, it was removed while the homogeneous points were kept. In cases where all spectra from a target showed significant scatter, we took this as an indication that the target was not sufficiently homogenized during preparation; thus, the reference composition may not match the composition of the spots analyzed. For these cases, all spectra for the target were removed.

We also used several outlier identification approaches to more quantitatively identify potentially problematic spectra. Two of these were algorithms available through the scikit-learn Python library: local outlier factor (LOF) and isolation forest (IF) [55,56]. LOF works by calculating the distance from each spectrum to its nearest neighbors and comparing with the average distance to the nearest neighbors of the nearest neighbors. Outliers are expected to be farther from their neighbors than average. IF works by randomly splitting the high-dimensionality point cloud of spectra until the spectrum of interest is isolated. An outlier tends to require relatively few splits to isolate, while a spectrum that is more "typical" will be in the dense part of the cloud and require more splits to isolate. We ran both algorithms on the normalized spectra, with parameters set so that they would flag 10% of the spectra as potential outliers. We then removed those spectra that were flagged by both methods. Many of the spectra flagged by LOF and IF as potential outliers were also identified above as having low signal.

Another approach to outlier identification is to generate a partial least squares (PLS) model and plot the Q residuals against the Hotelling T^2 values for each spectrum. For this, we used PLS_toolbox 8.9 (Eigenvector Research Inc.) for MATLAB R2020b (MathWorks Inc.). For a model that represents the spectra X using loadings P and scores T, with an error matrix E

$$X = TP^{\mathsf{T}} + E$$

Q residuals are defined as

$$Q_i = e_i e_i^{\mathsf{T}} = x_i\left(I - P_k P_k^{\mathsf{T}}\right)x_i^{\mathsf{T}},$$

where e_i is the error for the ith spectrum, x_i is the ith spectrum, I is the identity matrix, and P_k are the loadings for the k components of the model. Q_i is a summary of how well the selected

components model the spectrum, with larger values indicating a spectrum that is not handled well by the model.

Hotelling's T^2 statistic is defined as

$$T_i^2 = t_i \lambda^{-1} t_i^\top = x_i P_k \lambda^{-1} P_k^\top x_i^\top$$

where t_i refers to the i-th row of the scores matrix T, and λ is the matrix of eigenvalues corresponding to the k of components in the model. T_i^2 reflects the leverage of a spectrum on the model.

Outliers on the Q vs T^2 plot are points that plot far away from the origin, particularly those with high values of both Q and T^2, indicating that the spectrum has a significant amount of influence on the model (high T^2) but is still poorly predicted by the model (high Q).

A similar approach to calculating Q is to train a PLS model and identify training set samples that are poorly predicted by the model. For each major element, we used both the Q vs T^2 and the training set approach and flagged potential outliers. Spectra flagged as outliers for many or all of the major elements using these two model-based methods were removed completely from all models. These spectra included ilmenite, a mix of quartz and cobaltite, a Mn oxide, and sodalite. If these model-based methods flagged a spectrum as an outlier for only a small number of the major elements, then that spectrum was removed for those elements but kept for other element models.

One of the challenges of defining outliers is how to handle high-quality spectra from samples that are very different from the average. In our data set, these tend to be mineral samples with unusually high concentrations of one element. These spectra may be flagged as outliers because they are either poorly modeled or they exert an undue influence on the model, but they are valid data and may improve the model performance at high concentrations at the expense of the performance at low concentrations. Thus, we found it useful to handle these samples differently depending on the model being trained. We remove them from fixed models intended to accurately predict low concentrations but retain them for models restricted to high concentrations, and for local regression models, which dynamically adjust the samples being used to match the unknown spectrum (see below). To define which samples should be handled in this way, we established a threshold for compositions to be considered "high" compared to the rest of the data set. For each element, we calculated the median and standard deviation of the composition across all standards in the database. Standards were considered "high" concentration if they had values greater than 1 standard deviation above the median value. Spectra that were both "high" in composition based on this criterion and flagged as outliers were removed when training models intended to predict the full range (0-100 wt.%) for an element but were kept for high-concentration submodels and local regression models. In total, out of 1198 individual spectra, 54 were removed from all major element models. The number of spectra removed for each of the major elements is listed in Table 2. For "high" models, fewer spectra are removed because those identified as high concentration are retained.

Table 2: Outliers removed from laboratory data set

	# of Outlier Spectra	# of Outlier Spectra (for “High” models)
SiO_2	102	92
TiO_2	114	112
Al_2O_3	101	89
FeO_T	102	94
MgO	97	78
CaO	125	100
Na_2O	120	116
K_2O	115	97

4. Quantification

4.1. Algorithms

No single multivariate regression algorithm is clearly the best choice for all major elements. For our work toward a quantitative prediction model for each major element, we take the approach of trying a wide variety of algorithms and choosing the model or models that give the best results. We first discuss the algorithms in this section and in the next section we discuss the criteria used to select the preferred model. The algorithms considered are listed in Table 3. We used the Python library scikit-learn [57] to implement these algorithms.

Table 3: Regression algorithms and abbreviations

Algorithm	**Abbreviation**
Ordinary Least Squares	OLS
Partial Least Squares	PLS
Least Absolute Shrinkage and Selection Operator	LASSO
Ridge regression	Ridge
Elastic Net	ENet
Orthogonal Matching Pursuit	OMP
Support Vector Regression	SVR

Random Forest	RF
Gradient Boosting Regression	GBR
Local Elastic Net	Local ENet
Blended submodels	Blend

Ordinary Least Squares (OLS) is the simplest approach to multivariate regression. For the *n* spectra *x* with *p* spectral channels, it seeks to find the regression coefficients *w* to predict the composition *y*:

$$y_{i,predict} = w_0 + w_1 x_{1i} + w_2 x_{2i} + w_3 x_{3i} + \cdots + w_p x_{pi}$$

while minimizing the sum of squared residuals:

$$\sum_{i=0}^{n} \left(y_{i,predict} - y_{i,true}\right)^2 = \sum_{i=0}^{n} \left(x_i w - y_{i,true}\right)^2$$

OLS tends to perform poorly when there is a high degree of correlation between the features in the data, which is a common situation when working with spectroscopic data. However, we included OLS as a point of comparison for other more sophisticated algorithms.

Least Absolute Selection and Shrinkage Operator (LASSO; Tibshirani, 1996) is one of several methods that seek to improve upon OLS by adding a “regularization” term, which seeks to impose constraints or certain behaviors on the regression model. LASSO adds a term consisting of a constant (α) multiplied by the sum of the absolute values of the regression coefficients *w*.

$$\sum_{i=0}^{n} \left(x_i w - y_{i,true}\right)^2 + \alpha \sum_{j=0}^{p} \left|w_j\right|$$

Minimizing this regularized equation has the effect of simplifying the model by setting many of the regression coefficients to zero. The value of α adjusts how strongly the regularization term is weighted, and therefore how sparse the solution is. A sparse model has the benefit of being easier to interpret and potentially faster, while still performing well [59].

Ridge regression [60] imposes a different form of regularization to the model, the sum of the squares of the regression coefficients:

$$\sum_{i=0}^{n} \left(x_i w - y_{i,true}\right)^2 + \alpha \sum_{j=0}^{p} w_j^2$$

This has the effect of penalizing models in which certain coefficients are significantly larger than the others, which in turn can make the model more robust to correlation between x variables (spectral channels)

Elastic Net (Enet; [61]) combines the Ridge and Lasso regularizations, using the parameter ρ to control their relative strengths:

$$\sum_{i=0}^{n}\left(x_i w - y_{i,true}\right)^2 + \alpha(1-\rho)/2\sum_{j=0}^{p} w_j^2 + \alpha\rho\sum_{k=0}^{p}|w_k|$$

Orthogonal Matching Pursuit (OMP) [62,63] seeks to minimize the least squared error, with a constraint on the total number of non-zero regression coefficients. It iteratively selects spectral channels, with each additional channel chosen to be orthogonal to previously selected channels and highly correlated with the remaining residual.

Partial Least Squares (PLS; [63]) is a regression method that is closely related to PCA and has previously been used successfully for LIBS calibration (e.g., [37,43,64,65]). Like PCA, PLS seeks to reproject high-dimensionality data (spectra) into a lower-dimensionality space. However, unlike PCA, PLS seeks a projection that maximizes the correlation between each component in the x space and the composition y. PLS handles data with a large number of highly correlated independent variables well, and thus is commonly used with spectroscopic data.

Support vector regression is based on the Support Vector Machine (SVM), in which data are projected into a space where they can be effectively separated using a hyperplane [67,68]. For regression, this hyperplane defines a region around the prediction within which errors are not penalized. This allows the algorithm to focus on reducing the largest errors rather than making insignificant improvements on predictions that are already close to the true value.

We used two ensemble methods as well: Gradient Boosting Regression (GBR; Friedman, 2002, 2001) and Random Forest (RF; Breiman, 2001), both of which are based on decision trees [72]. To build a decision tree, a series of binary splits (“branches”) are chosen. For regression trees, it is common to choose a split that minimizes the variance. Once the decision tree is built, an unknown spectrum begins at the tree “trunk,” and follows the set of branches, eventually arriving at a “leaf”, which represents the prediction result. Decision trees have the disadvantage of overfitting test data if the hierarchy is too deep. To prevent this overfitting, rather than using a single decision tree, ensemble methods form predictions from a combination of multiple decision trees. See [72] for more details on decision trees.

In RF regression [71], a set of decision trees is created by training on random subsets of the training set and using random subsets of the input variables (spectral channels) as well. Taking the average of a larger number of randomized decision trees generally causes their individual errors to balance out, yielding an accurate regression model without suffering from overfitting.

GBR [69,70], on the other hand, is a technique for repeatedly adding decision trees so that the next decision tree corrects errors in the prediction from the previous decision tree. This is done using “boosting" [73] which is a technique that aggregates models developed sequentially on a given learning task, with the weights assigned to the input data adjusted as new models are added. At each step of the process, a new model is added and fit to the negative gradient of a

loss function. The loss function can be the mean squared error (MSE) which is not robust to outliers, the mean absolute error (MAE) which is robust to outliers, or the Huber loss function which transitions from MAE to MSE at a specified threshold [74].

As discussed above, one of the main challenges in developing a regression model for predicting the composition of geologic materials on Mars is the wide range of potential compositions. Models trained on a restricted range of compositions tend to perform well within that range, but very poorly outside the training range. Models trained on a diverse set of samples, on the other hand, tend to perform better overall, but within a specific range a specialized model may still do better. For the calibration of the ChemCam instrument, we developed a "submodel" approach to make use of this behavior [65]. By training several models on restricted ranges of composition, and then using a single overarching model as a "first guess" to determine which submodel is most appropriate for a given prediction, we can often improve the overall accuracy. The disadvantage of the submodel approach is that it is relatively involved, requiring the cross validation of several models, optimization of the blending of multiple models, and trial and error to determine which algorithms and which training set ranges give the best results.

Local ENet is an algorithm that we developed as an alternative to the relatively involved process of using blended submodels. It generates a new elastic net model for each unknown spectrum being predicted, using the N most similar spectra in the training set, where N is a user-specified number of nearest neighbors. The individual models are optimized using the automatic cross validation capabilities of the implementation of Elastic Net in scikit-learn. Local Elastic Net is inspired by the LOCAL algorithm [75], in which a weighted average of PLS models is used in a similar manner. Local Elastic Net regression is time consuming since it trains many individual models, but it has the advantage that it can adapt the training set to be as similar as possible to the unknown spectrum without the need for human involvement. Our implementation of Local ENet is available as part of the Python Hyperspectral Analysis Tool (https://github.com/USGS-Astrogeology/PyHAT).

To investigate the behavior of regression models, it is useful to see which spectral channels influence the model the most. For the linear models above (PLS, Ridge, LASSO, Enet, OMP) we use the vector of regression coefficients *w* that is multiplied by each spectrum to yield a predicted composition. These can be plotted as a function of wavelength much like a spectrum to see which parts of the spectrum have a strong positive or negative correlation with the prediction. Ensemble methods do not have a perfectly analogous vector, since they comprise many decision tree models. Instead, the scikit-learn implementation of GBR and RF provides a "feature importance" or "Gini importance" vector. This is a vector of values that indicates which spectral channels had the greatest influence on the model, but it is not a vector of weights that is multiplied by the spectrum to yield a prediction.

4.2. Model Selection

With such a large variety of regression algorithms, the process of selecting between the models for each element is very important. As discussed above, we use cross validation on the training set to optimize the parameters of each model to minimize the RMSECV. Once the parameters

are set, we use the optimized models to predict the test set. The Root Mean Squared Error of Prediction (RMSEP) of those test set predictions is the primary basis on which the best model is selected. Rather than using a single RMSEP, we subdivide the test set and calculate the RMSEP for all test set data acquired at 3 m, and SCCTs observed at 3 , 1.545, and 4.25 m.

The primary metric we use to select a model is the RMSEP for the test set spectra at 3 meters (the most typical distance at which targets will be analyzed on Mars). For each element, several models typically had a better performance than other models evaluated (lower RMSEP). For models with similar RMSEP for data obtained at 3 m, we next evaluated the RMSEP with SCCT data obtained at 1.545 and 4.25 m. All models for all elements performed worse at 4.25 m, suggesting that there may be a problem with that set of data. Although the poor performance at 4.25 m is not fully understood, we favored models that were more robust to the differences in that data set. We also calculated the RMSEP for just the SCCTs at 3 m. This was not used as the primary statistic for model selection because the calibration targets include several "extreme" compositions, but if the 3 m overall RMSEP was similar for multiple models, the model with better performance on the calibration targets was preferred. Based on these RMSEPs and other considerations such as model performance at low and high concentrations, we identified several candidate regression models for each element for more detailed evaluation.

The model selection steps described above were completed prior to landing on Mars. Once initial spectra of calibration targets and geologic targets from the surface of Mars were available, we began an additional stage of evaluation using those data. The calibration targets are useful because they have a known composition; however, they are analyzed at closer distance than the Mars target and a lower power must be used to prevent saturation. Mars geologic targets are of unknown composition but can still serve as a valuable check to ensure that the predictions are geochemically reasonable and are consistent with comparable spectra of known composition from the laboratory. Depending on the grain size of minerals in a rock, the LIBS analytical footprint may be small enough to analyze individual grains and return a pure mineral composition. Observations that appear to be pure minerals or simple mixtures of minerals are useful for evaluating model performance, because there are known geochemical constraints on mineral compositions.

In April 2021, roughly two months after landing on Mars, the initial results were used in conjunction with laboratory results to select a preferred model for each of the major elements from among the candidates identified prior to landing. After that initial selection, we continued to monitor the predicted compositions as additional targets were observed over the following months. In September 2021, we reviewed the results from Mars and in several cases switched to a different model based on our findings. We discuss this in more detail below for each individual major element.

The test set predictions of the final selected models are shown in Figure 12, the SCCT predictions on Mars are shown in Figure 13, and histograms of the compositions predicted for Mars targets through Sol 239 are shown in Figure 14.

905

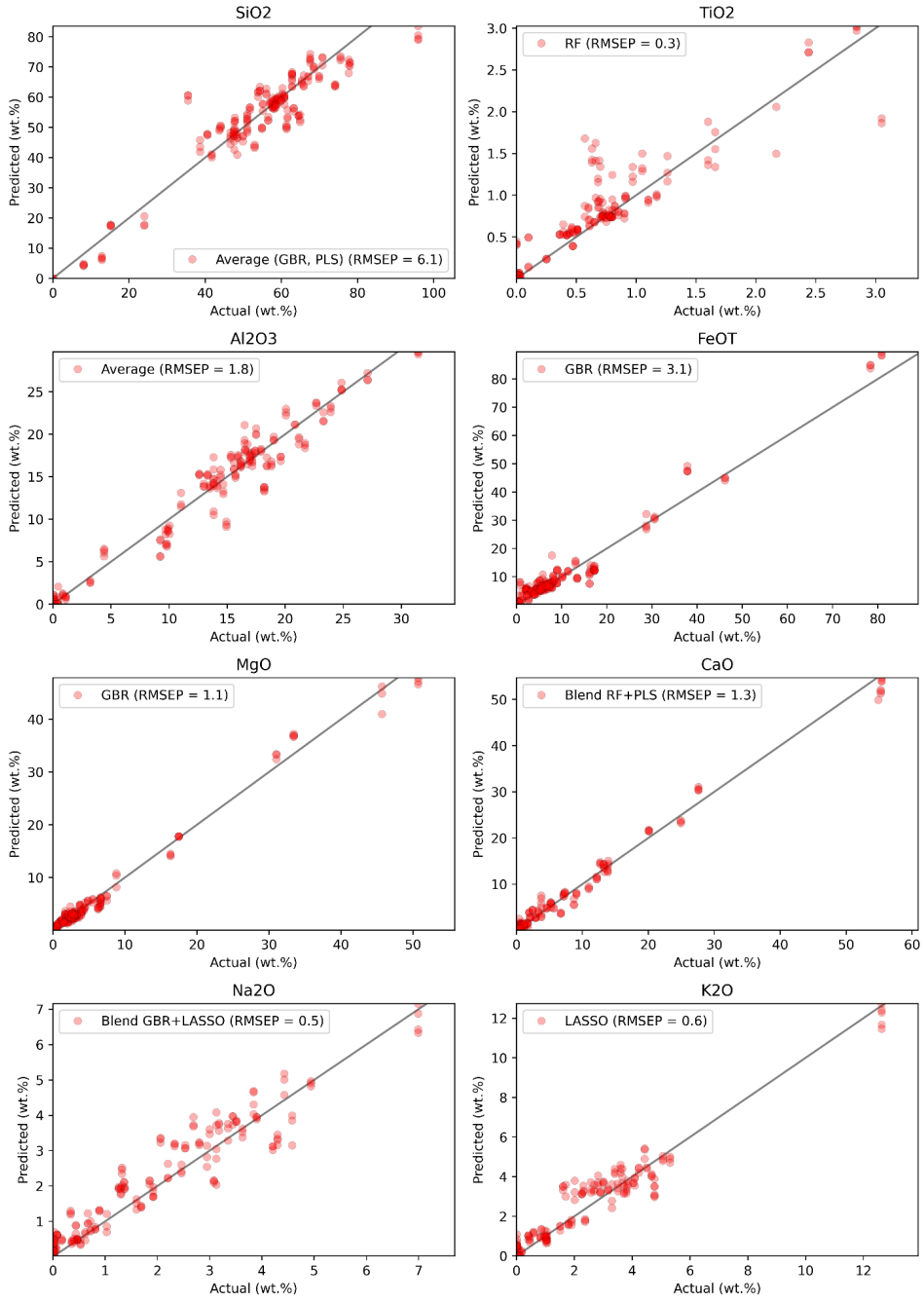

Figure 12: Test set predictions for each major element for the current selected models. Negative predictions are set to zero. Perfect predictions would fall on the diagonal (1:1) line. RMSEP indicates the overall accuracy in wt.% of the model when predicting the test set. SiO_2 results are the average of GBR and PLS predictions. Al_2O_3 results are the average of predictions using several different algorithms. CaO and Na_2O results use a blend of two

models to obtain more accurate results at both low and high concentrations (see text for details).

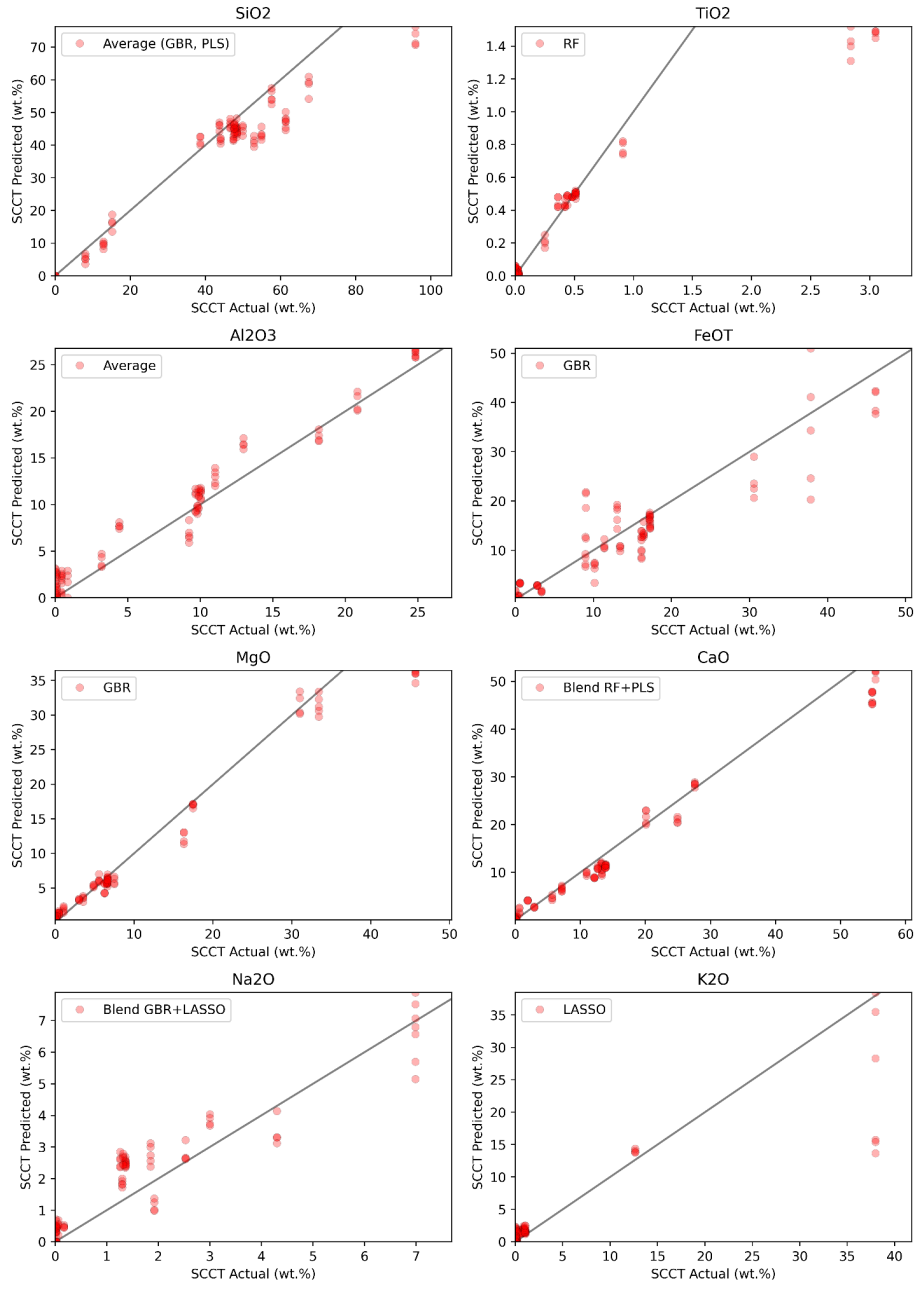

Figure 13: Prediction results for the SCCTs measured on the martian surface using the current selected models

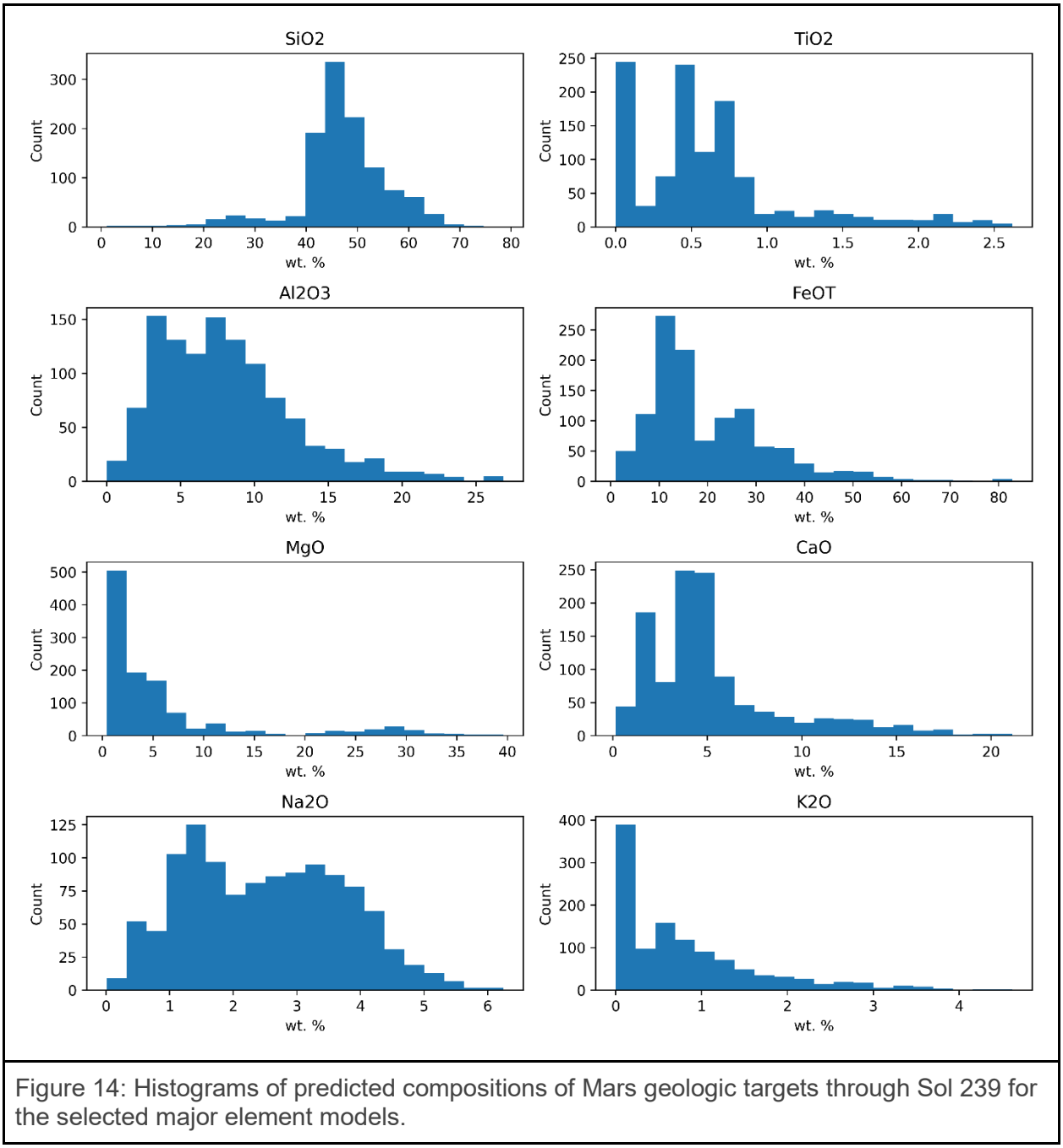

Figure 14: Histograms of predicted compositions of Mars geologic targets through Sol 239 for the selected major element models.

4.2.1. SiO_2

SiO_2 is a critical element for understanding both igneous and sedimentary geochemistry. In Gale crater, ChemCam analyzed targets with a wide range of predicted SiO_2 values from nearly 0 to >70 weight % [32,76]. Therefore, accurate predictions across a wide range of SiO_2 values are critical for SuperCam as well.

Of the models considered for SiO_2, five had lower RMSEPs at 3 m and were investigated in more detail: RF, GBR, PLS, Local Elastic Net, and a blend of SVR, Elastic Net, and PLS

submodels. The blended model performed considerably worse on the 4.25 m data than the other models and performed poorly at compositions >75 wt.%, so it was removed from consideration. PLS had the best performance on the 4.25 m data, but GBR had a lower RMSEP on the 3 m data, so an average of the GBR and PLS predictions was used to mitigate the errors of the individual models (Figure 12). Figure 15 shows the feature importance values for the GBR model and the regression coefficients for the PLS model.

The most important feature for the GBR model is the 413.04 nm spectral channel, corresponding to the Si II lines at 412.9 nm and 413.2 nm. The PLS model does not show a single dominant spectral channel. This PLS model uses standardized spectra, which results in a more even spread of influence across the full spectrum.

Figure 13 shows results from the SCCT data collected on Mars. The low compositional range is predicted accurately while the higher end tends to underpredict. The mid-range, from ~38-60 wt.%, shows similar predicted values with considerable scatter, indicating poor discrimination among these targets for SiO_2. This behavior is also observed in the other regression models considered; it is not unique to the GBR and PLS models.

Figure 14 shows a histogram of SiO_2 predictions on Mars, excluding SCCTs, through sol 239. The majority of martian targets fall between ~40 and 65 wt.%, with a small number of points exceeding 65 wt.%, and a significant number of predictions in the 0-40 wt.% range, likely indicating mixtures between silicate and non-silicate minerals such as Fe oxides. In investigation of LIBS points on possible pyroxenes, we find that the predicted SiO_2 content is 5-10 wt.% lower than that of typical martian meteorites.

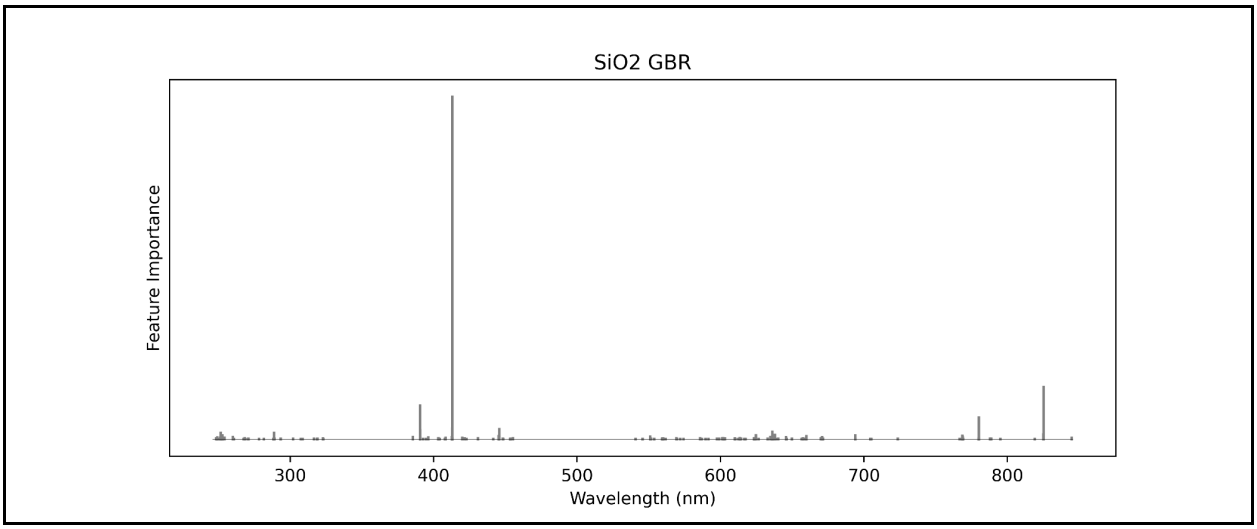

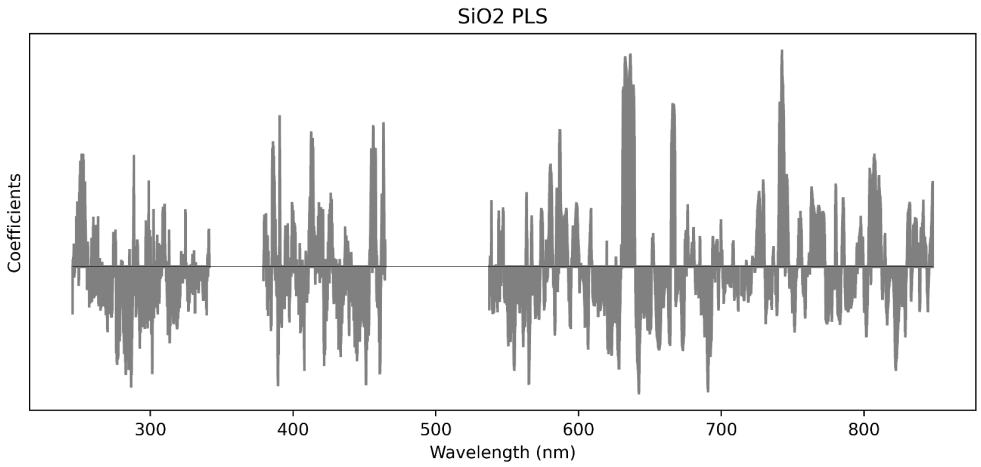

Figure 15: (top) Feature importance values for the SiO_2 GBR model. The most important feature is at 413.04 nm, corresponding to the Si II lines at 412.9 nm and 413.2 nm. (bottom) Regression coefficients for the SiO_2 PLS model. This model uses standardized spectra, so individual strong lines are less favored, and the influence on the model is more evenly spread across the spectrum.

4.2.2. TiO_2

The choice of regression model for TiO_2 was relatively straightforward: the models with the best performance at 3 m were GBR, RF, and a blend of elastic net submodels, all with an RMSEP of ~0.3 wt.%. Of these models, RF exhibited better performance at 4.25 m, and was therefore selected. Figure 12 shows the performance on the laboratory test set. The scatter in the predictions is smaller at the low end and increases toward higher concentrations. A group of samples at ~0.6 wt.% actual TiO_2 content are overpredicted and are visually notable in the plots, but most samples with compositions <1 wt.% TiO_2 are predicted accurately. Figure 16 shows the feature importance values for the RF model. This model uses a different mask than other models discussed in this paper. It was trained on spectra with the full transmission spectrometer masked out and thus relies strictly on the UV and VIO spectrometers. The most important spectral channels (Figure 16) correspond to several Ti II lines in the UV.

Figure 13 shows the TiO_2 predictions on the SCCTs on Mars. The TiO_2 model performs well on SCCTs with TiO_2 <1 wt.%, but predicts a range of 1.3 wt.% - 1.5 wt.% for LBHVO2 (actual TiO_2 wt.% of 2.84 wt.%). This target is predicted accurately in the laboratory data. The other high TiO_2 SCCT (LJSC1; actual TiO_2 of 3.05 wt.%) is underpredicted in both the laboratory and on Mars.

In martian data, several observations for which the RF model predicts compositions between 2 and 3 wt.% have LIBS spectra that suggest a far greater TiO_2 content, more similar to the laboratory spectra of ilmenite. These points highlight a limitation of the ensemble methods such as RF and GBR. Whereas methods such as LASSO or PLS may underpredict samples with

very high concentration, they are capable of some degree of extrapolation and can yield predicted compositions outside of the training set used for the model. RF and GBR, on the other hand, do not predict values outside of the range of compositions in their training set. The training set used for TiO_2 has a maximum value of 3.4 wt.%, and therefore no higher TiO_2 predictions are possible from the RF model. Two samples in the laboratory database did have higher TiO_2 concentrations but were excluded from modeling because they were too spectrally distinct. One is pure ilmenite (36 wt.% TiO_2) and one is a mixture of basalt and ilmenite (6.6 wt.% TiO_2). We experimented with a RF model that incorporated these higher TiO_2 samples in the training set, and it did yield much higher TiO_2 predictions on the Mars spectra in question, but at the expense of degraded performance on low-TiO_2 samples. It was also impossible to evaluate the accuracy of this high TiO_2 model for high-concentration (>5 wt.%) targets, since the only high-TiO_2 samples were used to train it, and the Mars sample compositions are unknown. Since most geologic targets are low in TiO_2 (<2 wt.%), we chose to continue to use the original RF model and flag spectra that predict near the upper end of the training set range as requiring special attention.

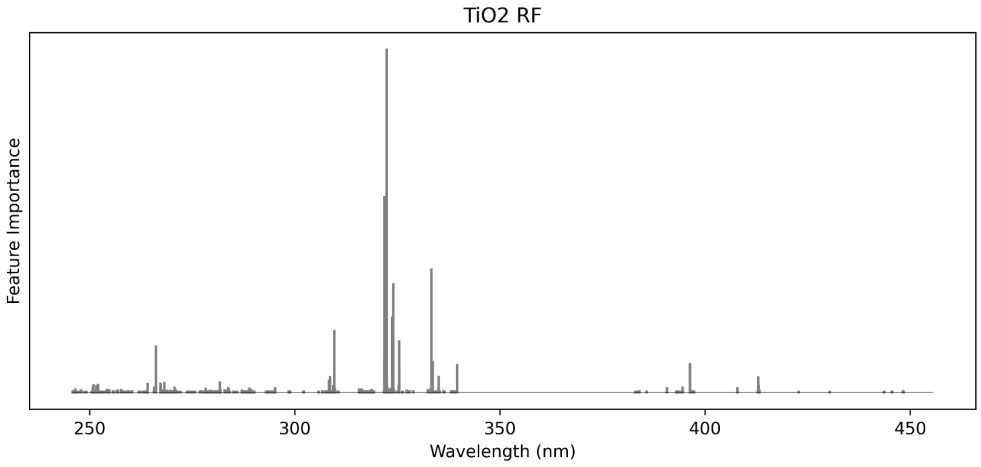

Figure 16: Feature importance values for the TiO_2 Random Forest (RF) model. The most important features in the model and their corresponding Ti lines are: 322.37 nm (Ti II at 322.38 nm), 321.83 nm (Ti II at 321.80 nm), 333.29 nm (Ti II at 332.39 nm and 333.04 nm), 323.99 nm (Ti II at 324.0 nm), and 323.72 nm (Ti II at 323.75 nm).

4.2.3. Al_2O_3

For Al_2O_3, the four models investigated in detail were Local ENet, RF, and two variants of PLS; one with peak binning and standardization and one without. Local ENet had the lowest 3 m RMSEP (1.97 wt.%), but we found that an average of the predictions from these four models resulted in a lower 3 m RMSEP than any of the individual models (1.8 wt.%), so the average was chosen as the preferred “model.” Figure 12 shows that the test set predictions perform well across the range of compositions, although moderate concentrations (10-20 wt.%) exhibit more

scatter in the predictions than either the low or high ends. Figure 17 shows the feature importance values for the RF model and the regression coefficients for the two PLS models.

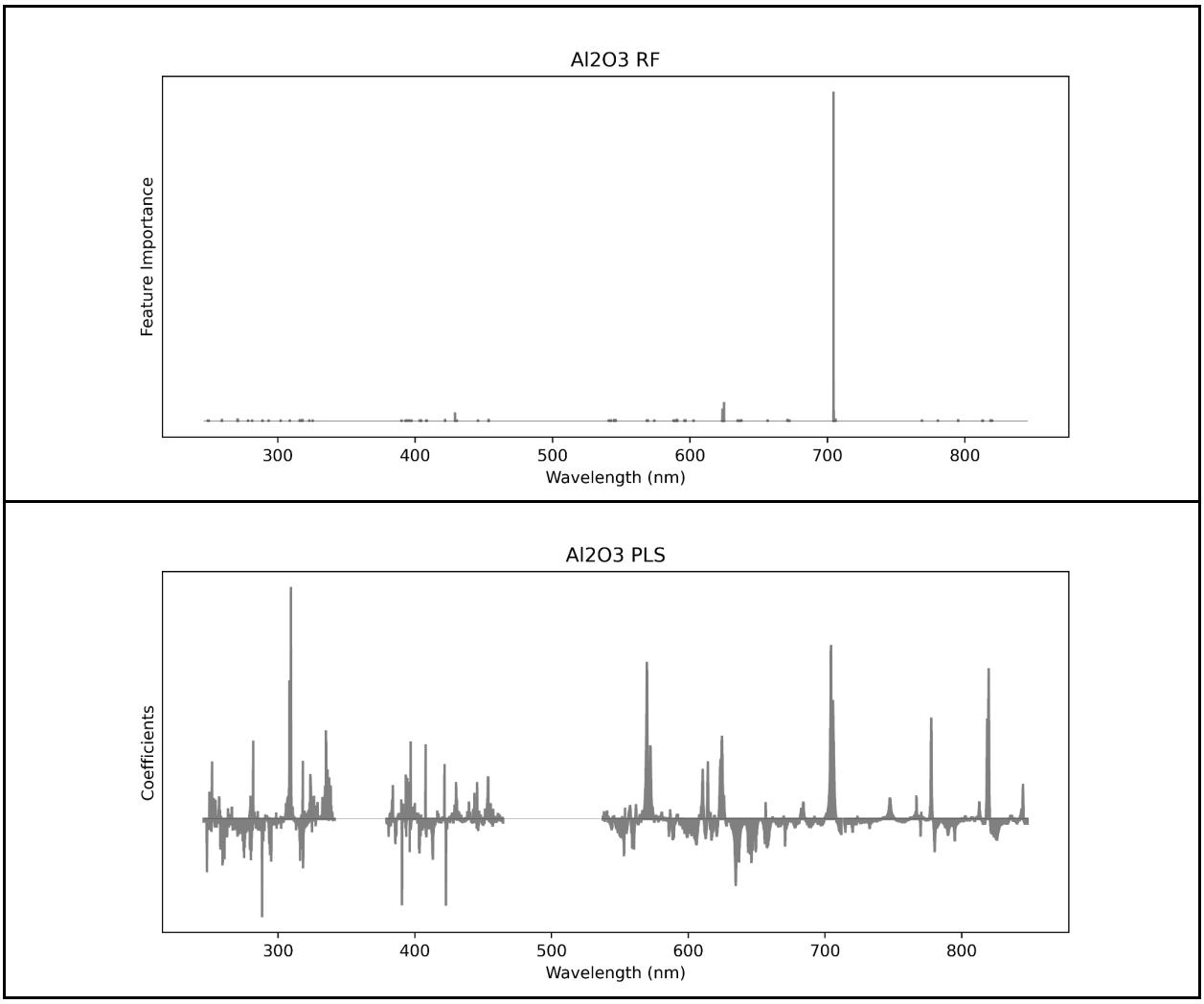

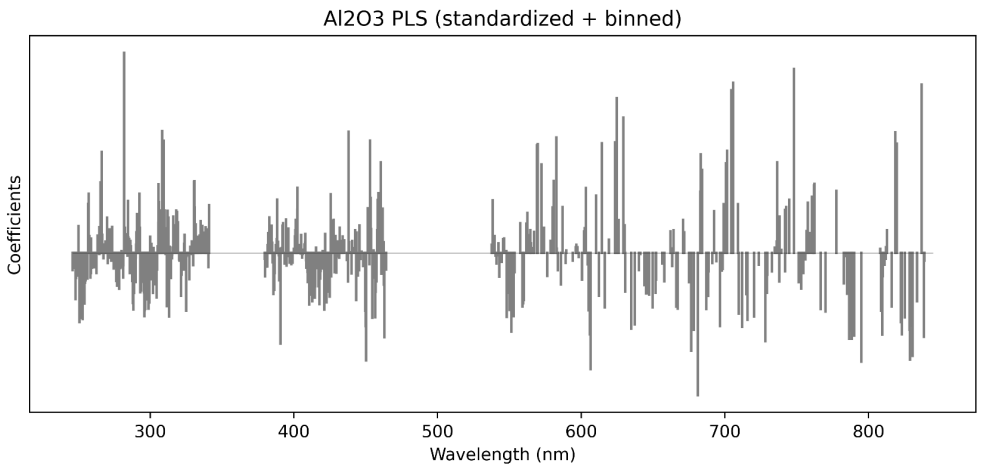

Figure 17: Feature importance values and regression coefficients for three of the four models that are averaged for the Al_2O_3 predictions. The Local ENet model does not have a fixed set of coefficients, since the local model trains on the fly based on the unknown spectrum. (top) The RF model relies almost solely on the spectral channel at 704.38 nm corresponding to the Al II line at 704.4 nm. (middle) PLS using 11 components, without peak binning or standardization applied. Strongest coefficients correspond to the following lines: Al I at 309.37 nm, Al II at 704.4 nm, Na I 568.98 nm, Na I 819.71 nm. There are notable negative coefficients at 288.24 nm (Si I), 390.67 nm (Si I at 390.66 nm), and 422.8 nm (Fe I at 422.86 nm or Ca I at 422.79 nm). (bottom) PLS using 13 components on peak binned, standardized spectra. The five strongest coefficients are at 281.75 nm (Al II at 281.7 nm), 748.05 nm (O I at 748.24 nm), 705.89 nm (Al II at 705.86 nm), 837.01 nm (Al II at 836.58 nm), and 704.38 nm (Al II at 704.4 nm), although standardization results in numerous other strong coefficients.

The Al_2O_3 model performs well on the Mars SCCTs, with most predictions close to the true composition (Figure 13). Of particular interest are the SCCTs PMIAN (andesine; 24.84 wt.% Al_2O_3), LJSC1 (JSC Mars-1 simulant; 20.83 wt.% Al_2O_3), and PMIOR (orthoclase; 18.18 wt.% Al_2O_3). These targets are accurately predicted by the Al_2O_3 model, indicating that the model performs well on feldspars. Figure 14 shows the distribution of Al_2O_3 predictions on Mars. Most targets have <10 wt.% Al_2O_3, but a significant “tail” of predictions extends up to ~27 wt.%.

Based on Mars surface data gathered so far at Jezero crater, restricted to samples with concentrations of SiO_2 (>35%), Al_2O_3 (>10%), Na_2O (<20%) and CaO (<30%) compatible with feldspars, no target has sufficient K_2O to be clearly identified as K-rich feldspar. However, there are many candidates with compositions similar to those calculated for the Andesine and JSC Mars-1 SCCTs (Figure 18). Plagioclases are the dominant feldspars detected by CheMin at Gale crater [77], with the exception of the Windjana location which contained K-rich feldspar [78].

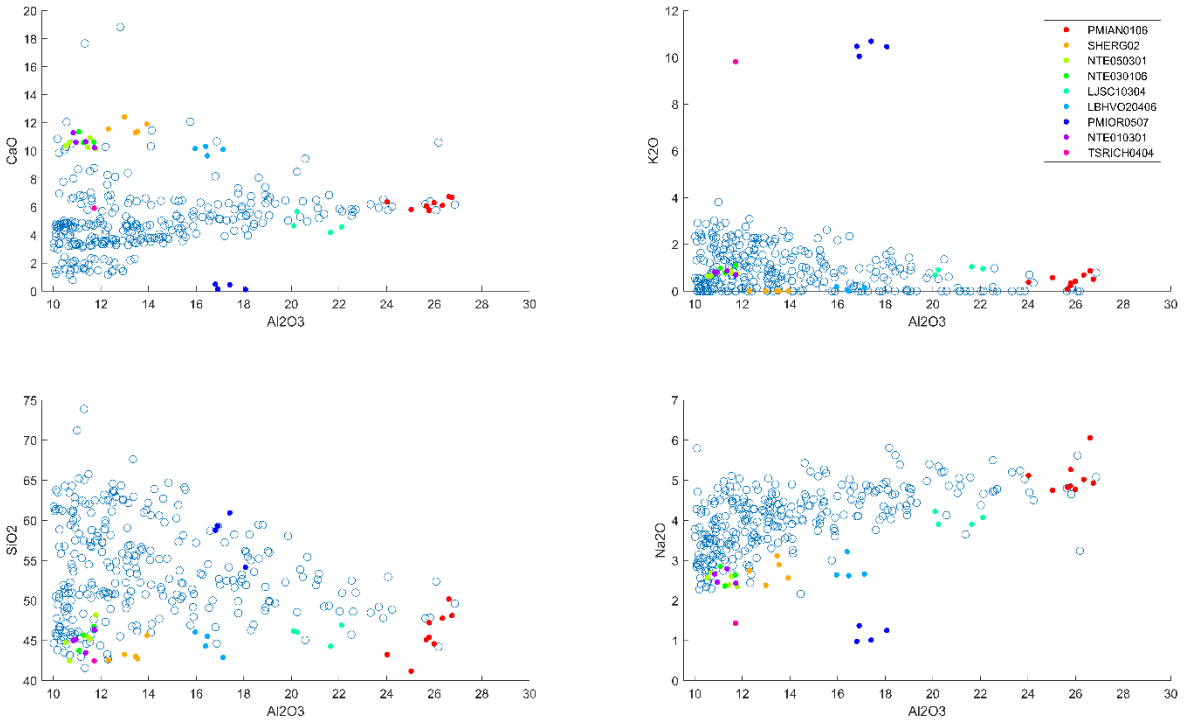

Figure 18: Calculated concentrations of Al_2O_3 vs different elements of interest for feldspars. hollow circles represent Mars surface measurements, while the colored dots correspond to Mars SCCT measurements.

We observe some evidence that spectra from targets with high TiO_2 concentrations may result in overestimates of Al_2O_3. This is likely due to the large number of emission lines present in the spectra of high-TiO_2 samples, which overlap with positive loadings in the Al_2O_3 models. For example, consider the surface target Ha'íí'ą́ągo (Haa_ii_aah[1]) Point 1 on this target has a very high concentration of TiO_2 (predicted as 2.6 wt.% but likely significantly higher) and the Al_2O_3 model predicts a concentration of 17.4 wt.%. The spectra from this point have weak Al lines, but numerous Ti lines. Table 4 compares the predictions from each Al_2O_3 model for this target. The RF model predicts a much lower concentration (4.8 wt.% Al_2O_3), which is more similar to the composition of other points on the target. The features with higher weight in RF calculations are mainly located at 704 nm (Figure 17). Ti has many emission lines, particularly in the UV range, so the reliance on a longer wavelength Al line may make the RF model less sensitive to high Ti. The overall performance of the averaged models is more accurate than that of RF alone, so we

[1] Targets early in the mission were given names in the Navajo language because the rover landed in an area of the landing site named after Canyon de Chelly National Monument, which is within the Navajo Nation. For situations where special characters cannot be used, such as in commands sent to the rover, a "plain text" version of the name that approximates the pronunciation is used. We list both versions.

still use the average as the default prediction. However, this illustrates that caution should be used in cases with high Ti and that the RF model may be a viable alternative in such cases.

Table 4: TiO_2 and Al_2O_3 predictions in wt.% for target Ha'íí'ą́ągo (Haa_ii_aah)

		Al_2O_3 Predictions				
Point	TiO_2 Predictions	PLS (binned + standardized)	Local ENet	PLS	RF	Average
1	**2.6**	**21.4**	**26.0**	**17.4**	**4.8**	**17.4**
2	0.8	8.0	9.6	7.3	5.1	7.5
3	1.6	3.5	7.6	5.6	5.1	5.5
4	0.1	5.2	7.8	3.8	5.3	5.6
5	0.5	12.2	13.5	11.6	15.0	13.1
6	0.8	10.0	10.2	8.9	5.6	8.7
7	0.7	6.5	9.4	7.1	12.8	9.0
8	0.9	8.0	10.5	8.1	13.1	9.9
9	0.9	6.9	10.8	7.5	5.9	7.8
10	0.3	14.0	11.1	11.5	12.5	12.3

4.2.4. FeO_T

Selection of an FeO_T model was subject to considerable discussion. Of the models evaluated, GBR and RF had the best performance at 3 m and at 4.25 m. The RF model was initially selected as the preferred model, based on its performance at both high and low extremes of composition in the test set. Preliminary Mars results seemed to support the selection of RF as the preferred model. In particular, point 1 on the target Dį́į' (Dii_scam) and point 6 on the target Tsé łibá (Tselhbahih) both exhibited high FeO_T concentrations. Comparison with laboratory spectra indicated that the RF model was likely closer to the true composition, while GBR was likely overestimating FeO_T in Fe-rich targets.

However, additional results from Mars have led us to revisit the decision to use the RF model rather than the GBR model. In particular, in studying the results from candidate high-Ca pyroxenes, the stoichiometry using RF indicated that the FeO_T content may be underestimated by ~4 wt.%, and resulted in compositions that fell outside those permitted for pyroxenes. Substituting the GBR FeO_T predictions for the RF predictions resulted in more realistic stoichiometry overall, but also increased the overall scatter in the results. The effect of switching from RF to GBR was evaluated on several other groups of targets as well. For points with MgO content >20 wt.%, switching to GBR yields stoichiometries more consistent with olivines. For

targets where the sum of the major elements is >110 wt.%, switching from RF to GBR brings the totals closer to 100 wt.%. For these reasons, we chose to switch to GBR as the preferred model for FeO_T. The results for the laboratory 3 m test set are shown in Figure 12, and the Mars SCCT results are shown in Figure 13. Figure 19 shows the feature importance values for the GBR model and indicates that the model results are primarily driven by Fe I and II lines in the UV and VIO spectrometers.

The distribution of the GBR FeO_T predictions for all Mars geologic targets to date (Figure 14) peaks at ~12-15 wt.%, with a long tail toward higher concentrations. In general, we find that the estimated FeO_T content of rocks and soils analyzed by *Perseverance* is lower than other sites on Mars. This is best illustrated by examining the results from the first LIBS shots on geologic targets, which are dominated by dust. Since martian dust is highly mobile and globally distributed, it is assumed to be homogeneous across different landing sites. Results from ChemCam at Gale crater give a dust FeO_T content of ~20 wt.% [79], similar to the estimated FeO_T content for dust rich soils (17 wt.%) and the average martian crust (18 wt.%;. By contrast, all of the regression models considered for SuperCam tend to underpredict FeO_T abundance in the dust, giving results closer to 12 wt.%.

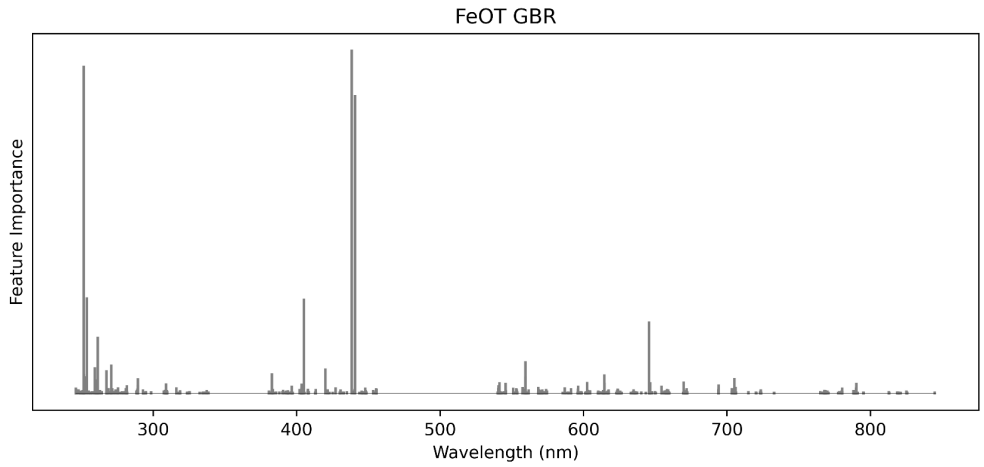

Figure 19: Feature importance values for the FeO_T GBR model. The most important features are at 438.46 nm (Fe I at 438.48 nm), 440.61 nm (Fe I at 440.6 nm), and 251.59 nm (Fe II at 251.51 nm).

4.2.5. MgO

The four MgO models that were evaluated in detail were RF, GBR, ENet, and PLS, and they all performed well for the 3 m test set data. GBR had the lowest RMSEP (1.1 wt.%), closely followed by RF (1.22 wt.%). Both models also inherently avoid negative predictions, while the ENet and PLS models had some negative predictions for low-MgO targets. RF showed a slight tendency to overpredict MgO for high concentration samples, so GBR was selected as the preferred model.

Figure 12 shows GBR results for the 3 m test set. The GBR model relies heavily on two spectral channels corresponding to the Mg II emission line at 448.238 nm (Figure 20).

The GBR model performs well on most of the SCCTs in Mars data, as shown in Figure 13. The model underpredicts the diopside SCCT (PMIDN) both on Mars and in the laboratory data set (actual MgO content of 16.32 wt.%) but performs well on the ankerite SCCT (LANKE; actual MgO content of 17.46 wt.%). The most notable deviation is that GBR predicts values of 34.6-36.4 wt.% for the Serpentine/Talc SCCT (TSERP), when the actual MgO content is 45.68 wt.%. This underprediction is not observed in the laboratory results.

In the LIBS data collected on Mars, the GBR model appears to be performing relatively well, predicting a wide range of composition from depleted to significantly Mg-rich rocks (Figure 14). There is no clear correlation with any other of the major elements except some clusters of points that may correspond to major mineral classes (e.g. olivines, pyroxenes). There is no noticeable relation between MgO prediction and distance to the target.

One possible area of concern is that the points that are highest in MgO also tend to be the points with major element totals exceeding 100 wt.%. Some of these cases approach 130 wt.%, which is well beyond what can be explained by the RMSEPs for each element and suggests a systematic bias in one or more of the most abundant elements in the target (MgO, SiO_2, or FeO_T). A number of these points have LIBS spectra and estimated compositions consistent with olivine based on comparison with SCCT PMIFA on Mars, and the presence of olivine has been confirmed by SuperCam Raman spectroscopy. The stoichiometric ratios of FeO_T, MgO, and SiO_2 in the olivine-bearing points are consistent with olivine, but MgO is not particularly high for olivine (e.g. compared to PMIFA). The high totals may come from the contribution of other elements rather than an overestimate of MgO. Note that predictions for the analysis of SCCT PMIFA on Mars do not show a high total.

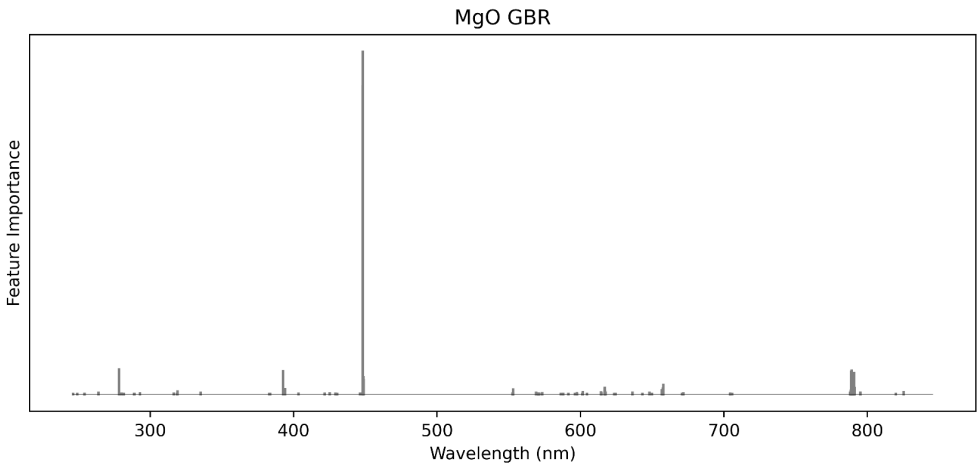

Figure 20: Feature importance values for the MgO Gradient Boosting Regression (GBR) model. The most important features are at 448.21 and 448.24 nm (Mg II at 448.238 nm).

4.2.6. CaO

The five best models for CaO calibration were RF, Elastic Net, SVR, and two instances of PLS (with and without peak binning). The RF model yielded the lowest 3 m RMSEP (1.51 wt.%) and was the only algorithm that produced universally positive predictions; all other tested models predicted negative CaO values for some low-CaO samples. Consequently, the RF model was selected as the preferred model for CaO.

However, martian surface measurements indicated that the RF model was not performing as well as expected. The CaO predictions showed a bimodal distribution, with most predictions falling in one of two clusters centered around 6 and 20 wt.%, respectively. This bimodal distribution is not reflected in the Ca emission line intensities in normalized spectra, which are more evenly distributed. Likewise, the bimodal distribution predicted by the RF model is not reflected in any of the other candidate models, suggesting that the observed data structure is intrinsic to the RF algorithm and is not representative of the true distribution of CaO at Jezero crater.

In response to this behavior on martian data, we evaluated the average of the two best models: RF and PLS without peak binning. This reduced but did not eliminate the bimodal behavior, and introduced numerous negative predictions at low concentrations due to the PLS model. However, the PLS model alone showed better results for higher concentrations and lacked the spurious bimodal behavior. This led us to use a blended submodel approach, with the RF model used as both the “reference” model and the “low” model, and the PLS model used for cases in which the reference model predicts high concentrations of CaO. The range over which the two models are blended was optimized based on the training set, resulting in the following values: For RF predictions <4.33 wt.%, the results are used without any modification. For RF predictions between 4.33 wt.% and 8.9 wt.% the RF and PLS predictions are combined in a weighted sum, with the weights determined by where in the range the initial RF prediction falls. For RF predictions >8.9 wt.% the PLS prediction is used instead. The result has a RMSEP on the 3 m test set of 1.3 wt.% (Figure 12), and performs well on the Mars SCCT data (Figure 13). The regression coefficients for the PLS model (Figure 21) show a strong positive weight on several Ca emission lines, and the RF model feature importance highlights the Ca I 442.67 nm line.

The histogram of CaO predictions for Mars geologic targets (Figure 14) shows that the group of predictions at ~20 wt.% is no longer evident, though there is still some degree of bimodality in the lower CaO results, with groups of predictions at ~2 wt.% and at 4-5 wt.%. Preliminary attempts to correct for this behavior suggest that models based on just the UV and VIO spectrometers produce a smoother CaO distribution, and work is ongoing to evaluate these results.

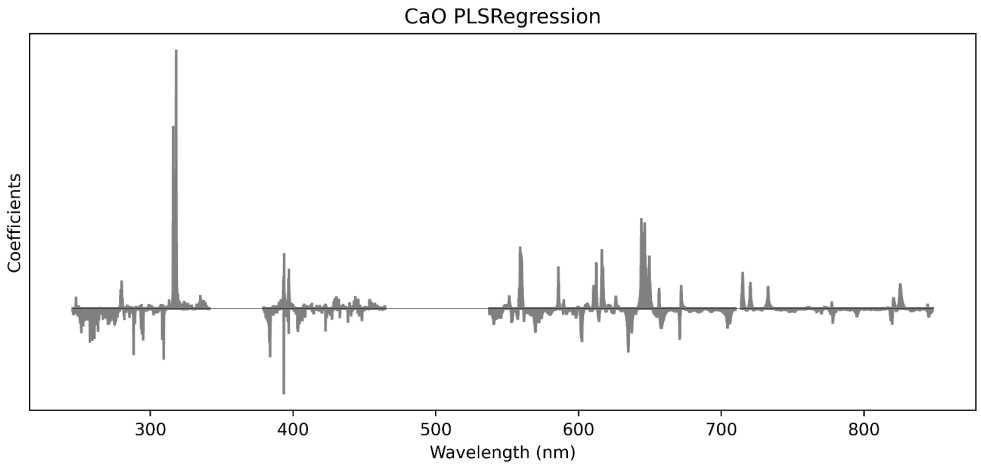

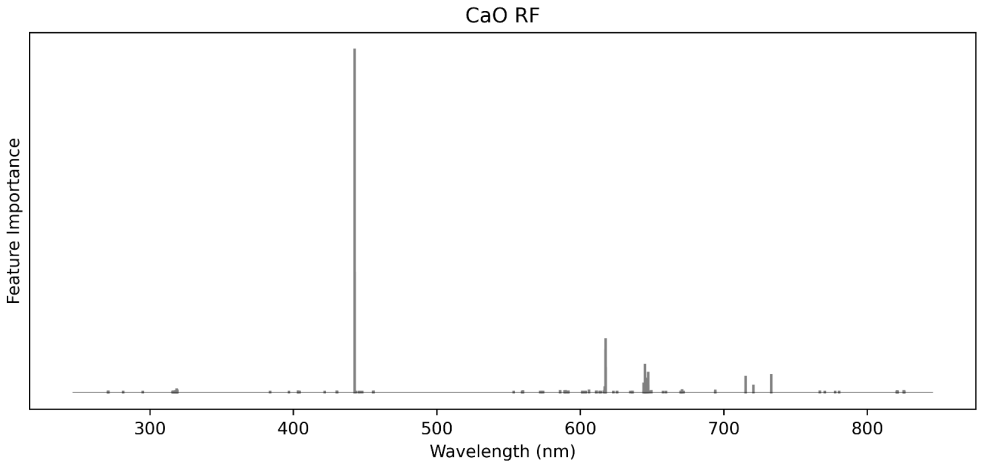

Figure 21: Regression coefficients and feature importance values for the two models used in CaO predictions. (top) The PLS model is used for higher concentrations. This model has its strongest positive coefficients at 317.9 nm - 318.2 nm and 315.9 nm - 316.1 nm, corresponding to the Ca II lines at 318.05 nm and 315.98 nm, respectively. (bottom) The Random Forest (RF) model is used as the reference model and for lower concentrations. The most important feature for this model is at 442.71 nm (Ca I at 442.67 nm).

4.2.7. Na_2O

For Na_2O, four models had a similarly low 3 m test set RMSEP (between 0.5 and 0.6 wt.%): LASSO, GBR, and two different Blend models, referred to as “Blend A” and “Blend B.” To choose among these models, we compared their predictions on initial Mars data. The Blend A and Blend B model had similar results, with their highest predictions reaching ~4.5 wt. %. In contrast, GBR and LASSO had predictions >5.5 wt. %. By comparing the LIBS spectra of the points with the highest Na_2O predictions with laboratory spectra, we determined that the Na_2O content seemed to be underestimated with the Blend A and B models, so those models were eliminated from consideration.

We next investigated the differences between the GBR and LASSO. We initially picked GBR; however, we found that some Mars data were trending towards plagioclase composition in terms of each major element, except for Na_2O, which appeared to be underestimated. We found that LASSO predicted higher values (up to 7.5 wt.%) compared to GBR (up to 6 wt.%). This behavior was confirmed by evaluating the GBR and LASSO predictions of the andesine SCCT: LASSO predicts the Na_2O in andesine more accurately than GBR. The disadvantage of the LASSO model was that it gave a large number of negative values on observations with low Na_2O.

To combine the better performance of the GBR model at low concentrations with the better performance of LASSO at high concentrations, we developed a blended model that uses GBR as the "reference" model and at the low end (when GBR predicts Na_2O <3.335 wt. %), a weighted sum of GBR and LASSO between 3.335 wt.% and 5.458 wt.%, and LASSO only when GBR predicts Na_2O > 5.458 wt. %. These blending ranges were optimized on the training set. See [65] for details of the submodel blending process.

The performance of this blended model on the 3 m test set is shown in Figure 12 (RMSEP of 0.5 wt.%), and the Mars SCCT performance is shown in Figure 13. The feature importance values and regression coefficients for the GBR and LASSO models (Figure 22) show that the GBR model relies heavily on the Na I lines at 819.704 nm and 819.708 nm. The LASSO model uses several Na emission lines, but also uses negative coefficients corresponding to Ca. Figure 14 shows the distribution of Na_2O predictions for Mars geologic targets.

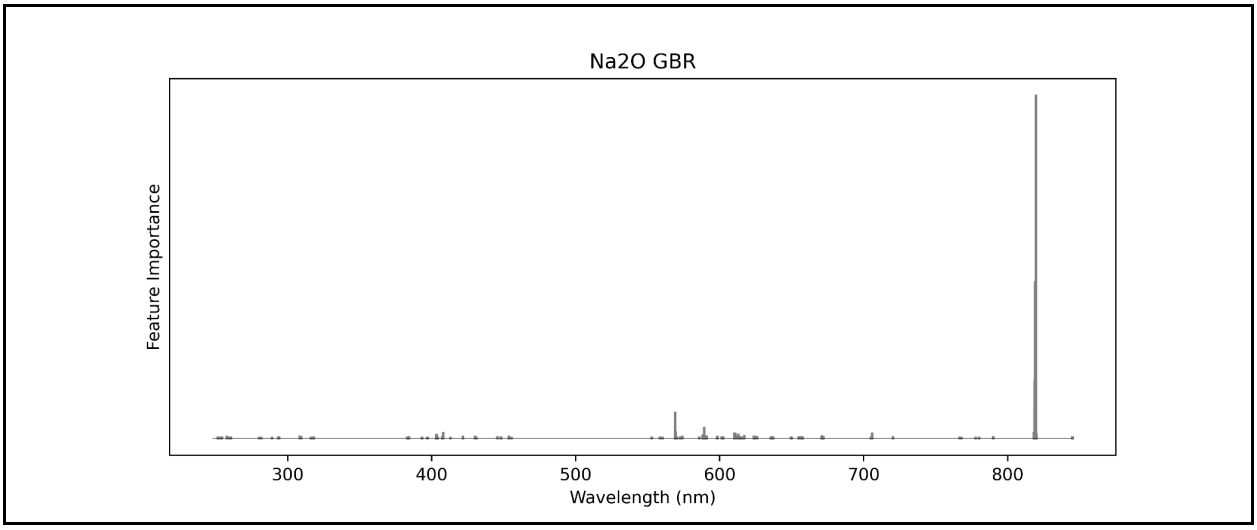

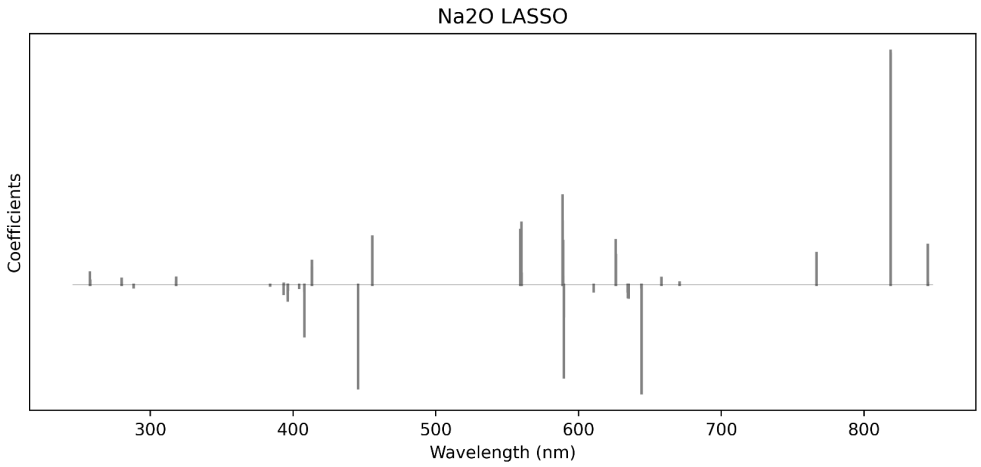

Figure 22: Feature importance and model coefficients for the two models used in the Na_2O predictions. (top) The GBR model is used as the reference model and for predictions of low concentrations. The most important features for this model occur at 819.79 nm (Na I lines at 819.704 nm and 819.708 nm), and 819.09 nm (Na I at 818.55 nm). (bottom) The LASSO model has several important coefficients, both positive and negative: 818.66 nm and 818.74 nm (Na I at 818.55 nm), 644.18 nm (Ca I at 644.09 nm), 445.61 nm (Ca I at 445.60 nm and 445.71 nm), and several coefficients, both positive and negative, related to the strong Na I doublet at 589.158 nm and 589.756 nm.

4.2.8. K_2O

As shown in Figure 2, most samples in the LIBS data set have K_2O concentrations <6 wt.%. There are several samples between ~6 wt.% and ~10 wt.%, and two very high K_2O SCCTs: TSRICH (37.99 wt.%; a mixture of BHVO-2 basalt and K-sulfate) and PMIOR (12.63 wt.%; orthoclase). As a result of this distribution, it is challenging to train models that predict K_2O accurately both in the 0 to 5 wt.% range and for higher potassium contents. The TSRICH composition is so extreme that it is unrealistic to expect any model using our data set to predict it reliably.

Five models were considered in detail for the K_2O calibration, and they showed different behaviors at low and high potassium concentrations. In general, the models presented a tradeoff between the variability of predictions and performance at high K_2O contents. The PLS, ENet, and LASSO models have broader variations for a given K_2O content, which results in negative predictions for some low K_2O samples but perform better at high concentrations. The SVR and Local ENet models are less noisy but tend to severely underestimate high K_2O compositions.

We found that averaging the predictions of these five models resulted in slightly improved performance for concentrations <10 wt.% compared to the LASSO model (low-concentration 3 m RMSEP of 0.59 wt.% for averaging vs 0.64 wt.% for LASSO). Therefore the averaged result was

selected as the initial preferred “model”. This averaging still resulted in negative values for some low-K_2O targets. In these cases, we set the potassium content to 0 wt.%.

In our evaluation of the Mars results, we found the averaged results underpredicted both high K_2O SCCTs (PMIOR 12.63 wt.% and TSRICH 37.99 wt.%) while the LASSO model performed better on both targets. Although the LASSO predictions of TSRICH were still significantly low and highly variable, this is expected given the limitations of our data set. The Mars results were consistent with the laboratory results, but upon further discussion of the LASSO vs averaging results, we decided that the slight improvement of the averaged models over LASSO at low concentrations was not sufficient to sacrifice the better performance of LASSO at the high concentrations and we decided to switch to using the LASSO model alone as the preferred model. The 3 m test data set performance is shown in Figure 12. The RMSEP is 0.6, and the PMIOR target at 12.6 wt.% is predicted well. The test set predictions for targets with actual compositions between ~2-4 wt.% are grouped at ~3.5 wt.%. However, this behavior is not observed in the distribution of predictions from Mars (Figure 14). Mars SCCT results (Figure 13) include the extremely high K_2O TSRICH target, showing the predictions for this target vary widely from approximately correct to significant underprediction. Figure 23 shows the regression coefficients for the LASSO model, which relies heavily on the K II emission line at 438.94 nm, rather than the stronger K I lines at 766.7 nm and 770.1 nm.

In the Mars results, the potassium content is mostly low, with steadily decreasing frequency toward higher concentrations (Figure 14). On the low end of this range, we observe that the model sometimes predicts negative values (which we set to 0 wt.% K_2O) for points that have potassium lines in their spectra, especially for points with high Mg, Ca or Fe content. This is not unique to LASSO; it is observed for all of the K_2O models considered. LIBS is highly sensitive to K_2O, particularly at the two strong K I emission lines mentioned above, so it is not surprising that at low K_2O contents, models with a RMSEP of ~1 wt.% may predict negative or zero K_2O contents when weak K_2O lines are still present. Blended submodels trained on an expanded training set could help to mitigate this behavior while also improving high K_2O predictions.

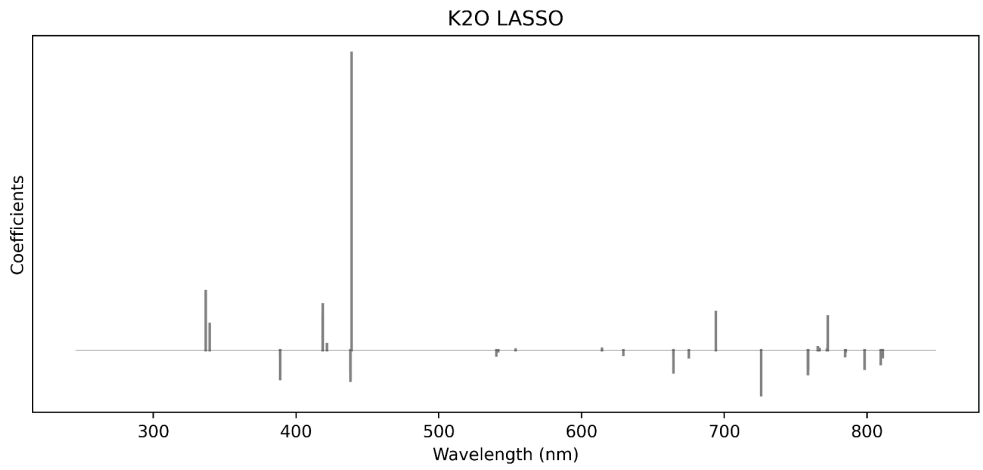

Figure 23: Regression coefficients for the K_2O LASSO model. The strongest coefficient is at

438.9 nm, which corresponds to K II at 438.94 nm.

5. Discussion

5.1. Accuracy

The 3 m test set performance (RMSEP) provides an estimate of the accuracy of each regression model (Table 5), but in most cases the prediction accuracy varies with predicted composition and depends on the distribution of samples in the calibration data set. To provide the most representative estimate of the accuracy of each prediction, we calculate the RMSEP as a function of predicted concentration ("local RMSEP") similar to that used for ChemCam [38].

Table 5: Summary of 3 m test set RMSEPs and selected models

Element	RMSEP wt.%	Model
SiO_2	6.1	Average (GBR, PLS)
TiO_2	0.3	RF
Al_2O_3	1.8	Average
FeO_T	3.1	GBR
MgO	1.1	GBR
CaO	1.3	Blend RF+PLS
Na_2O	0.5	Blend GBR+LASSO
K_2O	0.6	LASSO

Local RMSEP is calculated for each element by first creating an evenly spaced array of simulated predicted values. For each simulated prediction, we calculate the RMSEP of the 60 nearest test set predictions. As described in the Setup section, each target in the database was analyzed three times, so 60 test set predictions represent the nearest 20 targets. In cases where the distribution of test set compositions is sparse, a range of simulated predicted compositions may have the same nearest 60 test set predictions and therefore identical local RMSEPs. This is an artifact of the test set, and the "true" local RMSEP is assumed to vary smoothly. We handle these cases by removing duplicate values from the array of local RMSEPs. The local RMSEP values with duplicates removed are shown in black in Figure 24. After removal, we re-interpolate the RMSEP values, effectively creating a linear ramp in places where there was previously a "stair step." To avoid neighboring predictions with significantly different RMSEPs, we smooth the RMSEP vs prediction curve such that it captures large-scale variations but removes small jumps in value.

It is also necessary to extrapolate the local RMSEP values beyond the range of the test set. This is preferable to reporting no RMSEP at all for high predictions or reporting a "flat" RMSEP which would almost certainly underestimate the true uncertainty. We prefer to instead make an educated guess at the trend of RMSEP with predicted composition. With no test set data to

compare with, extrapolated RMSEP values are speculative and should be used with caution. For most major elements, we calculate the slope of the extrapolated line based on a linear fit to the RMSEP values after removal of duplicates but prior to the re-interpolation. Since most elements have a general trend correlating RMSEP with predicted wt.%, this results in a line with a positive slope. Al_2O_3 is an exception: its RMSEP vs prediction curve rises and then drops back down, so a line fit to all of the RMSEP points has a nearly flat slope. We want our extrapolated local RMSEPs to be conservative, with the uncertainty increasing with the degree of extrapolation. So, for Al_2O_3 we instead fit the extrapolation line to only the RMSEP points from the minimum value at ~16 wt.% and above.

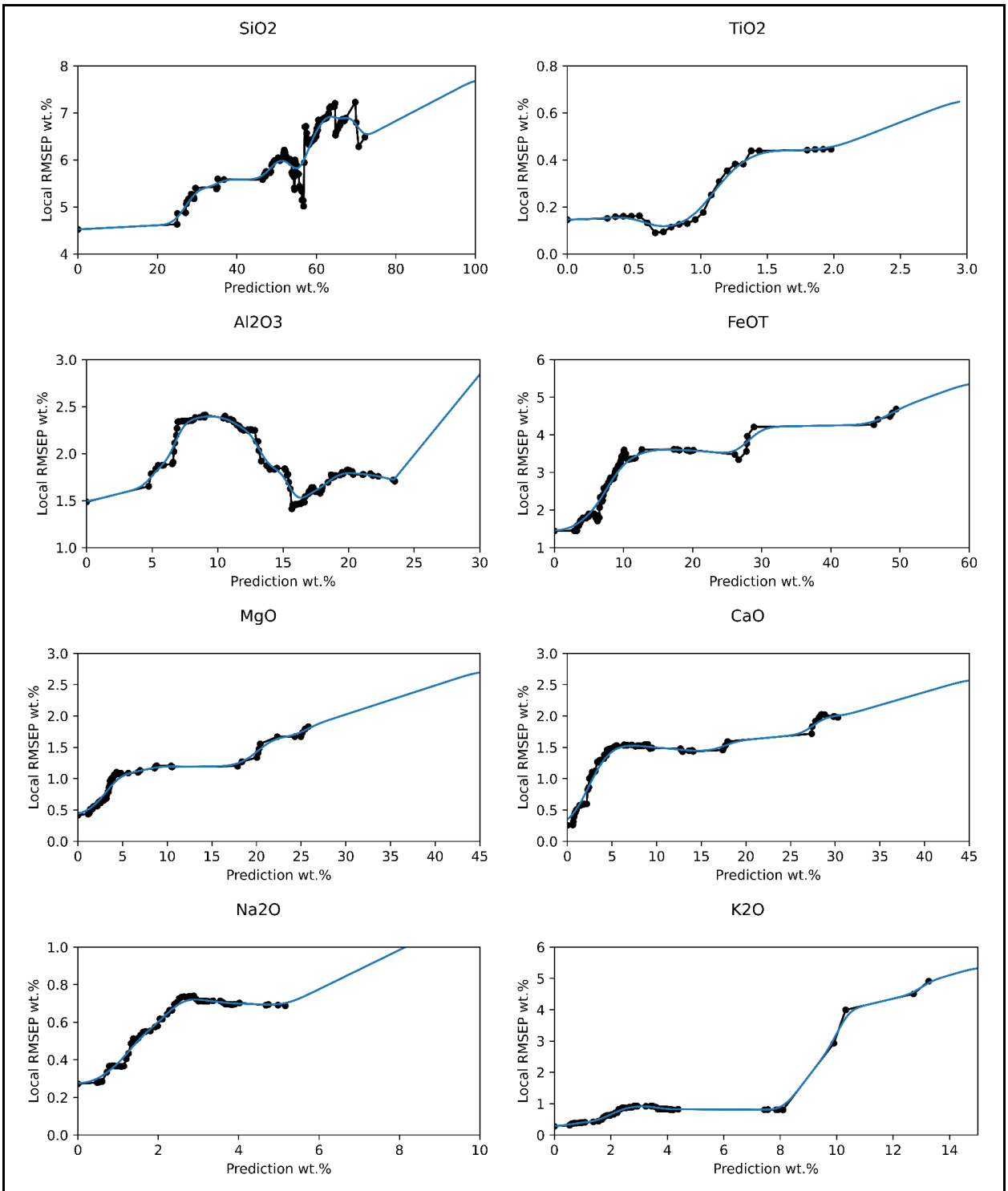

Figure 24: Local RMSEP vs prediction wt.% for each of the major elements. Black points are the unsmoothed values calculated using the nearest 60 test set predictions. Blue curves show the result of smoothing and extrapolating as described in the text.

5.2. Precision

According to the definition in ISO 5725-1:1994 [80], the accuracy of a model—how close its prediction is to the true value—is a combination of its trueness and precision Trueness is how far the average prediction is from the true composition, while precision indicates the distribution of individual predictions around that average prediction value. RMSEP is a measure of the accuracy of our quantification, which is useful to understand when we compare derived abundances with stoichiometric mineral compositions or with abundances derived from other instruments (e.g., PIXL, ChemCam, APXS). Precision is important in determining whether groups of targets observed by the same instrument can be distinguished from one another[81]. For example, to understand if the rover has entered a new geological formation by testing for a change in the distribution of chemical abundances [e.g., 15,81,82].

We assess SuperCam precision in two ways. The first is to calculate the standard deviation of predictions across several locations on each target in the laboratory test set, assuming that these targets are homogeneous and that the predictions will be normally distributed. Then we take an average of the standard deviations across all targets. Effectively, this provides an estimate of the average spread around the typical predicted value expected in each oxide. Most standards were observed in three locations on the same target. Although standard deviations are usually computed from a larger number of samples, we apply it here on only three values for each standard. We argue that this statistic should be robust because we are averaging the standard deviations of ~60-70 standards, depending on the element. We find that the standard deviations are not correlated with concentration, so the mean standard deviation is taken in all cases (Table 6).

A similar exercise can be conducted using the results from the SCCTs on Mars. This benefits from a greater number of observations per target, which makes the standard deviation estimate more robust. It also benefits from the fact that the measurements are made with the flight instrument on Mars rather than the laboratory instrument, making the precision estimates more relevant to measurements on Mars. In the Mars SCCT results, the standard deviations for high-MgO and high-Na_2O targets were somewhat higher than those for lower concentrations. In these cases we report the overall average precision and the precision with higher concentration targets excluded (the value in parentheses) in Table 6. The results for K_2O exclude the very high K_2O TSRICH target.

Several factors affect the standard deviations from replicate measurements on standards. We suspect that some standards that are outliers in terms of standard deviations have larger grain sizes and/or more diverse compositions in individual grains despite efforts during sample preparation to homogenize the sample powders. Although the diameter of the laser beam is ~250 μm [2], the center of the beam can produce a large fraction of the ablation and emission, so grain sizes must ideally be much smaller than 50 μm. Other factors that will contribute to variations in reproducibility on surface targets include variations in focus, laser energy, and distance to the sample. On Mars, these factors will cause more day-to-day and sample-to-sample variations than are quantified in the test set standard deviations.

Table 6: Estimated precision for each of the major elements in wt.%. Numbers in parentheses exclude some higher concentration samples.

	SiO_2	TiO_2	Al_2O_3	FeO_T	MgO	CaO	Na_2O	K_2O
3 m Test Set (Laboratory)	0.8	0.06	0.4	0.5	0.2	0.2	0.1	0.1
SCCTs (Mars)	1.6	0.02	0.7	1.3	0.5 (0.3)	0.5	0.3 (0.2)	0.3

By comparing the values in Table 6 to the RMSEPs in Table 5 and Figure 12, we find that SuperCam LIBS quantification is more precise than it is accurate, similar to the results from ChemCam (e.g., [84]). Thus, although we strive to provide accurate stoichiometry, the greater precision of the results combined with the ability to make frequent observations over the course of the rover traverse, makes LIBS particularly useful for distinguishing trends in composition, both within a single heterogeneous target, and across multiple targets.

SuperCam's estimated precision is comparable to that of ChemCam. Two measures of ChemCam's precision are given from repeated observations of its onboard calibration targets [84] and of homogeneous, fine-grained bedrock [e.g.,81]. Many of the rocks encountered to date in Jezero crater are heterogeneous at the scale of SuperCam LIBS points, so we do not yet have enough observations of fine-grained rocks to provide an estimate of precision using data from Mars surface targets.

5.3. Environmental Factors

As discussed above, numerous factors can cause changes in LIBS spectra, resulting in changes in the quantitative results. These include shifts in wavelength calibration, variations with distance and focus quality, and sensitivity to anomalous features in the spectra or faulty continuum removal. Some factors can be assessed now, while assessing others would require additional data collection either in the laboratory or on Mars.

One effect that can be readily assessed with available data is the influence of shifts in wavelength. Although we do not observe significant shifts in wavelength calibration in the Mars data, slight shifts are unavoidable, and larger changes may occur due to changing seasonal temperatures, observations conducted at unusual times of day, and changes in the instrument itself over time. We trained our regression models on spectra that had been artificially shifted by ±1 or 2 pixels to improve robustness to any shift that may occur. The peak binning preprocessing used by some models also increases robustness to any shifts. Figure 25 shows the 3 m test set RMSEP as a function of wavelength shift in pixels, with horizontal black bars providing a reference value of 1.2 times the RMSEP without any shift. Within ±1 pixel of wavelength shift, all models show little change in RMSEP.

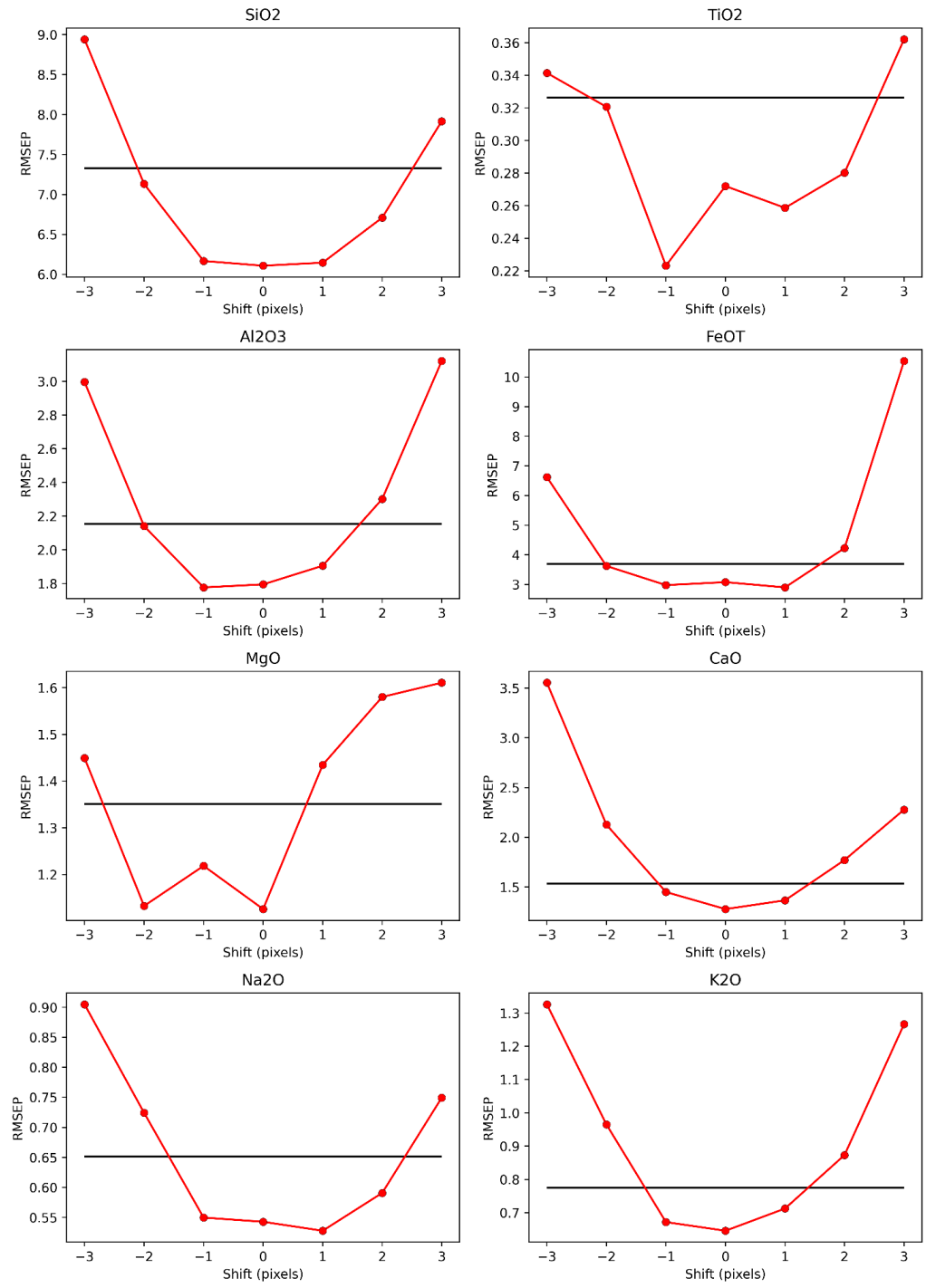

Figure 25: Test set RMSEP for each major element as a function of pixel shift. Horizontal black lines indicate a 20% increase in RMSEP relative to the value at 3 m. Wavelength shifts observed in Mars data correspond to less than 1 pixel of shift, which causes little variation in RMSEP for all elements.

Distance effects have been observed in data from ChemCam. Multiple studies [85–87] observed that predicted abundances of several elements (Al, Na, K, and to some extent Si) increased as a function of distance. For SuperCam, our models have the advantage of being based primarily on data acquired at 3 m, whereas the ChemCam models were trained on data acquired at 1.5 m [38]. The SuperCam models were also selected based in part on robustness to distance trends. However, additional Mars data at varying distances may still reveal a distance effect, particularly since SuperCam has shown greater ability than ChemCam to observe targets at long distances. SuperCam LIBS operates at least to 8.75 m compared to ChemCam's longest observation of ~7.2 m on bedrock. Both instruments area able to achieve a LIBS spark at even longer distances on iron meteorites (due to iron's excellent absorption of the laser), which are encountered occasionally on the surface of Mars. However, pure metal targets have significantly different matrix effects than typical geologic targets composed of oxides and must be handled separately. As additional data are collected on Mars, especially on fine-grained, uniform geologic units, it will be possible to better assess distance effects and develop methods to mitigate it.

We do not have laboratory data suitable to assess variations in results due to changing focusSuch data could be collected on Mars, either as a dedicated experiment or over the course of the mission, as occasional observations with poor focus are inadvertently acquired. The effects of poor focus are similar to the effects of distance in that the laser energy per unit area on the target is decreased. Thus, it may be that a distance correction (if needed) also can help to mitigate the effects of poor focus.

In Mars data, we have observed a bump in the baseline of processed data that covers several nm around 290 nm in the UV spectrometer that was not present in the cleanroom data. The origin of this feature is not well understood and still under investigation, but it may be related to the SiO_2 content of the target. We are currently testing a correction to the continuum removal algorithm parameters for the UV spectrometer to remove the bump. Alternatively, or in addition, it may be possible to remove the anomalous bump using calibration transfer methods, as described below.

5.4. Future Work

Although the current models selected for the major elements are acceptable, they could be improved. In addition, developing methods by which new spectra could be evaluated prior to quantification would ensure that they are similar enough to the training data set to give accurate results. The sections discussing Spectral Variability and Outlier Removal above suggest possible approaches to evaluating and identifying outliers that could be applied to the Mars data. In addition, it may be beneficial to develop tests to verify the presence of emission lines from an element prior to predicting it.

5.4.1. Uncertainty Quantification

Although our calculation of Local RMSEP seeks to provide an estimate of the uncertainty of a prediction as a function of composition, it is not able to account for the possibility that the "true" uncertainty in the predicted composition may be differ even for the same predicted composition.

For example, two samples may have the same SiO_2 content, but one may have significantly more FeO_T and as a result have an increased uncertainty in the predictability of SiO2. Under our current scheme, the local RMSEP at a certain predicted SiO_2 content is constant, regardless of any other factors. Additionally, while the extrapolated Local RMSEP values are a better solution for predictions outside the training set than simply providing a constant RMSEP, it should be possible to achieve a more statistically rigorous estimate of uncertainties in these cases. One approach is to use Bayesian regression methods, which are inherently based on probability distributions. Rather than returning a single value, they return a distribution of predictions for each unknown spectrum. Statistical measures, such as the mean and standard deviation of that distribution, can be used to describe the model's "best" prediction and its associated uncertainty. Preliminary work on quantifying LIBS using gaussian process variational autoencoders [88] is promising, and has additional benefits such as the ability to estimate the spectrum corresponding to a given composition, with uncertainties on the estimated spectrum.

5.4.2. Minor and trace elements

Minor and trace elements are important to quantify because they provide distinctive tracers among largely similar rock targets, related to their primary petrogenesis (i.e. magmatism) and information about past alteration. Such elements typically present only a few detectable emission lines, which are relatively weak compared to the lines from major elements. Both univariate and multivariate methods have been used to quantify minor and trace elements with LIBS.

For the ChemCam instrument, several methods were investigated for quantifying trace elements. Ollila et al. [89] developed univariate and multivariate (PLS) models for the quantification of Li, Rb, Sr, and Ba. For Li, they found that the univariate model was more accurate than the PLS models. However, for Rb, Sr, and Ba, the univariate and PLS models gave similar results. [36] revised the quantification of these elements, using univariate models and the updated ChemCam database with more than 400 samples [38]. The updated quantification showed improvement for Li and Ba and similar results for Rb and Sr, although a direct comparison of RMSE is difficult because the range of compositions in the models was different.

Mn is an important element to quantify because it provides information about redox and pH of the ancient martian environment. It was first quantified for ChemCam using a univariate approach [31] based on a database of ~60 samples. Then, using the expanded database from [38] with additional Mn-bearing samples, [90] developed an improved quantification for Mn, based on blended multivariate submodels.

Several other minor/trace elements are quantified with ChemCam: Cl, H, S, P, Ni, F, Zn [e.g. 48,51,90–92]. Quantification of minor and trace elements to which LIBS is relatively sensitive (Li, Rb, Sr, Ba, and Mn) is likely to be more straightforward, while elements with weaker spectral lines (Cl, S, H, P, Ni, F) will likely be more challenging.

5.4.3. Alternative Normalization

Prior to significant efforts to revise the major element calibration or develop new calibrations for trace and minor elements, it would be prudent to review the preprocessing steps applied to the spectra before quantification, such as normalization. Although normalization helps to correct for fluctuations intrinsic to the LIBS process, and to mitigate distance, focus, and signal quality effects, the normalization scheme itself can introduce artifacts. Our normalization is currently applied after the continuum has been removed. Because of this, the sum of the signal in each spectrometer by which the spectrum is divided, is highly dependent upon the composition of the target [25]. For example, consider two targets with identical Ca content, one with a very high Fe content and one with very low Fe. Fe has numerous emission lines, particularly in the UV spectrometer. Thus, the high-Fe sample will be divided by a larger number (the sum of the emission lines) effectively resulting in “smaller” Ca lines compared to the other target, despite having identical Ca content.

Finding an alternative method of normalization that can avoid these issues may be possible One possibility is to divide the spectrum in each spectrometer by the total of the continuum in that spectrometer, which is far less influenced by the composition of the target than the total of the emission lines. However, part of the initial motivation for removing the continuum before normalization was to mitigate distance effects. Normalizing by the continuum may reduce normalization artifacts related to composition at the expense of stronger artifacts due to distance, necessitating a separate distance correction.

5.4.4. Calibration Transfer

Although the application of the instrument response function corrects for the most significant differences between spectra collected in the laboratory and those collected on Mars, there are still differences. The origin of these differences is not fully understood, but they represent a common scenario in chemometrics, where a calibration was developed using data from a specific instrument in certain conditions and then is implemented on another instrument or the same instrument in different conditions. The process of correcting for such differences is referred to as “calibration transfer,” and various methods are available for performing this task. In general, calibration transfer relies on a set of spectra collected by both instruments to derive a transformation that can be applied to one or both sets of spectra to minimize differences and enable accurate intercomparison. For ChemCam, a simple calibration transfer approach based on the average ratio between rover calibration target spectra from Mars and those in the laboratory was used by Clegg et al. [38]. Similarly, for SuperCam the SCCTs provide the suite of common spectra on Earth and Mars.

We have begun investigating calibration transfer corrections that may improve the performance of our quantifications. In Figure 26, we show the results of applying the piecewise direct standardization (PDS) calibration transfer method [94] to the lab SCCT data. We find the transformed data are spectrally ‘closer’ to the Mars data by examining the distance between the principal components of Mars and laboratory spectra before and after calibration transfer.

Additional work is needed to assess the influence of calibration transfer on quantification and to understand how the differences in laser power between SCCT and Mars surface target observations affect the correction.

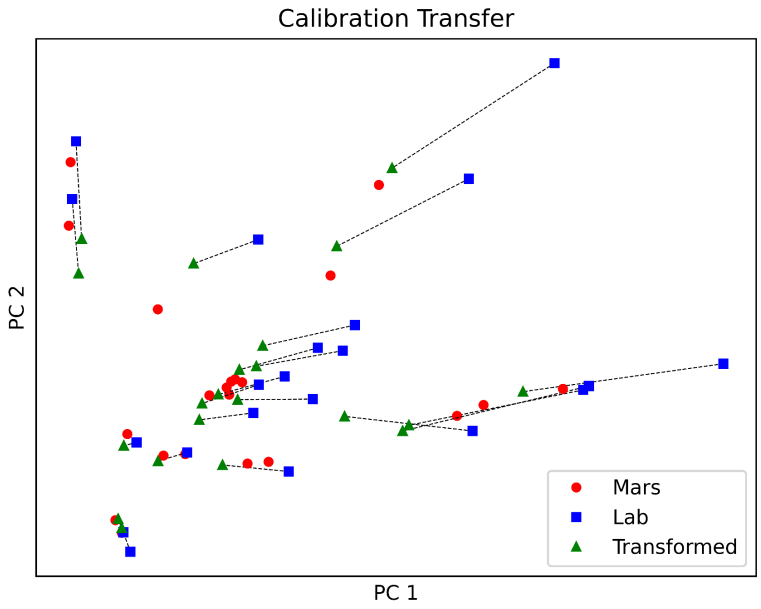

Figure 26: PCA scores plot comparing average Mars spectra for each SCCT (red circles) with the corresponding average spectra from the laboratory (blue squares). Laboratory spectra with Piecewise Direct Standardization (PDS) calibration transfer applied are shown as green triangles. Dashed lines connect the untransformed and transformed lab data points. In general, calibration transfer brings the laboratory spectra closer to the corresponding Mars spectra.

6. Conclusion

This paper represents a summary of the current status of SuperCam LIBS quantification efforts. By using a suite of 1198 laboratory spectra of 334 diverse standards, we have developed multivariate regression models for the quantification of the major elements SiO_2, TiO_2, Al_2O_3, FeO_T, MgO, CaO, Na_2O, and K_2O. Initial model selection was based primarily on test set RMSEPs and early results from Mars. With additional data from Mars, we were able to identify issues with the initial calibration which were not apparent in laboratory data alone and adjust the selected models accordingly to eliminate or reduce the issues identified. Although many areas of potential improvement remain, the SuperCam major element calibration is more mature than the ChemCam calibration was at a similar point in the mission. As additional data are collected

on Mars and in the laboratory, it will be possible to continue to improve SuperCam's quantitative LIBS capabilities, which play a fundamental role in the *Perseverance* rover's science mission.

Acknowledgements

This project was supported in the USA by the NASA Mars Exploration Program and in France by CNES, CNRS, and local universities. Support in Spain was provided by the Spanish Science Ministry. SuperCam benefitted from LANL laboratory-directed research and development funding which provided early prototypes of the new technologies incorporated in the SuperCam BU. JF acknowledges the support from the Carlsberg Foundation. Any use of trade, firm, or product names is for descriptive purposes only and does not imply endorsement by the U.S. Government.

References

[1] K.A. Farley, K.H. Williford, K.M. Stack, R. Bhartia, A. Chen, M. de la Torre, K. Hand, Y. Goreva, C.D.K. Herd, R. Hueso, Y. Liu, J.N. Maki, G. Martinez, R.C. Moeller, A. Nelessen, C.E. Newman, D. Nunes, A. Ponce, N. Spanovich, P.A. Willis, L.W. Beegle, J.F. Bell, A.J. Brown, S.-E. Hamran, J.A. Hurowitz, S. Maurice, D.A. Paige, J.A. Rodriguez-Manfredi, M. Schulte, R.C. Wiens, Mars 2020 Mission Overview, Space Sci. Rev. 216 (2020) 142. https://doi.org/10.1007/s11214-020-00762-y.

[2] S. Maurice, R.C. Wiens, P. Bernardi, P. Caïs, S. Robinson, T. Nelson, O. Gasnault, J.-M. Reess, M. Deleuze, F. Rull, J.-A. Manrique, S. Abbaki, R.B. Anderson, Y. André, S.M. Angel, G. Arana, T. Battault, P. Beck, K. Benzerara, S. Bernard, J.-P. Berthias, O. Beyssac, M. Bonafous, B. Bousquet, M. Boutillier, A. Cadu, K. Castro, F. Chapron, B. Chide, K. Clark, E. Clavé, S. Clegg, E. Cloutis, C. Collin, E.C. Cordoba, A. Cousin, J.-C. Dameury, W. D'Anna, Y. Daydou, A. Debus, L. Deflores, E. Dehouck, D. Delapp, G. De Los Santos, C. Donny, A. Doressoundiram, G. Dromart, B. Dubois, A. Dufour, M. Dupieux, M. Egan, J. Ervin, C. Fabre, A. Fau, W. Fischer, O. Forni, T. Fouchet, J. Frydenvang, S. Gauffre, M. Gauthier, V. Gharakanian, O. Gilard, I. Gontijo, R. Gonzalez, D. Granena, J. Grotzinger, R. Hassen-Khodja, M. Heim, Y. Hello, G. Hervet, O. Humeau, X. Jacob, S. Jacquinod, J.R. Johnson, D. Kouach, G. Lacombe, N. Lanza, L. Lapauw, J. Laserna, J. Lasue, L. Le Deit, S. Le Mouélic, E. Le Comte, Q.-M. Lee, C. Legett, R. Leveille, E. Lewin, C. Leyrat, G. Lopez-Reyes, R. Lorenz, B. Lucero, J.M. Madariaga, S. Madsen, M. Madsen, N. Mangold, F. Manni, J.-F. Mariscal, J. Martinez-Frias, K. Mathieu, R. Mathon, K.P. McCabe, T. McConnochie, S.M. McLennan, J. Mekki, N. Melikechi, P.-Y. Meslin, Y. Micheau, Y. Michel, J.M. Michel, D. Mimoun, A. Misra, G. Montagnac, C. Montaron, F. Montmessin, J. Moros, V. Mousset, Y. Morizet, N. Murdoch, R.T. Newell, H. Newsom, N. Nguyen Tuong, A.M. Ollila, G. Orttner, L. Oudda, L. Pares, J. Parisot, Y. Parot, R. Pérez, D. Pheav, L. Picot, P. Pilleri, C. Pilorget, P. Pinet, G. Pont, F. Poulet, C. Quantin-Nataf, B. Quertier, D. Rambaud, W. Rapin, P. Romano, L. Roucayrol, C. Royer, M. Ruellan, B.F. Sandoval, V. Sautter, M.J. Schoppers, S. Schröder, H.-C. Seran, S.K. Sharma, P. Sobron, M. Sodki, A. Sournac, V. Sridhar, D. Standarovsky, S. Storms, N. Striebig, M. Tatat, M. Toplis, I. Torre-Fdez, N. Toulemont, C. Velasco, M. Veneranda, D. Venhaus, C. Virmontois, M. Viso, P. Willis, K.W. Wong, The SuperCam Instrument Suite on the Mars 2020 Rover: Science Objectives and Mast-Unit Description, Space Sci. Rev. 217 (2021) 47. https://doi.org/10.1007/s11214-021-00807-w.

[3] R.C. Wiens, S. Maurice, S.H. Robinson, A.E. Nelson, P. Cais, P. Bernardi, R.T. Newell, S. Clegg, S.K. Sharma, S. Storms, J. Deming, D. Beckman, A.M. Ollila, O. Gasnault, R.B. Anderson, Y. André, S. Michael Angel, G. Arana, E. Auden, P. Beck, J. Becker, K. Benzerara, S. Bernard, O. Beyssac, L. Borges, B. Bousquet, K. Boyd, M. Caffrey, J. Carlson, K. Castro, J. Celis, B. Chide, K. Clark, E. Cloutis, E.C. Cordoba, A. Cousin, M. Dale, L. Deflores, D. Delapp, M. Deleuze, M. Dirmyer, C. Donny, G. Dromart, M. George Duran, M. Egan, J. Ervin, C. Fabre, A. Fau, W. Fischer, O. Forni, T. Fouchet, R. Fresquez, J. Frydenvang, D. Gasway, I. Gontijo, J. Grotzinger, X. Jacob, S. Jacquinod, J.R. Johnson, R.A. Klisiewicz, J. Lake, N. Lanza, J. Laserna, J. Lasue, S. Le Mouélic, C. Legett, R. Leveille, E. Lewin, G. Lopez-Reyes, R. Lorenz, E. Lorigny, S.P. Love, B. Lucero, J.M. Madariaga, M. Madsen, S. Madsen, N. Mangold, J.A. Manrique, J.P. Martinez, J. Martinez-Frias, K.P. McCabe, T.H. McConnochie, J.M. McGlown, S.M. McLennan, N. Melikechi, P.-Y. Meslin, J.M. Michel, D. Mimoun, A. Misra, G. Montagnac, F. Montmessin, V. Mousset, N. Murdoch, H. Newsom, L.A. Ott, Z.R. Ousnamer, L. Pares, Y. Parot, R. Pawluczyk, C. Glen Peterson, P. Pilleri, P. Pinet, G. Pont, F. Poulet, C. Provost, B. Quertier, H. Quinn, W. Rapin, J.-M. Reess, A.H. Regan, A.L. Reyes-Newell, P.J. Romano, C. Royer, F. Rull, B. Sandoval, J.H. Sarrao, V. Sautter, M.J. Schoppers, S. Schröder, D. Seitz, T. Shepherd, P. Sobron, B. Dubois, V. Sridhar, M.J. Toplis, I. Torre-Fdez, I.A. Trettel, M. Underwood, A. Valdez, J. Valdez, D. Venhaus, P. Willis, The SuperCam Instrument Suite on the NASA Mars 2020 Rover: Body Unit and Combined System Tests, Space Sci. Rev. 217 (2021) 4. https://doi.org/10.1007/s11214-020-00777-5.

[4] W. Xu, X. Liu, Z. Yan, L. Li, Z. Zhang, Y. Kuang, H. Jiang, H. Yu, F. Yang, C. Liu, T. Wang, C. Li, Y. Jin, J. Shen, B. Wang, W. Wan, J. Chen, S. Ni, Y. Ruan, R. Xu, C. Zhang, Z. Yuan, X. Wan, Y. Yang, Z. Li, Y. Shen, D. Liu, B. Wang, R. Yuan, T. Bao, R. Shu, The MarSCoDe Instrument Suite on the Mars Rover of China's Tianwen-1 Mission, Space Sci. Rev. 217 (2021) 64. https://doi.org/10.1007/s11214-021-00836-5.

[5] S. Maurice, R.C. Wiens, M. Saccoccio, B. Barraclough, O. Gasnault, O. Forni, N. Mangold, D. Baratoux, S. Bender, G. Berger, J. Bernardin, M. Berthé, N. Bridges, D. Blaney, M. Bouyé, P. Caïs, B. Clark, S. Clegg, A. Cousin, D. Cremers, A. Cros, L. DeFlores, C. Derycke, B. Dingler, G. Dromart, B. Dubois, M. Dupieux, E. Durand, L. d'Uston, C. Fabre, B. Faure, A. Gaboriaud, T. Gharsa, K. Herkenhoff, E. Kan, L. Kirkland, D. Kouach, J.-L. Lacour, Y. Langevin, J. Lasue, S. Mouélic, M. Lescure, E. Lewin, D. Limonadi, G. Manhès, P. Mauchien, C. McKay, P.-Y. Meslin, Y. Michel, E. Miller, H.E. Newsom, G. Orttner, A. Paillet, L. Parès, Y. Parot, R. Pérez, P. Pinet, F. Poitrasson, B. Quertier, B. Sallé, C. Sotin, V. Sautter, H. Séran, J.J. Simmonds, J.-B. Sirven, R. Stiglich, N. Striebig, J.-J. Thocaven, M.J. Toplis, D. Vaniman, The ChemCam Instrument Suite on the Mars Science Laboratory (MSL) Rover: Science Objectives and Mast Unit Description, Space Sci. Rev. 170 (2012) 95–166. https://doi.org/10.1007/s11214-012-9912-2.

[6] R.C. Wiens, S. Maurice, B. Barraclough, M. Saccoccio, W.C. Barkley, J.F. Bell, S. Bender, J. Bernardin, D. Blaney, J. Blank, M. Bouyé, N. Bridges, N. Bultman, P. Caïs, R.C. Clanton, B. Clark, S. Clegg, A. Cousin, D. Cremers, A. Cros, L. DeFlores, D. Delapp, R. Dingler, C. D'Uston, M. Darby Dyar, T. Elliott, D. Enemark, C. Fabre, M. Flores, O. Forni, O. Gasnault, T. Hale, C. Hays, K. Herkenhoff, E. Kan, L. Kirkland, D. Kouach, D. Landis, Y. Langevin, N. Lanza, F. LaRocca, J. Lasue, J. Latino, D. Limonadi, C. Lindensmith, C. Little, N. Mangold, G. Manhes, P. Mauchien, C. McKay, E. Miller, J. Mooney, R.V. Morris, L. Morrison, T. Nelson, H. Newsom, A. Ollila, M. Ott, L. Pares, R. Perez, F. Poitrasson, C. Provost, J.W. Reiter, T. Roberts, F. Romero, V. Sautter, S. Salazar, J.J. Simmonds, R. Stiglich, S. Storms, N. Striebig, J.-J. Thocaven, T. Trujillo, M. Ulibarri, D. Vaniman, N. Warner, R. Waterbury, R. Whitaker, J. Witt, B. Wong-Swanson, The ChemCam Instrument Suite on the Mars Science Laboratory (MSL) Rover: Body Unit and Combined System Tests, Space Sci. Rev. 170 (2012) 167–227. https://doi.org/10.1007/s11214-012-9902-4.

[7] M. Czerny, A.F. Turner, Über den Astigmatismus bei Spiegelspektrometern, Z. Für Phys. 61 (1930) 792–797. https://doi.org/10.1007/BF01340206.
[8] J.A. Manrique, G. Lopez-Reyes, A. Cousin, F. Rull, S. Maurice, R.C. Wiens, M.B. Madsen, J.M. Madariaga, O. Gasnault, J. Aramendia, G. Arana, P. Beck, S. Bernard, P. Bernardi, M.H. Bernt, A. Berrocal, O. Beyssac, P. Caïs, C. Castro, K. Castro, S.M. Clegg, E. Cloutis, G. Dromart, C. Drouet, B. Dubois, D. Escribano, C. Fabre, A. Fernandez, O. Forni, V. Garcia-Baonza, I. Gontijo, J. Johnson, J. Laserna, J. Lasue, S. Madsen, E. Mateo-Marti, J. Medina, P.-Y. Meslin, G. Montagnac, A. Moral, J. Moros, A.M. Ollila, C. Ortega, O. Prieto-Ballesteros, J.M. Reess, S. Robinson, J. Rodriguez, J. Saiz, J.A. Sanz-Arranz, I. Sard, V. Sautter, P. Sobron, M. Toplis, M. Veneranda, SuperCam Calibration Targets: Design and Development, Space Sci. Rev. 216 (2020) 138. https://doi.org/10.1007/s11214-020-00764-w.
[9] A. Cousin, V. Sautter, C. Fabre, G. Dromart, G. Montagnac, C. Drouet, P.Y. Meslin, O. Gasnault, O. Beyssac, S. Bernard, E. Cloutis, O. Forni, P. Beck, T. Fouchet, J.R. Johnson, J. Lasue, A.M. Ollila, P. De Parseval, S. Gouy, B. Caron, J.M. Madariaga, G. Arana, M.B. Madsen, J. Laserna, J. Moros, J.A. Manrique, G. Lopez-Reyes, F. Rull, S. Maurice, R.C. Wiens, SuperCam calibration targets on board the perseverance rover: Fabrication and quantitative characterization, Spectrochim. Acta Part B At. Spectrosc. (2021) 106341. https://doi.org/10.1016/j.sab.2021.106341.
[10] L.A. Edgar, C.M. Fedo, S. Gupta, S.G. Banham, A.A. Fraeman, J.P. Grotzinger, K.M. Stack, N.T. Stein, K.A. Bennett, F. Rivera-Hernández, V.Z. Sun, K.S. Edgett, D.M. Rubin, C. House, J. Van Beek, A Lacustrine Paleoenvironment Recorded at Vera RubinRidge, Gale Crater: Overview of the Sedimentology and Stratigraphy Observed by the Mars ScienceLaboratory Curiosity Rover, J. Geophys. Res. Planets. 125 (2020). https://doi.org/10.1029/2019JE006307.
[11] J.P. Grotzinger, S. Gupta, M.C. Malin, D.M. Rubin, J. Schieber, K. Siebach, D.Y. Sumner, K.M. Stack, A.R. Vasavada, R.E. Arvidson, F. Calef, L. Edgar, W.F. Fischer, J.A. Grant, J. Griffes, L.C. Kah, M.P. Lamb, K.W. Lewis, N. Mangold, M.E. Minitti, M. Palucis, M. Rice, R.M.E. Williams, R.A. Yingst, D. Blake, D. Blaney, P. Conrad, J. Crisp, W.E. Dietrich, G. Dromart, K.S. Edgett, R.C. Ewing, R. Gellert, J.A. Hurowitz, G. Kocurek, P. Mahaffy, M.J. McBride, S.M. McLennan, M. Mischna, D. Ming, R. Milliken, H. Newsom, D. Oehler, T.J. Parker, D. Vaniman, R.C. Wiens, S.A. Wilson, Deposition, exhumation, and paleoclimate of an ancient lake deposit, Gale crater, Mars, Science. 350 (2015) aac7575–aac7575. https://doi.org/10.1126/science.aac7575.
[12] M.S. Rice, S. Gupta, A.H. Treiman, K.M. Stack, F. Calef, L.A. Edgar, J. Grotzinger, N. Lanza, L. Le Deit, J. Lasue, K.L. Siebach, A. Vasavada, R.C. Wiens, J. Williams, Geologic overview of the Mars Science Laboratory rover mission at the Kimberley, Gale crater, Mars: Overview of MSL at the Kimberley, J. Geophys. Res. Planets. 122 (2017) 2–20. https://doi.org/10.1002/2016JE005200.
[13] C.I. Fassett, J.W. Head, Fluvial sedimentary deposits on Mars: Ancient deltas in a crater lake in the Nili Fossae region: FLUVIAL SEDIMENTARY DEPOSITS ON MARS, Geophys. Res. Lett. 32 (2005) n/a-n/a. https://doi.org/10.1029/2005GL023456.
[14] T.A. Goudge, R.E. Milliken, J.W. Head, J.F. Mustard, C.I. Fassett, Sedimentological evidence for a deltaic origin of the western fan deposit in Jezero crater, Mars and implications for future exploration, Earth Planet. Sci. Lett. 458 (2017) 357–365. https://doi.org/10.1016/j.epsl.2016.10.056.
[15] N. Mangold, S. Gupta, O. Gasnault, G. Dromart, J.D. Tarnas, S.F. Sholes, B. Horgan, C. Quantin-Nataf, A.J. Brown, S. Le Mouélic, R.A. Yingst, J.F. Bell, O. Beyssac, T. Bosak, F. Calef, B.L. Ehlmann, K.A. Farley, J.P. Grotzinger, K. Hickman-Lewis, S. Holm-Alwmark, L.C. Kah, J. Martinez-Frias, S.M. McLennan, S. Maurice, J.I. Nuñez, A.M. Ollila, P. Pilleri, J.W. Rice, M. Rice, J.I. Simon, D.L. Shuster, K.M. Stack, V.Z. Sun, A.H. Treiman, B.P.

Weiss, R.C. Wiens, A.J. Williams, N.R. Williams, K.H. Williford, Perseverance rover reveals an ancient delta-lake system and flood deposits at Jezero crater, Mars, Science. 374 (2021) 711–717. https://doi.org/10.1126/science.abl4051.
[16] C.C. Bedford, S.P. Schwenzer, J.C. Bridges, S. Banham, R.C. Wiens, O. Gasnault, E.B. Rampe, J. Frydenvang, P.J. Gasda, Geochemical variation in the Stimson formation of Gale crater: Provenance, mineral sorting, and a comparison with modern Martian dunes, Icarus. 341 (2020) 113622. https://doi.org/10.1016/j.icarus.2020.113622.
[17] K.L. Siebach, M.B. Baker, J.P. Grotzinger, S.M. McLennan, R. Gellert, L.M. Thompson, J.A. Hurowitz, Sorting out compositional trends in sedimentary rocks of the Bradbury group (Aeolis Palus), Gale crater, Mars: Bradbury Group Compositional Trends in Gale Crater, J. Geophys. Res. Planets. 122 (2017) 295–328. https://doi.org/10.1002/2016JE005195.
[18] C.C. Bedford, J.C. Bridges, S.P. Schwenzer, R.C. Wiens, E.B. Rampe, J. Frydenvang, P.J. Gasda, Alteration trends and geochemical source region characteristics preserved in the fluviolacustrine sedimentary record of Gale crater, Mars, Geochim. Cosmochim. Acta. 246 (2019) 234–266. https://doi.org/10.1016/j.gca.2018.11.031.
[19] B.H.N. Horgan, R.B. Anderson, G. Dromart, E.S. Amador, M.S. Rice, The mineral diversity of Jezero crater: Evidence for possible lacustrine carbonates on Mars, Icarus. 339 (2020) 113526. https://doi.org/10.1016/j.icarus.2019.113526.
[20] A.J. Brown, S.J. Hook, A.M. Baldridge, J.K. Crowley, N.T. Bridges, B.J. Thomson, G.M. Marion, C.R. de Souza Filho, J.L. Bishop, Hydrothermal formation of Clay-Carbonate alteration assemblages in the Nili Fossae region of Mars, Earth Planet. Sci. Lett. 297 (2010) 174–182. https://doi.org/10.1016/j.epsl.2010.06.018.
[21] A.J. Brown, C.E. Viviano, T.A. Goudge, Olivine-Carbonate Mineralogy of the Jezero Crater Region, J. Geophys. Res. Planets. 125 (2020). https://doi.org/10.1029/2019JE006011.
[22] L. Mandon, C. Quantin-Nataf, P. Thollot, N. Mangold, L. Lozac'h, G. Dromart, P. Beck, E. Dehouck, S. Breton, C. Millot, M. Volat, Refining the age, emplacement and alteration scenarios of the olivine-rich unit in the Nili Fossae region, Mars, Icarus. 336 (2020) 113436. https://doi.org/10.1016/j.icarus.2019.113436.
[23] A.M. Zastrow, T.D. Glotch, Distinct Carbonate Lithologies in Jezero Crater, Mars, Geophys. Res. Lett. 48 (2021). https://doi.org/10.1029/2020GL092365.
[24] R.B. Anderson, R.V. Morris, S.M. Clegg, J.F. Bell, R.C. Wiens, S.D. Humphries, S.A. Mertzman, T.G. Graff, R. McInroy, The influence of multivariate analysis methods and target grain size on the accuracy of remote quantitative chemical analysis of rocks using laser induced breakdown spectroscopy, Icarus. 215 (2011) 608–627. https://doi.org/10.1016/j.icarus.2011.07.034.
[25] S. Schröder, K. Rammelkamp, D.S. Vogt, O. Gasnault, H.-W. Hübers, Contribution of a martian atmosphere to laser-induced breakdown spectroscopy (LIBS) data and testing its emission characteristics for normalization applications, Icarus. 325 (2019) 1–15. https://doi.org/10.1016/j.icarus.2019.02.017.
[26] S.M. Clegg, R.B. Anderson, N. Melikechi, Laser Induced Breakdown Spectroscopy: Theory and Laboratory Spectra of Geological Materials, in: Remote Compos. Anal., Cambridge University Press, 2018.
[27] D.A. Cremers, L. Radziemski, History and fundamentals of LIBS, in: A. Miziolek, I. Schechter, V. Palleschi (Eds.), Laser Induc. Breakdown Spectrosc. Fundam. Appl., Cambridge University Press, 2006: pp. 9–16.
[28] H.Y. McSween, G.J. Taylor, M.B. Wyatt, Elemental Composition of the Martian Crust, Science. 324 (2009) 736–739. https://doi.org/10.1126/science.1165871.
[29] R.V. Morris, G. Klingelhöfer, C. Schröder, D.S. Rodionov, A. Yen, D.W. Ming, P.A. de Souza, I. Fleischer, T. Wdowiak, R. Gellert, B. Bernhardt, E.N. Evlanov, B. Zubkov, J. Foh, U. Bonnes, E. Kankeleit, P. Gütlich, F. Renz, S.W. Squyres, R.E. Arvidson, Mössbauer mineralogy of rock, soil, and dust at Gusev crater, Mars: Spirit's journey through weakly

altered olivine basalt on the plains and pervasively altered basalt in the Columbia Hills: MÖSSBAUER MINERALOGY AT GUSEV CRATER, MARS, J. Geophys. Res. Planets. 111 (2006) n/a-n/a. https://doi.org/10.1029/2005JE002584.
[30] R.V. Morris, G. Klingelhöfer, C. Schröder, D.S. Rodionov, A. Yen, D.W. Ming, P.A. de Souza, T. Wdowiak, I. Fleischer, R. Gellert, B. Bernhardt, U. Bonnes, B.A. Cohen, E.N. Evlanov, J. Foh, P. Gütlich, E. Kankeleit, T. McCoy, D.W. Mittlefehldt, F. Renz, M.E. Schmidt, B. Zubkov, S.W. Squyres, R.E. Arvidson, Mössbauer mineralogy of rock, soil, and dust at Meridiani Planum, Mars: Opportunity's journey across sulfate-rich outcrop, basaltic sand and dust, and hematite lag deposits: IRON MINERALOGY AT MERIDIANI PLANUM, J. Geophys. Res. Planets. 111 (2006) n/a-n/a. https://doi.org/10.1029/2006JE002791.
[31] N.L. Lanza, W.W. Fischer, R.C. Wiens, J. Grotzinger, A.M. Ollila, A. Cousin, R.B. Anderson, B.C. Clark, R. Gellert, N. Mangold, S. Maurice, S. Le Mouélic, M. Nachon, M. Schmidt, J. Berger, S.M. Clegg, O. Forni, C. Hardgrove, N. Melikechi, H.E. Newsom, V. Sautter, High manganese concentrations in rocks at Gale crater, Mars, Geophys. Res. Lett. (2014) 2014GL060329. https://doi.org/10.1002/2014GL060329.
[32] S. Maurice, S.M. Clegg, R.C. Wiens, O. Gasnault, W. Rapin, O. Forni, A. Cousin, V. Sautter, N. Mangold, L. Le Deit, M. Nachon, R.B. Anderson, N.L. Lanza, C. Fabre, V. Payré, J. Lasue, P.-Y. Meslin, R.J. Léveillé, B.L. Barraclough, P. Beck, S.C. Bender, G. Berger, J.C. Bridges, N.T. Bridges, G. Dromart, M.D. Dyar, R. Francis, J. Frydenvang, B. Gondet, B.L. Ehlmann, K.E. Herkenhoff, J.R. Johnson, Y. Langevin, M.B. Madsen, N. Melikechi, J.-L. Lacour, S. Le Mouélic, E. Lewin, H.E. Newsom, A.M. Ollila, P. Pinet, S. Schröder, J.-B. Sirven, R.L. Tokar, M.J. Toplis, C. d'Uston, D.T. Vaniman, A.R. Vasavada, ChemCam activities and discoveries during the nominal mission of the Mars Science Laboratory in Gale crater, Mars, J Anal Spectrom. 31 (2016) 863–889. https://doi.org/10.1039/C5JA00417A.
[33] M. Nachon, S.M. Clegg, N. Mangold, S. Schröder, L.C. Kah, G. Dromart, A. Ollila, J.R. Johnson, D.Z. Oehler, J.C. Bridges, S. Le Mouélic, O. Forni, R. c. Wiens, R.B. Anderson, D.L. Blaney, J. f. Bell, B. Clark, A. Cousin, M.D. Dyar, B. Ehlmann, C. Fabre, O. Gasnault, J. Grotzinger, J. Lasue, E. Lewin, R. Léveillé, S. McLennan, S. Maurice, P.-Y. Meslin, W. Rapin, M. Rice, S.W. Squyres, K. Stack, D.Y. Sumner, D. Vaniman, D. Wellington, Calcium sulfate veins characterized by ChemCam/Curiosity at Gale crater, Mars, J. Geophys. Res. Planets. (2014) 2013JE004588. https://doi.org/10.1002/2013JE004588.
[34] A. Ciucci, M. Corsi, V. Palleschi, S. Rastelli, A. Salvetti, E. Tognoni, New Procedure for Quantitative Elemental Analysis by Laser-Induced Plasma Spectroscopy, Appl. Spectrosc. 53 (1999) 960–964. https://doi.org/10.1366/0003702991947612.
[35] E. Tognoni, G. Cristoforetti, S. Legnaioli, V. Palleschi, Calibration-Free Laser-Induced Breakdown Spectroscopy: State of the art, Spectrochim. Acta Part B At. Spectrosc. 65 (2010) 1–14. https://doi.org/10.1016/j.sab.2009.11.006.
[36] V. Payré, C. Fabre, A. Cousin, V. Sautter, R.C. Wiens, O. Forni, O. Gasnault, N. Mangold, P.-Y. Meslin, J. Lasue, A. Ollila, W. Rapin, S. Maurice, M. Nachon, L. Le Deit, N. Lanza, S. Clegg, Alkali trace elements in Gale crater, Mars, with ChemCam: Calibration update and geological implications: ALKALI TRACE ELEMENTS WITH CHEMCAM, J. Geophys. Res. Planets. 122 (2017) 650–679. https://doi.org/10.1002/2016JE005201.
[37] M.D. Dyar, C.I. Fassett, S. Giguere, K. Lepore, S. Byrne, T. Boucher, C.J. Carey, S. Mahadevan, Comparison of univariate and multivariate models of predictiton of major and minor elements from laser-induced breakdown spectra with and without masking, Spectrochim. Acta Part B At. Spectrosc. 123 (2016) 93–104. http://dx.doi.org/10.1016/j.sab.2016.07.010.
[38] S.M. Clegg, R.C. Wiens, R.B. Anderson, O. Forni, J. Frydenvang, J. Lasue, A. Cousin, V. Payre, T. Boucher, M.D. Dyar, S.M. McLennan, R.V. Morris, T.G. Graff, S.A. Mertzman, B.L. Ehlmann, I. Belgacem, H.E. Newsom, B.C. Clark, N. Melikechi, A. Mezzacappa, R.

McInroy, R. Martinez, P.J. Gasda, O. Gasnault, S. Maurice, Recalibration of the Mars Science Laboratory ChemCam Instrument with an Expanded Geochemical Database, Spectrochim. Acta Part B At. Spectrosc. 129 (2017) 64–85. https://doi.org/10.1016/j.sab.2016.12.003.
[39] H. Hotelling, Analysis of a Complex of Statistical Variables into Principal Components, J. Educ. Psychol. 24 (1933) 417–441. https://doi.org/10.1037/h0071325.
[40] K. Pearson, On lines and planes of closest fit to systems of points in space, Lond. Edinb. Dublin Philos. Mag. J. Sci. 2 (1901) 559–572. https://doi.org/10.1080/14786440109462720.
[41] S. Wold, K. Esbensen, P. Geladi, Principal Component Analysis, Chemom. Intell. Lab. Syst. 2 (1987) 37–52.
[42] R.R. Coifman, D.L. Donoho, Translation-Invariant De-Noising, in: A. Antoniadis, G. Oppenheim (Eds.), Wavelets Stat., Springer New York, New York, NY, 1995: pp. 125–150. https://doi.org/10.1007/978-1-4612-2544-7_9.
[43] J.L. Starck, F. Murtagh, Handbook of Astronomical Data Analysis, 2nd ed., Springer-Verlag, 2006.
[44] R.C. Wiens, S. Maurice, J. Lasue, O. Forni, R.B. Anderson, S. Clegg, S. Bender, D. Blaney, B.L. Barraclough, A. Cousin, L. Deflores, D. Delapp, M.D. Dyar, C. Fabre, O. Gasnault, N. Lanza, J. Mazoyer, N. Melikechi, P.-Y. Meslin, H. Newsom, A. Ollila, R. Perez, R.L. Tokar, D. Vaniman, Pre-flight calibration and initial data processing for the ChemCam laser-induced breakdown spectroscopy instrument on the Mars Science Laboratory rover, Spectrochim. Acta Part B At. Spectrosc. 82 (2013) 1–27. https://doi.org/10.1016/j.sab.2013.02.003.
[45] J.-L. Starck, J. Fadili, F. Murtagh, The Undecimated Wavelet Decomposition and its Reconstruction, IEEE Trans. Image Process. 16 (2007) 297–309. https://doi.org/10.1109/TIP.2006.887733.
[46] E. Stefanutti, F. Bruni, Signal denoising using the Stationary Wavelet Decomposition, (2017) 7.
[47] A. Bijaoui, M. Giudicelli, Optimal image addition using the Wavelet Transform, Exp. Astron. 1 (1990) 347–363. https://doi.org/10.1007/BF00426718.
[48] J.-L. Starck, M. Pierre, Structure detection in low intensity X-ray images, Astron. Astrophys. Suppl. Ser. 128 (1998) 397–407. https://doi.org/10.1051/aas:1998150.
[49] D.E. Anderson, B.L. Ehlmann, O. Forni, S.M. Clegg, A. Cousin, N.H. Thomas, J. Lasue, D.M. Delapp, R.E. McInroy, O. Gasnault, M.D. Dyar, S. Schröder, S. Maurice, R.C. Wiens, Characterization of LIBS emission lines for the identification of chlorides, carbonates, and sulfates in salt/basalt mixtures for the application to MSL ChemCam data: LIBS OF CL, C, S IN SALT-BASALT MIXTURES, J. Geophys. Res. Planets. 122 (2017) 744–770. https://doi.org/10.1002/2016JE005164.
[50] J.M. Tucker, M.D. Dyar, M.W. Schaefer, S.M. Clegg, R.C. Wiens, Optimization of laser-induced breakdown spectroscopy for rapid geochemical analysis, Chem. Geol. 277 (2010) 137–148. https://doi.org/10.1016/j.chemgeo.2010.07.016.
[51] A. Kramida, Y. Ralchenko, J. Reader, NIST Atomic Spectra Database (version 5.9), Natl. Inst. Stand. Technol. (2021). https://doi.org/10.18434/T4W30F.
[52] S.M. Clegg, J. Frydenvang, R.B. Anderson, D.T. Vaniman, P. Gasda, O. Forni, H. Newsom, D. Blaney, R.C. Wiens, Quantitative Sulfur Chemistry Observed on Diverse Samples from Sols 1800-2300, in: 2020: p. 2561. https://www.hou.usra.edu/meetings/lpsc2020/pdf/2561.pdf.
[53] T. Hastie, R. Tibshirani, J. Friedman, The Elements of Statistical Learning: Data Mining, Inference, and Prediction, 2nd ed., Springer, 2017.

[54] M.D. Dyar, C.R. Ytsma, Effect of data set size on geochemical quantification accuracy with laser-induced breakdown spectroscopy, Spectrochim. Acta Part B At. Spectrosc. 177 (2021) 106073. https://doi.org/10.1016/j.sab.2021.106073.
[55] M.M. Breunig, H.-P. Kriegel, R.T. Ng, J. Sander, LOF: Identifying Density-Based Local Outliers, in: Proc. 2000 ACM SIGMOD Int. Conf. Manag. Data, 2000: p. 12.
[56] F.T. Liu, K.M. Ting, Z.-H. Zhou, Isolation-Based Anomaly Detection, ACM Trans. Knowl. Discov. Data. 6 (2012) 1–39. https://doi.org/10.1145/2133360.2133363.
[57] F. Pedregosa, G. Varoquaux, A. Gramfort, V. Michel, B. Thirion, O. Grisel, M. Blondel, P. Prettenhofer, R. Weiss, V. Dubourg, others, Scikit-learn: Machine learning in Python, J. Mach. Learn. Res. 12 (2011) 2825–2830.
[58] R. Tibshirani, Regression Shrinkage and Selection Via the Lasso, J. R. Stat. Soc. Ser. B Methodol. 58 (1996) 267–288. https://doi.org/10.1111/j.2517-6161.1996.tb02080.x.
[59] M.D. Dyar, M.L. Carmosino, E.A. Breves, M.V. Ozanne, S.M. Clegg, R.C. Wiens, Comparison of partial least squares and lasso regression techniques as applied to laser-induced breakdown spectroscopy of geological samples, Spectrochim. Acta Part B At. Spectrosc. 70 (2012) 51–67. https://doi.org/10.1016/j.sab.2012.04.011.
[60] A.E. Hoerl, R.W. Kennard, Ridge Regression: Biased Estimation for Nonorthogonal Problems, Technometrics. 42 (2000) 80–86.
[61] H. Zou, T. Hastie, Regularization and variable selection via the elastic net, J. R. Stat. Soc. Ser. B Stat. Methodol. 67 (2005) 301–320. https://doi.org/10.1111/j.1467-9868.2005.00503.x.
[62] S.G. Mallat, Zhifeng Zhang, Matching pursuits with time-frequency dictionaries, IEEE Trans. Signal Process. 41 (1993) 3397–3415. https://doi.org/10.1109/78.258082.
[63] R. Rubinstein, M. Zibulevsky, M. Elad, Efficient Implementation of the K-SVD Algorithm using Batch Orthogonal Matching Pursuit, (2008) 15.
[64] S. Wold, M. Sjöström, L. Eriksson, PLS-regression: a basic tool of chemometrics, Chemom. Intell. Lab. Syst. 58 (2001) 109–130.
[65] R.B. Anderson, S.M. Clegg, J. Frydenvang, R.C. Wiens, S. McLennan, R.V. Morris, B.L. Ehlmann, M.D. Dyar, Improved accuracy in quantitative laser-induced breakdown spectroscopy using sub-models, Spectrochim. Acta Part B At. Spectrosc. 129 (2017) 49–57. http://dx.doi.org/10.1016/j.sab.2016.12.003.
[66] S.M. Clegg, E. Sklute, M.D. Dyar, J.E. Barefield, R.C. Wiens, Multivariate analysis of remote laser-induced breakdown spectroscopy spectra using partial least squares, principal component analysis, and related techniques, Spectrochim. Acta Part B At. Spectrosc. 64 (2009) 79–88. https://doi.org/10.1016/j.sab.2008.10.045.
[67] S.R. Gunn, Support Vector Machines for Classification and Regression, University of Southampton, 1998.
[68] C.-J. Lu, T.-S. Lee, C.-C. Chiu, Financial time series forecasting using independent component analysis and support vector regression, Decis. Support Syst. 47 (2009) 115–125. https://doi.org/10.1016/j.dss.2009.02.001.
[69] J.H. Friedman, Stochastic gradient boosting, Comput. Stat. Data Anal. 38 (2002) 367–378. https://doi.org/10.1016/S0167-9473(01)00065-2.
[70] J.H. Friedman, Greedy function approximation: A gradient boosting machine., Ann. Stat. 29 (2001). https://doi.org/10.1214/aos/1013203451.
[71] L. Breiman, Random Forests, Mach. Learn. 45 (2001) 5–32. https://doi.org/10.1023/A:1010933404324.
[72] S.B. Kotsiantis, Decision trees: a recent overview, Artif. Intell. Rev. 39 (2013) 261–283. https://doi.org/10.1007/s10462-011-9272-4.
[73] R.E. Schapire, A Brief Introduction to Boosting, in: Proc. Sixt. Int. Jt. Conf. Artif. Intell., 1999: p. 6.

[74] P.J. Huber, Robust Estimation of a Location Parameter, Ann. Math. Stat. 35 (1964) 73–101. https://doi.org/10.1214/aoms/1177703732.
[75] J. Shenk, M. Westerhaus, P. Berzaghi, Investigation of a LOCAL calibration procedure for near infrared instruments, J. Infrared Spectrosc. 5 (1997) 223. https://doi.org/10.1255/jnirs.115.
[76] J. Frydenvang, P.J. Gasda, J.A. Hurowitz, J.P. Grotzinger, R.C. Wiens, H.E. Newsom, K.S. Edgett, J. Watkins, J.C. Bridges, S. Maurice, M.R. Fisk, J.R. Johnson, W. Rapin, N.T. Stein, S.M. Clegg, S.P. Schwenzer, C.C. Bedford, P. Edwards, N. Mangold, A. Cousin, R.B. Anderson, V. Payré, D. Vaniman, D.F. Blake, N.L. Lanza, S. Gupta, J. Van Beek, V. Sautter, P.-Y. Meslin, M. Rice, R. Milliken, R. Gellert, L. Thompson, B.C. Clark, D.Y. Sumner, A.A. Fraeman, K.M. Kinch, M.B. Madsen, I.G. Mitrofanov, I. Jun, F. Calef, A.R. Vasavada, Diagenetic silica enrichment and late-stage groundwater activity in Gale crater, Mars: Silica Enriching Diagenesis, Gale, Mars, Geophys. Res. Lett. 44 (2017) 4716–4724. https://doi.org/10.1002/2017GL073323.
[77] E.B. Rampe, D.F. Blake, T.F. Bristow, D.W. Ming, D.T. Vaniman, R.V. Morris, C.N. Achilles, S.J. Chipera, S.M. Morrison, V.M. Tu, A.S. Yen, N. Castle, G.W. Downs, R.T. Downs, J.P. Grotzinger, R.M. Hazen, A.H. Treiman, T.S. Peretyazhko, D.J. Des Marais, R.C. Walroth, P.I. Craig, J.A. Crisp, B. Lafuente, J.M. Morookian, P.C. Sarrazin, M.T. Thorpe, J.C. Bridges, L.A. Edgar, C.M. Fedo, C. Freissinet, R. Gellert, P.R. Mahaffy, H.E. Newsom, J.R. Johnson, L.C. Kah, K.L. Siebach, J. Schieber, V.Z. Sun, A.R. Vasavada, D. Wellington, R.C. Wiens, Mineralogy and geochemistry of sedimentary rocks and eolian sediments in Gale crater, Mars: A review after six Earth years of exploration with Curiosity, Geochemistry. 80 (2020) 125605. https://doi.org/10.1016/j.chemer.2020.125605.
[78] A.H. Treiman, D.L. Bish, D.T. Vaniman, S.J. Chipera, D.F. Blake, D.W. Ming, R.V. Morris, T.F. Bristow, S.M. Morrison, M.B. Baker, E.B. Rampe, R.T. Downs, J. Filiberto, A.F. Glazner, R. Gellert, L.M. Thompson, M.E. Schmidt, L. Le Deit, R.C. Wiens, A.C. McAdam, C.N. Achilles, K.S. Edgett, J.D. Farmer, K.V. Fendrich, J.P. Grotzinger, S. Gupta, J.M. Morookian, M.E. Newcombe, M.S. Rice, J.G. Spray, E.M. Stolper, D.Y. Sumner, A.R. Vasavada, A.S. Yen, Mineralogy, provenance, and diagenesis of a potassic basaltic sandstone on Mars: CheMin X-ray diffraction of the Windjana sample (Kimberley area, Gale Crater), J. Geophys. Res. Planets. 121 (2016) 75–106. https://doi.org/10.1002/2015JE004932.
[79] J. Lasue, A. Cousin, P. -Y. Meslin, N. Mangold, R.C. Wiens, G. Berger, E. Dehouck, O. Forni, W. Goetz, O. Gasnault, W. Rapin, S. Schroeder, A. Ollila, J. Johnson, S. Le Mouélic, S. Maurice, R. Anderson, D. Blaney, B. Clark, S.M. Clegg, C. d'Uston, C. Fabre, N. Lanza, M.B. Madsen, J. Martin-Torres, N. Melikechi, H. Newsom, V. Sautter, M.P. Zorzano, Martian Eolian Dust Probed by ChemCam, Geophys. Res. Lett. 45 (2018). https://doi.org/10.1029/2018GL079210.
[80] International Organization for Standardization, ISO 5725-1: 1994: accuracy (trueness and precision) of measurement methods and results-part 1: general principles and definitions, (1994).
[81] M. Thompson, Precision in chemical analysis: a critical survey of uses and abuses, Anal. Methods. 4 (2012) 1598. https://doi.org/10.1039/c2ay25083g.
[82] N. Mangold, O. Forni, G. Dromart, K. Stack, R.C. Wiens, O. Gasnault, D.Y. Sumner, M. Nachon, P.-Y. Meslin, R.B. Anderson, B. Barraclough, J.F. Bell, G. Berger, D.L. Blaney, J.C. Bridges, F. Calef, B. Clark, S.M. Clegg, A. Cousin, L. Edgar, K. Edgett, B. Ehlmann, C. Fabre, M. Fisk, J. Grotzinger, S. Gupta, K.E. Herkenhoff, J. Hurowitz, J.R. Johnson, L.C. Kah, N. Lanza, J. Lasue, S. Le Mouélic, R. Léveillé, E. Lewin, M. Malin, S. McLennan, S. Maurice, N. Melikechi, A. Mezzacappa, R. Milliken, H. Newsom, A. Ollila, S.K. Rowland, V. Sautter, M. Schmidt, S. Schröder, C. d'Uston, D. Vaniman, R. Williams, Chemical variations in Yellowknife Bay formation sedimentary rocks analyzed by ChemCam on

board the Curiosity rover on Mars, J. Geophys. Res. Planets. 120 (2015) 2014JE004681. https://doi.org/10.1002/2014JE004681.
[83] K. Rammelkamp, O. Gasnault, O. Forni, C.C. Bedford, E. Dehouck, A. Cousin, J. Lasue, G. David, T.S.J. Gabriel, S. Maurice, R.C. Wiens, Clustering supported classification of ChemCam data from Gale crater, Mars, Earth Space Sci. (2021). https://doi.org/10.1029/2021EA001903.
[84] D.L. Blaney, R.C. Wiens, S. Maurice, S.M. Clegg, R.B. Anderson, L.C. Kah, S. Le Mouélic, A. Ollila, N. Bridges, R. Tokar, G. Berger, J.C. Bridges, A. Cousin, B. Clark, M.D. Dyar, P.L. King, N. Lanza, N. Mangold, P.-Y. Meslin, H. Newsom, S. Schröder, S. Rowland, J. Johnson, L. Edgar, O. Gasnault, O. Forni, M. Schmidt, W. Goetz, K. Stack, D. Sumner, M. Fisk, M.B. Madsen, Chemistry and texture of the rocks at Rocknest, Gale Crater: Evidence for sedimentary origin and diagenetic alteration, J. Geophys. Res. Planets. (2014) 2013JE004590. https://doi.org/10.1002/2013JE004590.
[85] N. Melikechi, A. Mezzacappa, A. Cousin, N.L. Lanza, J. Lasue, S.M. Clegg, G. Berger, R.C. Wiens, S. Maurice, R.L. Tokar, S. Bender, O. Forni, E.A. Breves, M.D. Dyar, J. Frydenvang, D. Delapp, O. Gasnault, H. Newsom, A.M. Ollila, E. Lewin, B.C. Clark, B.L. Ehlmann, D. Blaney, C. Fabre, Correcting for variable laser-target distances of laser-induced breakdown spectroscopy measurements with ChemCam using emission lines of Martian dust spectra, Spectrochim. Acta Part B At. Spectrosc. 96 (2014) 51–60. https://doi.org/10.1016/j.sab.2014.04.004.
[86] A. Mezzacappa, N. Melikechi, A. Cousin, R.C. Wiens, J. Lasue, S.M. Clegg, R. Tokar, S. Bender, N.L. Lanza, S. Maurice, G. Berger, O. Forni, O. Gasnault, M.D. Dyar, T. Boucher, E. Lewin, C. Fabre, Application of distance correction to ChemCam laser-induced breakdown spectroscopy measurements, Spectrochim. Acta Part B At. Spectrosc. 120 (2016) 19–29. https://doi.org/10.1016/j.sab.2016.03.009.
[87] R.C. Wiens, A.J. Blazon-Brown, N. Melikechi, J. Frydenvang, E. Dehouck, S.M. Clegg, D. Delapp, R.B. Anderson, A. Cousin, S. Maurice, Improving ChemCam LIBS long-distance elemental compositions using empirical abundance trends, Spectrochim. Acta Part B At. Spectrosc. 182 (2021) 106247. https://doi.org/10.1016/j.sab.2021.106247.
[88] N. Klein, P.J. Gasda, J. Castorena, D. Oyen, Gaussian Process Variational Autoencoders for Generative Modeling of ChemCam Data, in: Lunar and Planetary Institute, 2021: p. 2549. https://www.hou.usra.edu/meetings/planetdata2021/pdf/7052.pdf.
[89] A.M. Ollila, H.E. Newsom, B. Clark, R.C. Wiens, A. Cousin, J.G. Blank, N. Mangold, V. Sautter, S. Maurice, S.M. Clegg, O. Gasnault, O. Forni, R. Tokar, E. Lewin, M.D. Dyar, J. Lasue, R. Anderson, S.M. McLennan, J. Bridges, D. Vaniman, N. Lanza, C. Fabre, N. Melikechi, G.M. Perrett, J.L. Campbell, P.L. King, B. Barraclough, D. Delapp, S. Johnstone, P.-Y. Meslin, A. Rosen-Gooding, J. Williams, The MSL Science Team, Trace element geochemistry (Li, Ba, Sr, and Rb) using Curiosity's ChemCam: Early results for Gale crater from Bradbury Landing Site to Rocknest, J. Geophys. Res. Planets. 119 (2014) 2013JE004517. https://doi.org/10.1002/2013JE004517.
[90] P.J. Gasda, R.B. Anderson, A. Cousin, O. Forni, S.M. Clegg, A. Ollila, N. Lanza, J. Frydenvang, S. Lamm, R.C. Wiens, S. Maurice, O. Gasnault, R. Beal, A. Reyes-Newell, D. Delapp, Quantification of manganese for ChemCam Mars and laboratory spectra using a multivariate model, Spectrochim. Acta Part B At. Spectrosc. 181 (2021) 106223. https://doi.org/10.1016/j.sab.2021.106223.
[91] O. Forni, P.-Y. Meslin, A. Cousin, S.M. Clegg, N. Mangold, L. Le Deit, O. Gasnault, G. David, M. Nachon, D.L. Blaney, H. Newsom, S. Maurice, R.C. Wiens, M. Gaft, Fluorine on Mars: Seven Years of Detection with ChemCam Onboard MSL, in: 2019: p. 6095. https://www.hou.usra.edu/meetings/ninthmars2019/pdf/6095.pdf.
[92] J. Lasue, S.M. Clegg, O. Forni, A. Cousin, R.C. Wiens, N. Lanza, N. Mangold, L. Le Deit, O. Gasnault, S. Maurice, J.A. Berger, K. Stack, D. Blaney, C. Fabre, W. Goetz, J. Johnson,

S. Le Mouélic, M. Nachon, V. Payré, W. Rapin, D.Y. Sumner, Observation of > 5 wt % zinc at the Kimberley outcrop, Gale crater, Mars, J. Geophys. Res. Planets. 121 (2016) 338–352. https://doi.org/10.1002/2015JE004946.

[93] W. Rapin, B.L. Ehlmann, G. Dromart, J. Schieber, N.H. Thomas, W.W. Fischer, V.K. Fox, N.T. Stein, M. Nachon, B.C. Clark, L.C. Kah, L. Thompson, H.A. Meyer, T.S.J. Gabriel, C. Hardgrove, N. Mangold, F. Rivera-Hernandez, R.C. Wiens, A.R. Vasavada, An interval of high salinity in ancient Gale crater lake on Mars, Nat. Geosci. 12 (2019) 889–895. https://doi.org/10.1038/s41561-019-0458-8.

[94] Yongdong. Wang, D.J. Veltkamp, B.R. Kowalski, Multivariate instrument standardization, Anal. Chem. 63 (1991) 2750–2756. https://doi.org/10.1021/ac00023a016.